

Numerical modelling of tsunami effects at two sites on the Coromandel Peninsula, New Zealand:

Whitianga and Tairua-Pauanui

Prepared by:
eCoast Limited
Marine Consulting and
Research
P.O. Box 151
Raglan, New Zealand

For:
Waikato Regional Council
Private Bag 3038
Waikato Mail Centre
HAMILTON 3240

June 2012

Document #: 2741634

Approved for release
by:

Adam Munro

Date June 2013

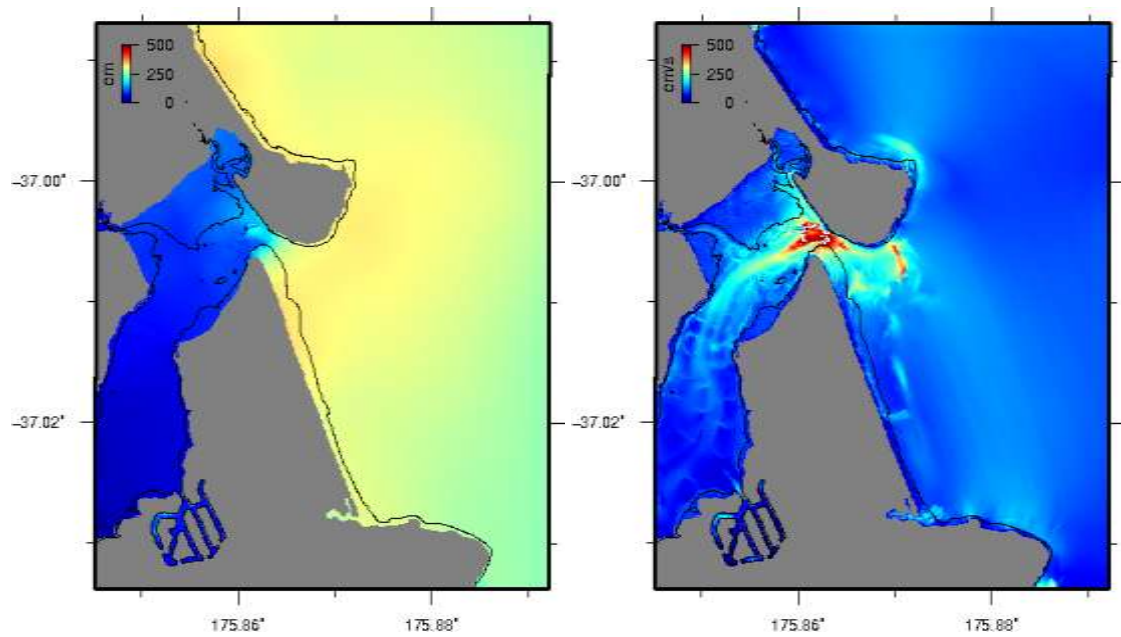
Disclaimer

This technical report has been prepared for the use of Waikato Regional Council as a reference document and as such does not constitute Council's policy.

Council requests that if excerpts or inferences are drawn from this document for further use by individuals or organisations, due care should be taken to ensure that the appropriate context has been preserved, and is accurately reflected and referenced in any subsequent spoken or written communication.

While Waikato Regional Council has exercised all reasonable skill and care in controlling the contents of this report, Council accepts no liability in contract, tort or otherwise, for any loss, damage, injury or expense (whether direct, indirect or consequential) arising out of the provision of this information or its use by you or any other party.

Numerical modelling of Tsunami Effects at two sites on the Coromandel Peninsula, New Zealand: Whitianga and Tairua-Pauanui



eCoast Limited
Marine Consulting and Research
P.O. Box 151
Raglan, New Zealand

jose@ecoast.co.nz

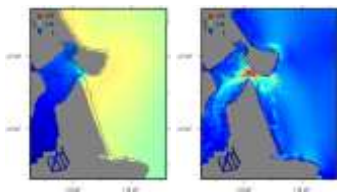
Numerical modelling of Tsunami Effects at two sites on the Coromandel Peninsula, New Zealand: Whitianga and Tairua-Pauanui

Report Status

Version	Date	Status	Approved By:
V 1	30-June-2012	DRAFT	JCB
V 5	13-May-2013	FINAL DRAFT	JCB
V 6	19-Jun-2013	FINAL	JCB

It is the responsibility of the reader to verify the currency of the version number of this report.

Jose C. Borrero Ph.D.



Cover Picture: Maximum water level (left) and current speed (right) for the Tairua and Pauanui estuary caused by a M~8.9 earthquake on the southern segments of the Tonga-Kermadec Trench.

The information, including the intellectual property, contained in this report is confidential and proprietary to eCoast Limited. It may be used by the persons to whom it is provided for the stated purpose for which it is provided, and must not be imparted to any third person without the prior written approval of eCoast. eCoast Limited reserves all legal rights and remedies in relation to any infringement of its rights in respect of its confidential information.

© eCoast Limited 2013

EXECUTIVE SUMMARY

This report details a tsunami inundation modelling study for two sites on the Coromandel Peninsula, New Zealand. We use the latest scientific literature on tsunami sources and high-resolution bathymetry grids to produce inundation predictions for Whitianga and Tairua – Pauanui. The model settings and parameters are established through sensitivity analyses and comparison of model results to historical data. This includes instrumental data recorded on the Whitianga tide gauge during the 2010 Chile and 2011 Japan tsunamis as well as eyewitness accounts regarding the wave activity and inundation extents from the 1960 Chile tsunami in Whitianga. The model results are also compared and contrasted with the model results previously presented by Prasetya et al. (2008) for Whitianga.

Model grid data was provided by the Waikato Regional Council for the study sites. This data was used in conjunction with publicly available bathymetry and topography to form a system of nested model grids. The numerical model itself was set up in the ComMIT modelling framework, a tsunami modelling tool developed by the National Oceanic and Atmospheric Administration (NOAA) of the United States of America. The ComMIT tool was specifically designed to provide an accessible means of robust tsunami inundation modelling for regions susceptible to tsunami hazards.

In this study we examine several historical events including the 1960 and 2010 Chilean tsunamis and the 2011 Japan tsunami. For the 1960 event, we examine a suite of 6 earthquake models. Each model has roughly the same magnitude, but with different slip distributions at the earthquake source. For the 2010 and 2011 tsunamis we use source models that were derived from the inversion of tsunami wave signals recorded on NOAA's tsunameter stations in the Pacific Ocean.

Hypothetical tsunami sources include earthquakes positioned along the Tonga-Kermadec (TK) Trench subduction zone and a large subduction zone event located on the southern coast of Peru in South America. These sources are included as they represent a significant hazard from both the near and far field. The Tonga-Kermadec Trench cases are a significant hazard in that this faulting zone lies adjacent to New Zealand and tsunami waves can begin affecting the study region less than 1 hour after generation. For far field sources, it has been shown that sources located in northern Chile or southern Peru produce higher waves in New Zealand relative to other areas around the Pacific Rim.

We first performed several sensitivity analyses to look at the effect of different model parameters on the ultimate results. These analyses included the effects of the grid configuration, the earthquake slip distribution and the model friction settings. These sensitivity studies are done in light of the available historical data to provide the best possible model calibration.

The sensitivity analysis led to a good fit between modelled and observed water levels at Whitianga caused by the 2011 Japan tsunami. The sensitivity analyses also highlighted the role that the slip distribution plays in the water level record for far-field sources in southern Chile affecting New Zealand. We show that the range of tsunami heights is relatively insensitive to the slip distribution, but that the slip distribution is important in the finer details of the water level record and should be taken in to account when possible.

Based on our sensitivity tests we chose a Manning's 'n' of 0.03 as the preferred friction factor for use in this model. Lower values led to small increases in wave height, but unrealistically large increase in current speed. Thus the default (0.03) was retained as the preferred value.

The model results for the 1960 Chile tsunami in Whitianga were shown to compare very well with the eyewitness descriptions of the character of the tsunami waves and the timing of the strongest effects. The model however does not match the inundation patterns precisely. We attribute this primarily to discrepancies in the topographic data provided for the study.

Correcting the Whitianga bathymetry for a datum shift led to a great improvement in the model results in terms of the inundation along Buffalo Beach and in the town's riverfront area. Considering all of the available observational data, we contend that the effects of the 1960 Chile tsunami in Whitianga are best explained by a variable slip fault model derived from the direct inversion of tide gauge data and land level changes in South America.

For the Tonga-Kermadec Trench scenarios, the modelling suggests that the leading wave cycles will have the greatest impact on the study region. This is in contrast to both models and observations from large scale far-field tsunamis which feature some of the larger wave heights many hours after arrival.

Following on from this analysis, we illustrated the relative impact of waves from different sources along the Tonga-Kermadec Trench. The greatest effect on sites in the Coromandel Peninsula is shown to result from ruptures on the southern segments of the fault that are situated to the north of the East Cape. The induced wave heights fall off as the source region is moved to the north or south.

From this point we moved to the predictive modelling runs for the study sites. Because inundation modelling for Whitianga was previously completed by Prasetya et al. (2008), the focus of this study is on the Tairua-Pauanui harbour area, although we present results for Whitianga as well.

The model results suggest that far-field sources have a relatively minor impact on Tairua-Pauanui as compared to Whitianga. Inundation levels from these sources (Chile 1960, Chile 2010, Japan 2011 and Peru Hypothetical) are all well below the crest of the dunes on either Tairua or Pauanui. The most significant effect from these types of sources is the generation of strong current in the harbour entrance and along the wharf area. Of the far field sources, the Peru source is shown to be the most potentially damaging.

For the near-field sources, we show that the TK Trench scenarios present a greater inundation hazard than the far-field sources. We model a range of scenarios; we positioned the fault at a location where it would cause the greatest impact on the study region as well as running a set of simulations moved to the north. The earthquake scenarios in this section ranged in size from 8.9 to 9.0 to 9.1 with slip amounts of 10.5, 14.3 and 20.8 m respectively. As expected, the fault located further south resulted in stronger and larger waves affecting Tairua.

Our final series of models looked at extreme earthquake events, analogous to some of the largest earthquakes known to have occurred on earth. These sources were positioned along the southern end of the TK Trench, north of East Cape, so as to

provide some indication of a worst-case scenario. The model results show that a source similar in size to the 1960 Chile earthquake occurring on the TK trench would result in complete overtopping of the Tairua and Pauanui Sand Spits. While not as extreme, using the same source mechanism as the 2011 Japan tsunami positioned along the southern section of the TK trench results in severe inundation along the Pauanui Peninsula and overtopping towards the southern end.

CONTENTS

EXECUTIVE SUMMARY	I
1 INTRODUCTION.....	11
1.1 REVIEW OF RECENT LITERATURE	12
1.2 MODELLING APPROACH	12
1.3 NUMERICAL MODELLING GRIDS	13
2 EARTHQUAKE SOURCE MODELS	16
2.1 1960 CHILE EARTHQUAKE AND TSUNAMI.....	16
2.2 KERMADEC TRENCH SCENARIOS	19
2.3 ADDITIONAL SOUTH AMERICAN TSUNAMI SOURCES: PERU AND NORTHERN CHILE	21
3 MODEL CALIBRATION AND SENSITIVITY ANALYSIS	23
3.1 MODEL GRID CONFIGURATIONS.....	23
3.2 CALIBRATION WITH JAPAN 2011 TSUNAMI DATA	25
3.3 THE FEBRUARY 2010 CHILE TSUNAMI	27
3.4 1960 CHILE TSUNAMI	28
3.4.1 <i>Effect of Grid Configuration</i>	28
3.4.2 <i>Effect of slip distribution</i>	30
3.4.3 <i>Effect of Friction Coefficient</i>	31
3.4.4 <i>Qualitative Comparison to Historical Accounts</i>	35
3.5 MODEL RESULTS FOR 1960 ON THE REVISED WHITIANGA BATHYMETRY.....	40
3.6 KERMADEC TRENCH SOURCE: EFFECT OF GRID CONFIGURATION	43
3.7 KERMADEC TRENCH SOURCE: SENSITIVITY TO SEGMENT LOCATION:	44
3.8 SUMMARY OF THE MODEL CALIBRATION AND SENSITIVITY ANALYSIS	46
3.9 ARRIVAL TIMES AT WHITIANGA AND TAIRUA-PAUANUI FROM TK SCENARIOS	47
4 MODEL RESULTS: TAIRUA PAUANUI.....	49
4.1 FAR FIELD SOURCES.....	52
4.2 KERMADEC TRENCH SOURCES.....	55
5 MODEL RESULTS: WHITIANGA.....	61
5.1 FAR FIELD SOURCES.....	61
5.2 KERMADEC TRENCH SCENARIOS	65
6 SITE VISIT	70
6.1 TAIRUA.....	71
6.2 PAUANUI.....	74
6.3 WHITIANGA.....	78
7 EXTREME SCENARIO INUNDATION MAPS	81
8 REFERENCES.....	88

TABLE OF FIGURES

Figure 1.1 The location of Whitianga, Tairua and Pauanui on the east coast of the Coromandel Peninsula.	11
Figure 1.2 The ComMIT propagation model database for tsunamis in the world's oceans. Insets show the details of the source zone discretization in to rectangular sub-faults.	13
Figure 1.3 Modelling grids used for the Whitianga simulations. Note that two 'A' level grids were trialled in this study.	14
Figure 1.4 Modelling grids used for the Tairua/Pauanui simulations.	15
Figure 2.1 Unit source segments used to define the 1960 Chilean Earthquake suite of events.	17
Figure 2.2 Six representations of the co seismic deformation associated with the 1960 Chilean earthquake	18
Figure 2.3 Case 1,2: 600 x 100 km fault 10.47 m average slip, M = 8.9. Case 3, 4: 600 x 100 km fault, 14.8 m average slip, M = 9. Note the change in the colour scale for cases 3 and 4.	19
Figure 2.4 Cases 5 and 6: 600 x 100 km fault, 20.9 m average slip, M = 9.1	20
Figure 2.5 Case 7 (left) 1000 x 100 km fault, 35 m max slip at south end of the Tonga-Kermadec Trench (M = 9.3). Case 8 (right) the Japan 2011 tsunami source positioned at the southern end of the Tonga-Kermadec Trench (M=8.81).	20
Figure 2.6 Fault segments used to construct the Peru tsunami source (left) and the initial deformation field used to initialise the tsunami model(right).	21
Figure 2.7 Three additional South American sources. Variant of the 1960 Chile earthquake are positioned along the coast of Northern Chile and Southern Peru.	22
Figure 3.1 Grid configuration 1. Red dots indicate locations where time series data is analysed, Location 2 corresponds to the Whitianga tide gauge.	24
Figure 3.2 Grid configuration 2. Red dots indicate locations where time series data is analysed, Location 2 corresponds to the Whitianga tide gauge.	24
Figure 3.3 Coarse grid configuration.	24
Figure 3.4 Source model used for the 2011 Tohoku tsunami, The amount of slip on each segment is indicated in the left panel, while the vertical deformation of the sea floor is shown on the right (image reproduced from Wei et al., 2012).	25
Figure 3.5 Comparison between modelled and measured water levels in Whitianga during the March 2011 Japan tsunami. The results from Grid Configuration 2 (highlighted in the red box) provide a better comparison to the tide gauge data.	26
Figure 3.6 Maximum computed water levels for the Japan 2011 tsunami in Mercury Bay using Grid Configuration 1 (left) and Configuration 2 (right).	26
Figure 3.7 Source segments used for the 2010 Chile tsunami.	27
Figure 3.8 Comparison between measured and modelled water levels at the Whitianga tide gauge for the February 2010 Chile earthquake and tsunami. Simulation run on Grid Configuration 2.	27

Figure 3.9 Comparison between model results for the two grid configurations at three locations in Whitianga using a Chile 1960 source.	28
Figure 3.10 Maximum computed water levels in Mercury Bay for Case 6 of the 1960 Chilean earthquake scenarios. GC 1 (left) and GC 2 (right).	29
Figure 3.11 Modelled water levels at the Whitianga tide gauge resulting from 6 different versions of the 1960 Chile earthquake source model.	30
Figure 3.12 The effect of the friction coefficient on water levels at the Whitianga tide gauge location for Case 3 and Case 6 of the 1960 Chilean tsunami sources. The GC2 and GC2f2 results are nearly indistinguishable from one another and appear as one trace on the plot.	31
Figure 3.13 Maximum computed water levels in Mercury Bay for Case 3 of 1960 Chilean earthquake scenarios on Grid Configuration 2. A friction factor of 0.03 is used on the left and 0.021 on the right.	32
Figure 3.14 Maximum computed water levels in Mercury Bay for Case 6 of 1960 Chilean earthquake scenarios on Grid Configuration 2. A friction factor of 0.03 is used on the left and 0.021 on the right. Note: the colour scale has changed from the previous figure.	32
Figure 3.15 Maximum computed current speed in Mercury Bay for Case 3 of 1960 Chilean earthquake scenarios on Grid Configuration 2. A friction factor of 0.03 is used on the left and 0.021 on the right.	33
Figure 3.16 Maximum computed current speed in Mercury Bay for Case 6 of 1960 Chilean earthquake scenarios on Grid Configuration 2. A friction factor of 0.03 is used on the left and 0.021 on the right.	33
Figure 3.17 The effect of friction setting on modelled water levels at the Whitianga tide gauge for the 2011 Japan tsunami. The two time series from the model are virtually indistinguishable from one another and appear as one blue trace on the plot.	34
Figure 3.18 The effect of friction setting on modelled water levels and current speeds in Buffalo Bay for the 2011 Japan tsunami.	34
Figure 3.19 (top) The predicted tide on the day the 1960 Chile tsunami affected Whitianga. Important times are marked and noted. (bottom) Model results (red) for the six source models compared to the predicted tide level. (black) Blue dots indicate the modelled arrival time and the time when the worst effects were observed by the witnesses.	36
Figure 3.20 Time series of computed water levels at the present location of the Whitianga tide gauge for the six different 1960 Chilean tsunami source models. Model results are from GC 2.	37
Figure 3.21 Modelled inundation overlaid on an aerial image of the Whitianga waterfront. The red line indicates the approximate observed extent of inundation in 1960.	38
Figure 3.22 The model bathymetry along the Whitianga water front (left) and a photo of the area (right). The photo was taken from a location approximated by the blue oval. The red is the 0 m contour, black contours are in 1 m intervals. Photo was taken between 1 and 2 pm on May 16, 2012 when the tide stage would have been at approximately +1.5 m relative to MLLW (http://www.tides4fishing.com/nz/coromandel/whitianga).	39

Figure 3.23 Inundation results from Prasetya et al., 2009 for the 1960 Chilean tsunami in Whitianga which significantly overstate the level of inundation along Buffalo beach.	39
Figure 3.24 Modelling grids adjusted by 1.6 m. The dashed black line is the shoreline (0 m) contour in the original grid.....	40
Figure 3.25 Modelled inundation in Whitianga from four different models of the 1960 Chilean tsunami. The location of the old Aerodrome hangar is indicated with a red dot.	41
Figure 3.26 Comparison between model results for the two grid configurations at three locations in Whitianga using a Kermadec Trench tsunami source.	43
Figure 3.27 (left) The fault segments used in the sensitivity analysis, Each number corresponds to two segments used in each model run. (right) The bathymetry at Pauanui, the red dot corresponds to the location where wave height information is extracted and analysed.....	44
Figure 3.28 Maximum and minimum wave amplitudes recorded offshore of Pauanui Beach as a function of the fault segment.	45
Figure 3.29 Computed wave forms recorded offshore of Pauanui Beach for each of the 11 fault segments.	45
Figure 3.30 The leading wave at Whitianga for the eight TK Scenario events.	48
Figure 3.31 Time series of the leading waves at Whitianga and Tairua for Case 3 and Case 8.....	48
Figure 4.1 The Tairua topography DEM over aerial imagery. The photo shown in below was taken from the location indicated by the blue dot with a view to the southeast. The thicker black line is the 0 m contour while the red line is the +1 m elevation. Thinner black contours are at 5 m intervals.	50
Figure 4.2 View along Pauanui Beach, the dune crest is on the order of 5 meters above sea level and there is an ample set back to the first house.	51
Figure 4.3 The beach at Tairua showing the relatively high dune ridge and large set back along the northern end of the beach. On the southern end (in the foreground) the topographic relief is lower and the buildings are located closer to the sea.	51
Figure 4.4 Maximum computed water level in Tairua at mid-tide for Cases 1 – 6 of the 1960 Chile tsunami.....	52
Figure 4.5 Maximum computed current speed in Tairua at mid-tide for Cases 1 – 6 of the 1960 Chile tsunami.....	53
Figure 4.6 Simulation of the 2011 Japan tsunami in Tairua. Water level (left) and current speed (right).	54
Figure 4.7 Simulation of a 1960 Chile-type source in Peru affecting Tairua at mid-tide. Water level (left) and current speed (right).	54
Figure 4.8 Maximum computed water levelled for the Kermadec Trench Cases 1-5 in Tairua at MSL. Note change in colour scale on Case 5 and Case 6.	55
Figure 4.9 Maximum computed current speeds for the Kermadec Trench Cases 1-6 in Tairua at MSL. Note change in colour scale on Case 5 and Case 6.	56

Figure 4.10 Comparison between mid tide (left) and high tide (+1 m, right) modelled inundation at Tairua – Pauanui for the three southern Kermadec Trench scenarios. Contours are the 0,1 and 5 m contours relative to MSL.	57
Figure 4.11 Comparison between mid tide (left) and high tide (+1 m, right) modelled current speeds at Tairua – Pauanui for the three southern Kermadec Trench scenarios. Contours are the 0,1 and 5 m contours relative to MSL.	58
Figure 4.12 Maximum computed water levels and current speeds in Tairua from Case 7 (left) and case 8 (right) at high tide.	59
Figure 4.13 Maximum computed water levels and current speeds in Tairua from Case 7 (left) and case 8 (right) at MSL.	60
Figure 5.1 Maximum water level (cm), Whitianga, 1960 cases. Note these results are for Grid Configuration 2. Cases 3-6 are computed on the	61
Figure 5.2 Maximum current speed, (cm/sec) Whitianga, 1960 cases. Note these results are for Grid Configuration 2.	62
Figure 5.3 Maximum water level and current speeds in Mercury Bay predicted by the model for a hypothetical 1960-type source located in Peru (left) and northern Chile (right).	63
Figure 5.4 Maximum water level and current speeds in Mercury Bay predicted by the model for a hypothetical 1960-type source located in the Peru/Chile border region.	64
Figure 5.5 Maximum water level and current speed in Whitianga predicted by the model for the 2011 Japan (Tohoku-oki) tsunami.	65
Figure 5.6 Kermadec Trench scenarios in Whitianga. Case 1 (top) and Case 2 (bottom). For each case water level is on the left and current speed is on the right.	66
Figure 5.7 Kermadec Trench scenarios in Whitianga. Case 3 (top) and Case 4 (bottom). For each case water level is on the left and current speed is on the right.	67
Figure 5.8 Kermadec Trench scenarios in Whitianga. Case 5 (top) and Case 6 (bottom). For each case water level is on the left and current speed is on the right.	68
Figure 5.9 Kermadec Trench scenarios in Whitianga. Case 7 (top) and Case 8 (bottom). For each case water level is on the left and current speed is on the right.	69
Figure 6.1 The Tairua wharf.	71
Figure 6.2 Looking inland from near cnr. Manaia and Hapenui Roads.	71
Figure 6.3 (top) looking out of the harbour entrance from Manaia Rd. (bottom) view from the top of Paku Hill.	72
Figure 6.4 (top) View of harbour from Paku Hill. (bottom) Tairua Beach from Paku Hill.	73
Figure 6.5 Views of Pauanui from Paku Hill.	74
Figure 6.6 (top) Pauani from Paku Hill (bottom) Pauanui Beach, view to south showing the width of the setback and the relatively high beach berm.	75

Figure 6.7 (top) View from Pauanui across the harbour entrance to Paku Hill.
 (bottom) inside the Pauanui canals. 76

Figure 6.8 Views of the Pauanui canals. 77

Figure 6.9 Views of the Whitianga water front near the marina entrance. 78

Figure 6.10 (top) Boats parked near the entrance to the Whitianga Marina. (bottom)
 Land for sale near the beachfront at Buffalo Beach. 79

Figure 6.11 Panoramic view of the Buffalo Beach beachfront. 80

Figure 7.1 Inundation at Tairua/Pauanui from Case 5 source scenario..... 81

Figure 7.2 Inundation at Tairua/Pauanui from Case 7 source scenario..... 83

Figure 7.3 Inundation at Tairua/Pauanui from Case 8 source scenario..... 84

Figure 7.4 Maximum current speed at Tairua/Pauanui from Case 5 source scenario.
 85

Figure 7.5 Maximum current speed at Tairua/Pauanui from Case 7 source scenario.
 86

Figure 7.6 Maximum current speed at Tairua/Pauanui from Case 8 source scenario.
 87

TABLE OF TABLES

Table 1.1 Grid details for the Whitianga simulations.	13
Table 1.2 Grid details for the Tairua/Pauanui simulations.	14
Table 2.1 Slip (in m) applied to each of the 27 sub-faults indicated in Figure 2.1 for version 1-6 of the 1960 Chilean earthquake.....	17
Table 3.1 Timing of the maximum withdrawal and maximum positive surge for the 10 unit-source segments shown in Figure 3.27.....	47
Table 3.2 Comparison of arrival times in Whitianga and Tairua.	47

1 INTRODUCTION

This report describes the assessment of tsunami hydrodynamics resulting from tectonic (earthquake) sources at Whitianga and Tairua-Pauanui located on the Coromandel Peninsula of New Zealand (Figure 1.1). The project was designed to update and extend the work of Prasetya et al. (2008), who analysed tsunami inundation at Whitianga from both near and far-field sources.

This study focuses on tsunamis generated by tectonic sources located along the Tonga-Kermadec trench as well as far-field sources located on subduction zones along the Pacific Rim including South America, and Japan. We use the current state-of-the-art tsunami modelling tools (ComMIT: Titov et al. 2011) and the most recent scientific literature on the relevant tsunami source mechanisms. Model results are compared quantitatively and qualitatively to available historical information.

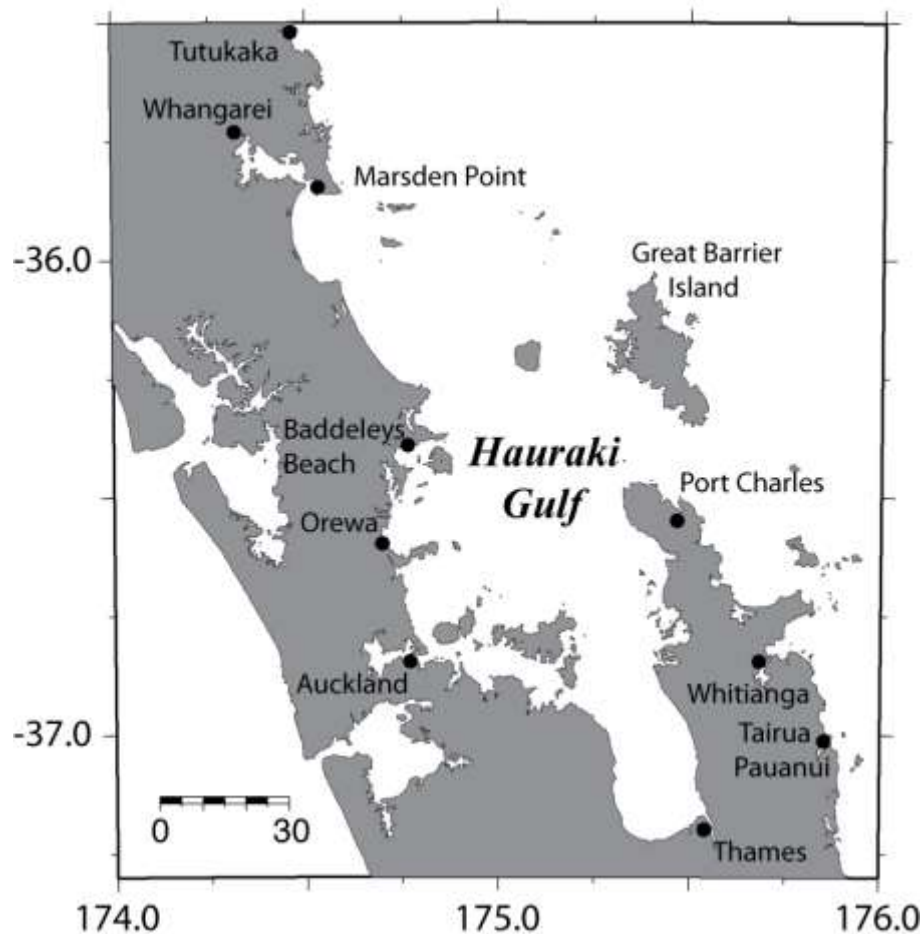


Figure 1.1 The location of Whitianga, Tairua and Pauanui on the east coast of the Coromandel Peninsula.

1.1 Review of Recent Literature

As noted above, this study extends the work of Prasetya et al. (2008) and provides inundation estimates for additional areas along the Waikato coast for both near and far-field sources.

Important results that came from the Prasetya et al. (2008) study include:

- Recognition of the importance of the source data for developing an accurate terrain model. They described the effect of terrain models derived from ground-striking and non-ground-striking LiDAR source data on tsunami inundation.
- Characterising the early onset hazard associated with Tonga-Kermadec trench sources.
- Assessing the relative severity of tsunami effects as it relates to the source mechanism and location.

Since the Work of Prasetya et al., (2008), an additional study by Prasetya and Wang (2011) investigated the recurrence of tectonic tsunami sources located along the Kermadec Trench and in the Bay of Plenty. Their analysis provides a suite of potentially tsunamigenic earthquake sources for the Kermadec Trench and is used as the basis for the modelling presented here.

1.2 Modelling Approach

The numerical modelling presented in this study was carried out using the Community Model Interface for Tsunamis (ComMIT) numerical modelling tool. The ComMIT model interface was developed by the United States government National Oceanic and Atmospheric Administration's (NOAA) Centre for Tsunami Research (NCTR) following the December 26, 2004 Indian Ocean tsunami as a way to efficiently distribute assessment capabilities amongst tsunami prone countries.

The backbone of the ComMIT system is a database of pre-computed deep water propagation results for tsunamis generated by unit displacements on fault plane segments (100 x 50 km) positioned along the world's subduction zones. Currently, there are 1,691 pre-computed unit source propagation model runs covering the world's oceans included in the propagation database. Using linear superposition, the deep ocean tsunami propagation results from more complex faulting scenarios can be created by scaling and/or combining the pre-computed propagation results from a number of unit sources (Titov et al., 2012). The resulting trans-oceanic tsunami propagation results are then used as boundary inputs for a series of nested near shore grids covering a coastline of interest. The nested model propagates the tsunami to shore computing wave height, velocity and overland inundation. The hydrodynamic calculations contained within ComMIT are based on the MOST (Method Of Splitting Tsunami) algorithm developed by Titov and Synolakis (1995, 1998). The ComMIT tool can also be used in conjunction with real time recordings of tsunami waveforms on one or more of the deep ocean tsunameter (DART) stations deployed throughout the oceans to fine tune details of an earthquake source mechanism in real time. An iterative algorithm that selects and scales the unit source segments is used until an acceptable fit to the observed DART data is met.

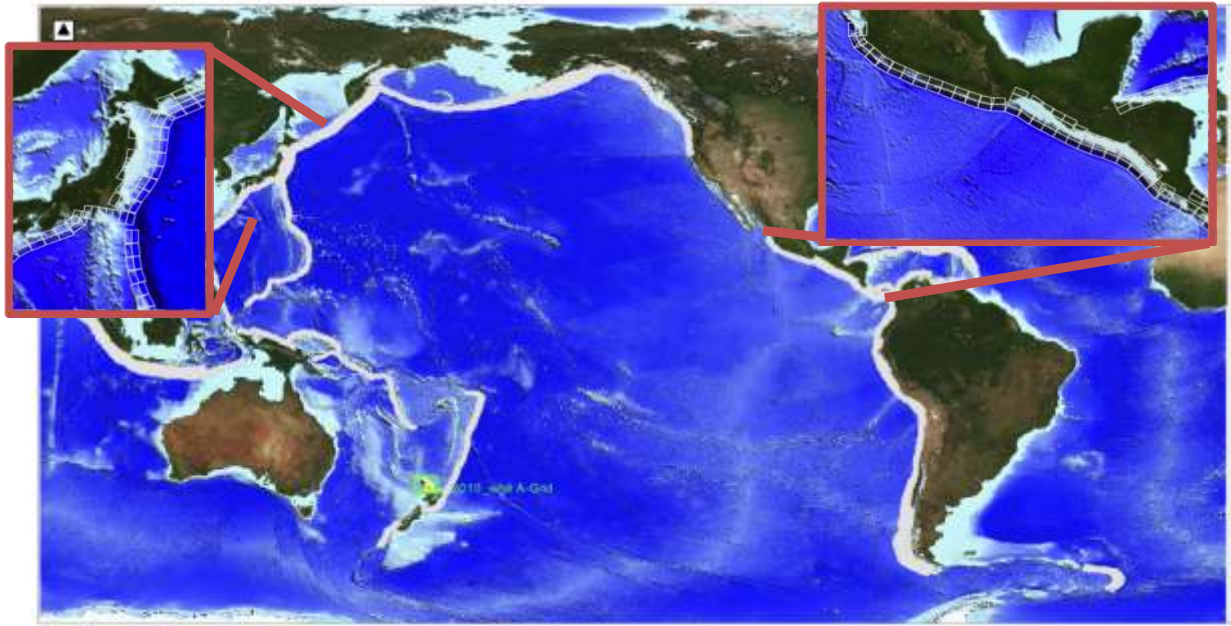


Figure 1.2 The ComMIT propagation model database for tsunamis in the world's oceans. Insets show the details of the source zone discretization in to rectangular sub-faults.

1.3 Numerical Modelling Grids

The MOST hydrodynamic model uses a system of three telescoping nested grids. The outermost ('A') grid has the coarsest resolution while subsequent grid levels (B and C) are a successively higher resolutions. For this study, the outer grids were derived from the GEBCO global bathymetry/topography data set while the inner (B and C) grids were derived from data provided by the Waikato Regional Council. The Whitianga bathymetry sets are essentially the same as those used by Prasetya et al. (2008) while the bathymetry for Tairua and Pauanui was recently developed for this and other studies focused on that area. Grid details are listed in Table 1.1 and Table 1.2 for the Whitianga and Tairua/Pauanui simulations respectively. Plots of the grids are provided in Figure 1.3 and Figure 1.4. For the Whitianga simulations, two outer grids were used to assess the model sensitivity to different grid configurations. This is discussed in Section 3 below.

Table 1.1 Grid details for the Whitianga simulations.

Grid	file name	Nx	Ny	dx (deg)	dy (deg)	spacing (m)
A (1)	WHITIANGA_A2_c.txt	500	500	0.0019	0.0019	~200
A (2)	waikato_A.txt	450	450	0.00667	0.00667	~600
B	WHITIANGA_B2_c.txt	350	361	0.000524	0.00047	~50
C	WHITIANGA_C2_c.txt	500	500	0.0001	0.0001	~10

Table 1.2 Grid details for the Tairua/Pauanui simulations.

Grid	file name	Nx	Ny	dx (deg)	dy (deg)	spacing (m)
A	waikato_A.txt	450	450	0.00667	0.00667	~600
B	TAIRUA_B_50m.grd	251	401	0.00047	0.00047	~42
C	TAIRUA_C_10m.grd	500	500	0.000094	0.000094	~10

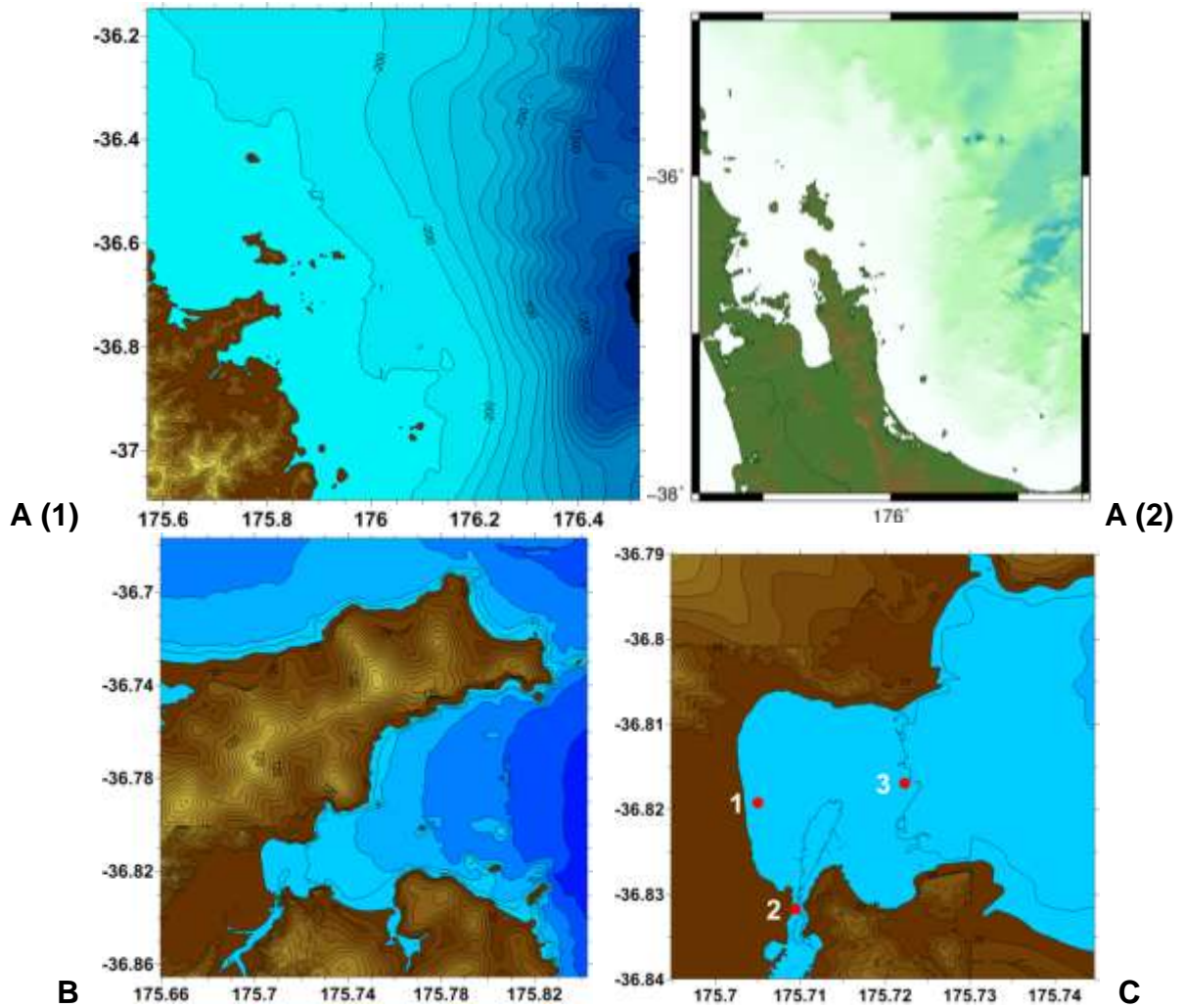


Figure 1.3 Modelling grids used for the Whitianga simulations. Note that two 'A' level grids were trialled in this study.

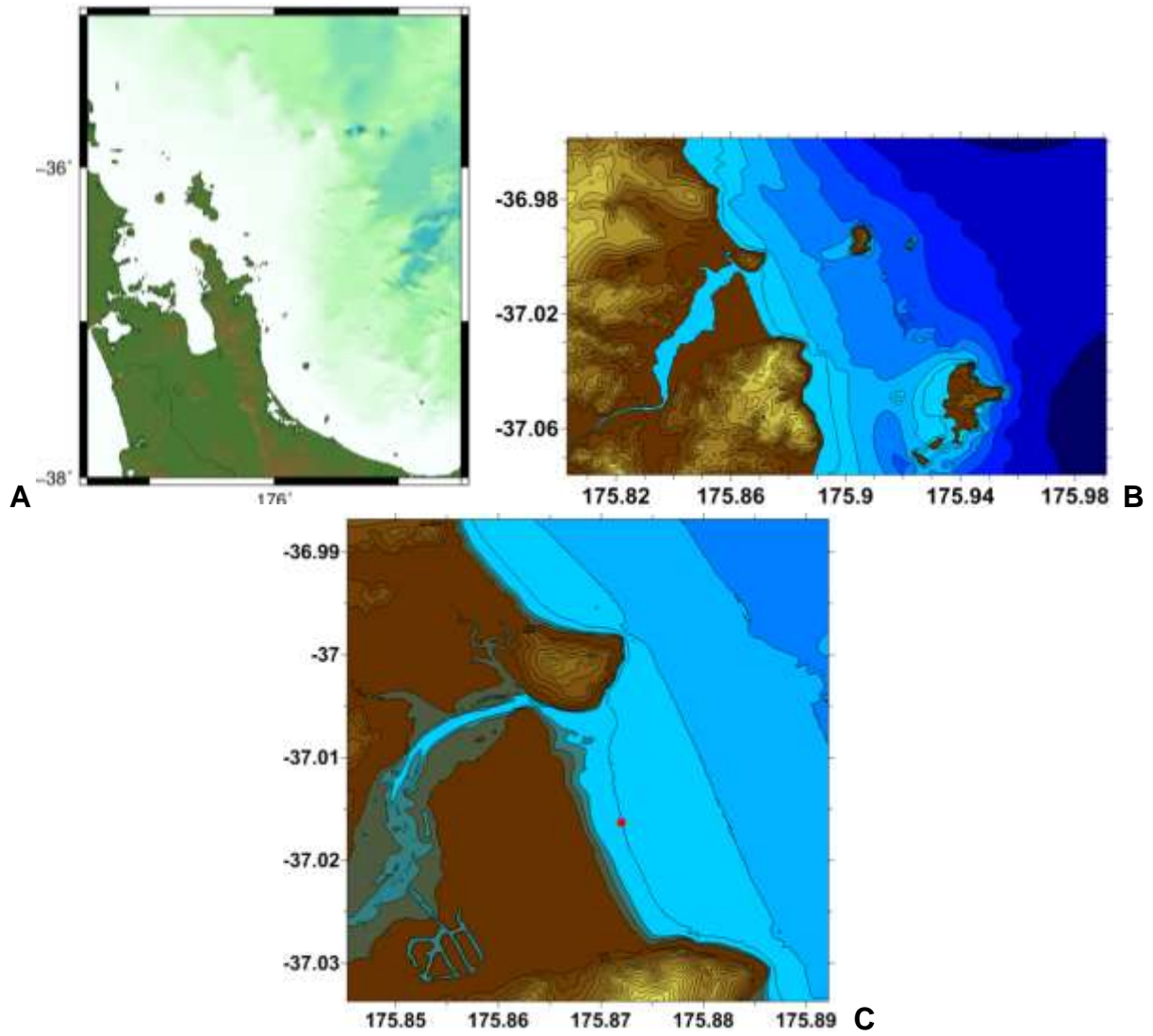


Figure 1.4 Modelling grids used for the Tairua/Pauanui simulations.

2 EARTHQUAKE SOURCE MODELS

For this study we focused on tsunamis generated by tectonic sources including the 1960 Chile earthquake and a range of hypothetical earthquakes on the Kermadec trench, which lies to the east of New Zealand. We also explore the effects of the 2011 Japan earthquake and compare model results to tide gauge data recorded during that tsunami in Whitianga. A final set of scenarios looks at the relative hazard posed by an earthquake similar to the 1960 event, however this source is positioned along the coast of Northern Chile and Peru, in a locations more favourable for wave energy transmission towards New Zealand (Power and Gale 2011).

2.1 1960 Chile Earthquake and Tsunami

The first scenario examined in this study is the 1960 earthquake. The tsunami generated by the 1960 earthquake ($M \sim 9.2$ to 9.5) caused run-up in excess of 25 m in Chile and was observed throughout the Pacific Ocean. The waves caused run-up on the order of 6 m in both Japan and Hawaii and resulted in fatalities in both places. The tsunami was also observed throughout New Zealand, particularly at sites along the east coast such as Lyttelton, Otago Harbor, and Tauranga (Heath 1976). Whitianga also experienced significant effects as detailed in Bell et al. (2004). At all sites where the tsunami was recorded on tide gauge stations, the tsunami was observed as a leading elevation wave (see Heath 1976), where the first motion of the water is positive. This observation makes sense given the earthquake source mechanism which would produce uplift to the west of the South American mainland and subsidence on shore to the east.

Our model of the 1960 Chile earthquake is based on research recently published by Fujii and Satake (2012) who determined a detailed slip distribution for this earthquake based on the analysis of far-field tide gauge recordings in conjunction with estimates of crustal deformation in the near field. We also looked at similarly sized earthquakes with uniform amounts of co-seismic slip applied over the entire fault plane. In total we trialled 6 different source models for the 1960 Chile earthquake. The slip amounts applied to each fault segment in each case are listed in Table 2. and the resulting computed sea floor deformations are shown in Figure 2.2.

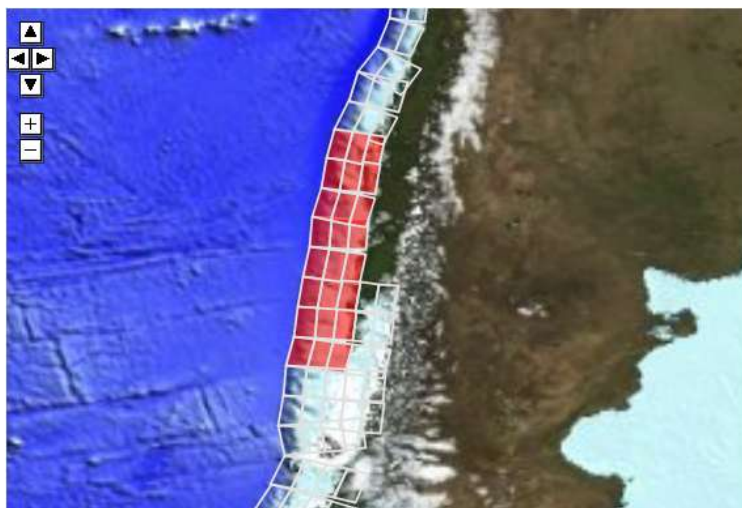
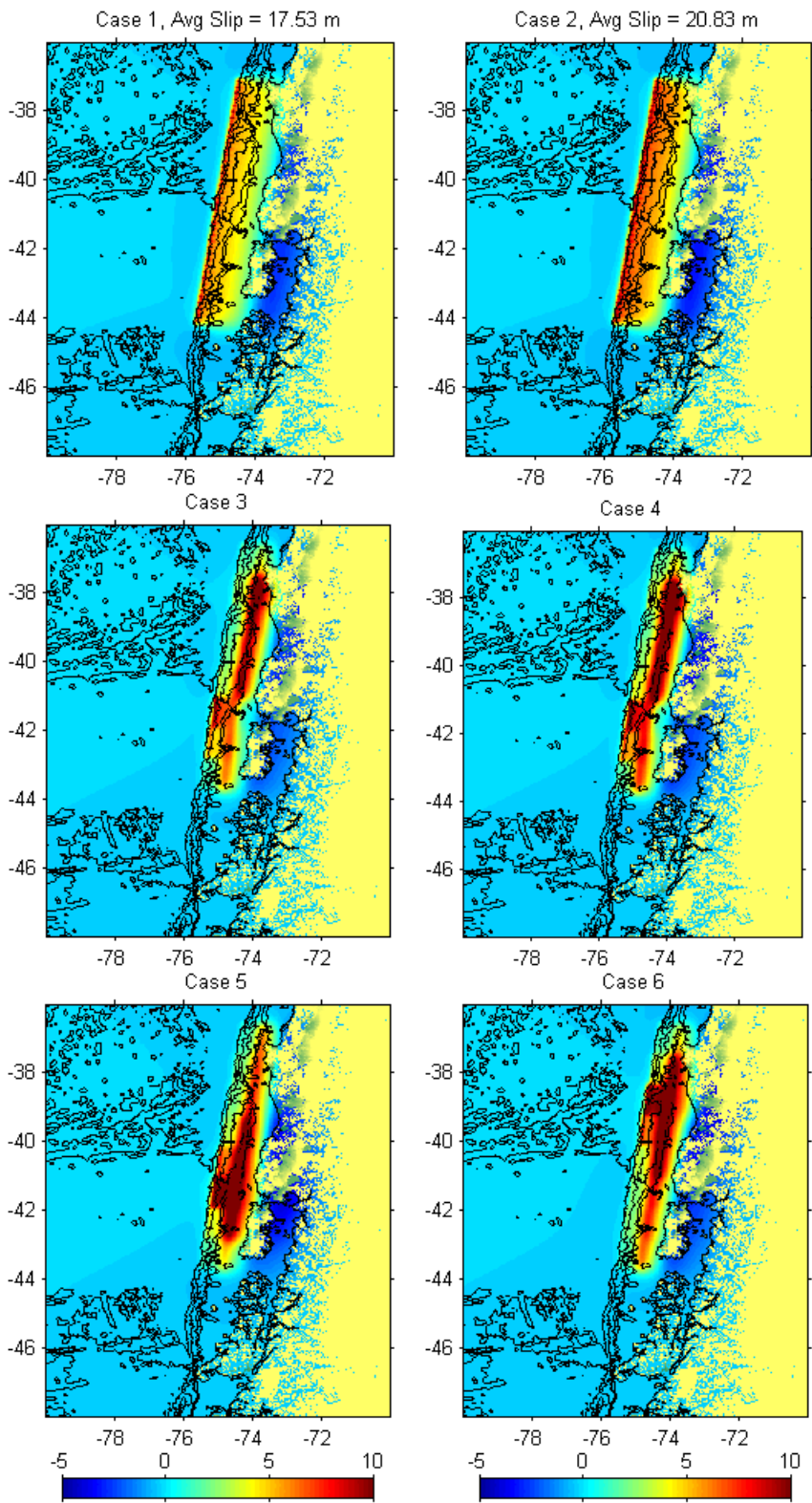


Figure 2.1 Unit source segments used to define the 1960 Chilean Earthquake suite of events.

Table 2.1 Slip (in m) applied to each of the 27 sub-faults indicated in Figure 2.1 for version 1-6 of the 1960 Chilean earthquake.

case 1			case 2		
17.5	17.5	17.5	20.8	20.8	20.8
17.5	17.5	17.5	20.8	20.8	20.8
17.5	17.5	17.5	20.8	20.8	20.8
17.5	17.5	17.5	20.8	20.8	20.8
17.5	17.5	17.5	20.8	20.8	20.8
17.5	17.5	17.5	20.8	20.8	20.8
17.5	17.5	17.5	20.8	20.8	20.8
case 3			case 4		
4.2	10.8	1.0	5.0	12.9	1.2
5.5	30.1	17.5	6.6	36.1	21.0
2.3	25.9	9.4	2.8	31.1	11.3
4.1	24.7	9.6	4.9	29.6	11.5
6.5	27.4	5.5	7.8	32.9	6.6
21.4	14.8	5.1	25.7	17.8	6.2
12.8	18.1	4.6	15.3	21.7	5.5
3.1	17.1	2.3	3.7	20.5	2.7
case 5			case 6		
2.8	17.8	1.2	3.7	12.9	2.7
4.9	20.5	5.5	7.8	29.6	11.3
5.0	21.7	6.2	25.7	36.1	21.0
6.6	31.1	6.6	15.3	32.9	11.5
15.3	32.9	11.5	6.6	31.1	6.6
25.7	36.1	21.0	5.0	21.7	6.2
7.8	29.6	11.3	4.9	20.5	5.5
3.7	12.9	2.7	2.8	17.8	1.2



- Case 1 – average slip 17.5 m
- Case 2 – average slip 20.8 m
- Case 3 – Fujii and Satake (2012) source.
- Case 4 – Fujii and Satake (2012) slip distribution increased by 20%.
- Case 5 - Fujii and Satake (2012) slip distribution increased by 20%, concentrated to south.
- Case 6 - Fujii and Satake (2012) slip distribution increased by 20%, concentrated to north.

Figure 2.2 Six representations of the co seismic deformation associated with the 1960 Chilean earthquake

2.2 Kermadec Trench Scenarios

The Kermadec trench scenarios are based on the work presented in Prasetya and Wang (2011). In that study they presented a number of potential source mechanisms based on an extensive literature review of the tectonics of the Kermadec Trench. For this analysis, we used eight different source models; two M8.9 with ~10.5 m average slip, two M9 earthquake sources with 14.9 m of average slip, two M9.1 sources with 20.9 m of average slip. The sources are shown in Figure 2.3 and Figure 2.5.

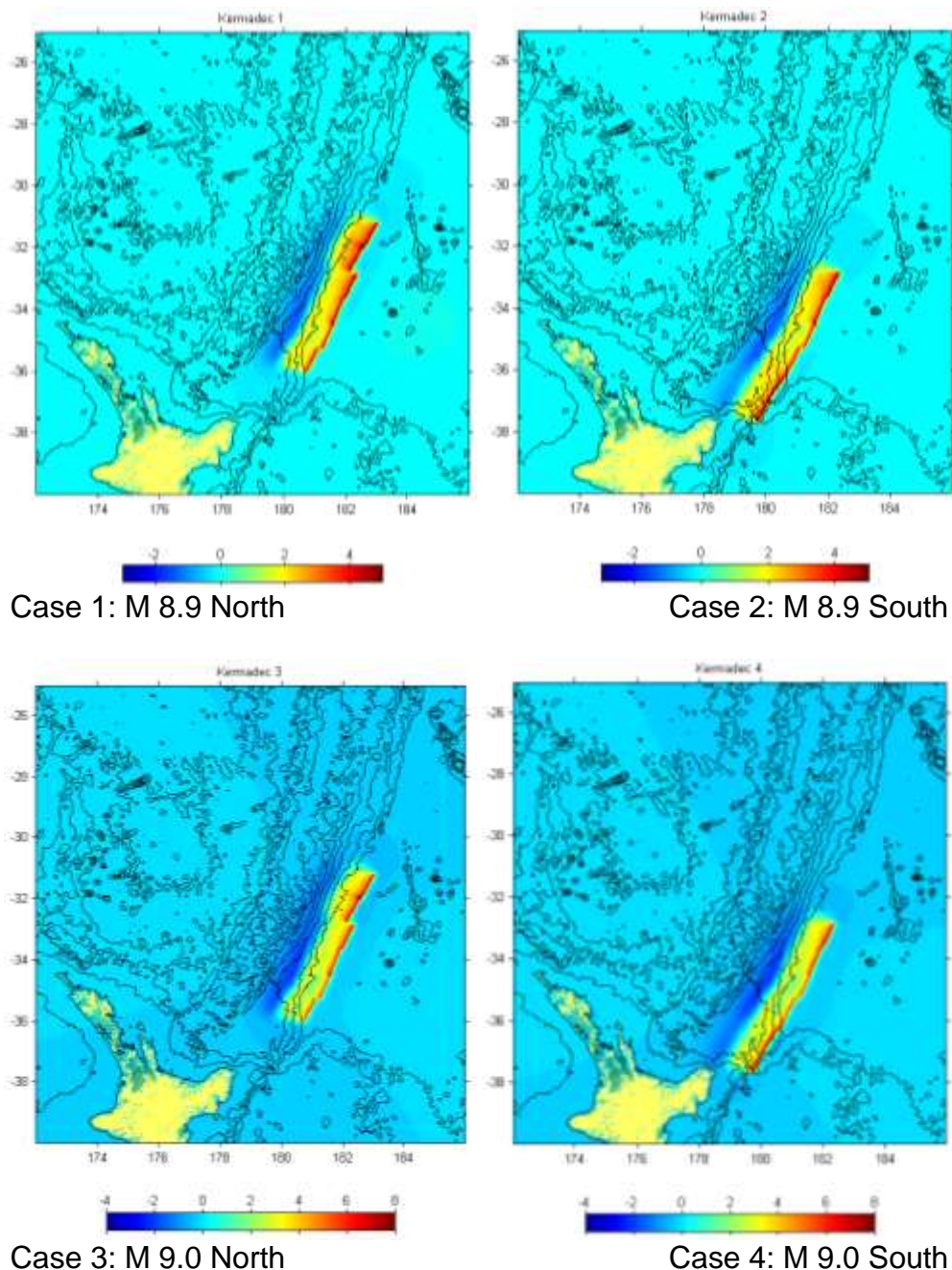


Figure 2.3 Case 1,2: 600 x 100 km fault 10.47 m average slip, M = 8.9. Case 3, 4: 600 x 100 km fault, 14.8 m average slip, M = 9. Note the change in the colour scale for cases 3 and 4.

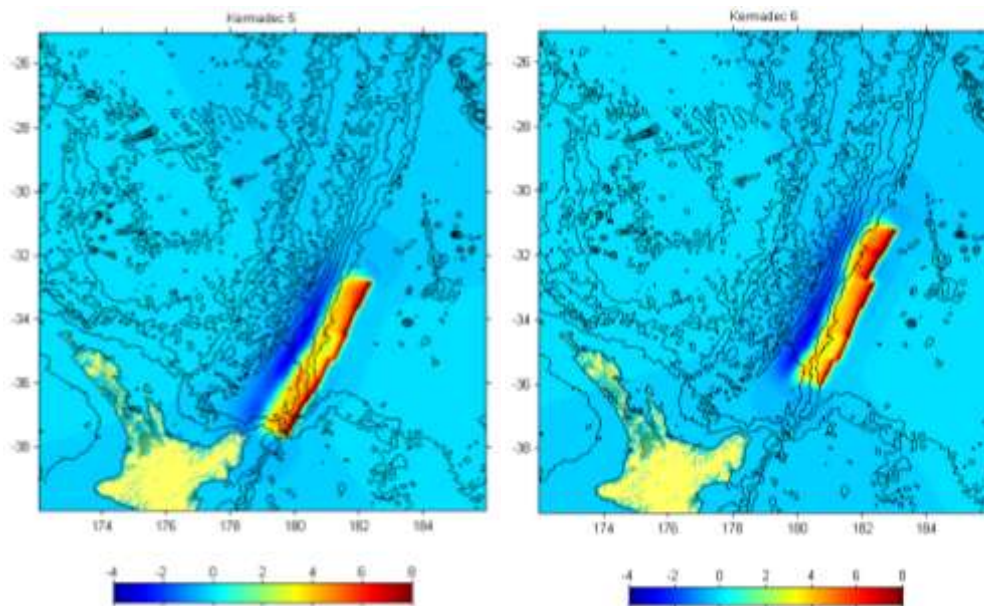


Figure 2.4 Cases 5 and 6: 600 x 100 km fault, 20.9 m average slip, $M = 9.1$

In addition we used one ‘extreme’ source ($M9.3$) with 35 m of slip on the southern segments of the Kermadec trench tapering to 15 m slip 1000 km to the north. The 35 m maximum slip was used as it is roughly equivalent to the maximum slip which occurred during the 1960 Chilean earthquake. The final scenario uses the tsunami source derived for the 2011 Japan event. This source uses variable slip (max of 26 m) spread over a fault length of 400 km and is positioned in the ‘worst case’ location for affecting the Coromandel Peninsula.

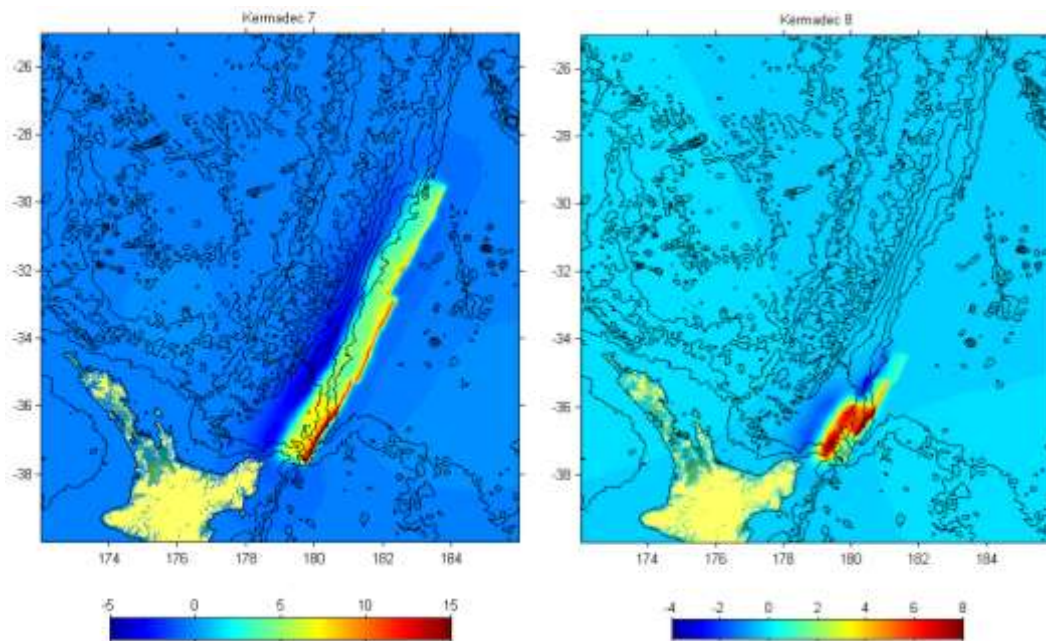


Figure 2.5 Case 7 (left) 1000 x 100 km fault, 35 m max slip at south end of the Tonga-Kermadec Trench ($M = 9.3$). Case 8 (right) the Japan 2011 tsunami source positioned at the southern end of the Tonga-Kermadec Trench ($M=8.81$).

2.3 Additional South American Tsunami Sources: Peru and Northern Chile

Power and Gale (2012) showed that along the South American Subduction Zone, tsunamis generated along the Peru-Chile Border region have a greater impact along the New Zealand coast relative to sources located further to the north or south. Indeed, the 1960 event would have been more damaging in New Zealand had it occurred a few thousand km to the north. Furthermore a very large earthquake (M9) offshore of southern Peru and northern Chile in 1868 generated run-up of 1-4 m in New Zealand (up to 10 m in the Chatham islands) and resulted in New Zealand's only tsunami related fatality since European settlement. The event caused damage to boats and infrastructure along the east coast of the North and South Islands. This event was followed 11 years later by another earthquake of similar magnitude (M9) located further south along the northern coast of Chile. This event however was not as damaging or well observed in New Zealand as the 1868 event. For this reason we felt it was prudent to explore the effects of such an event. The source models we used were based on version 5 and 6 of the 1960 earthquakes described above. We simply translated the identical slip values to fault segments located along the southern coast of Peru to initialise the model.

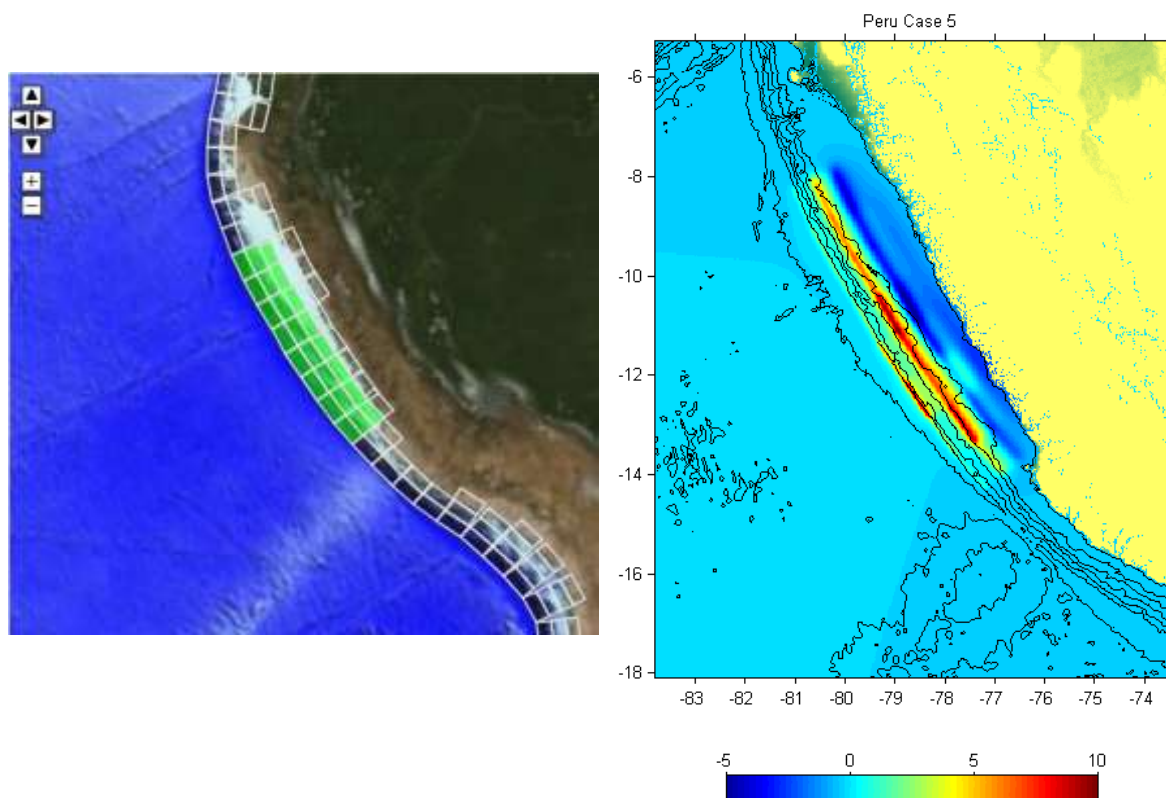


Figure 2.6 Fault segments used to construct the Peru tsunami source (left) and the initial deformation field used to initialise the tsunami model(right).

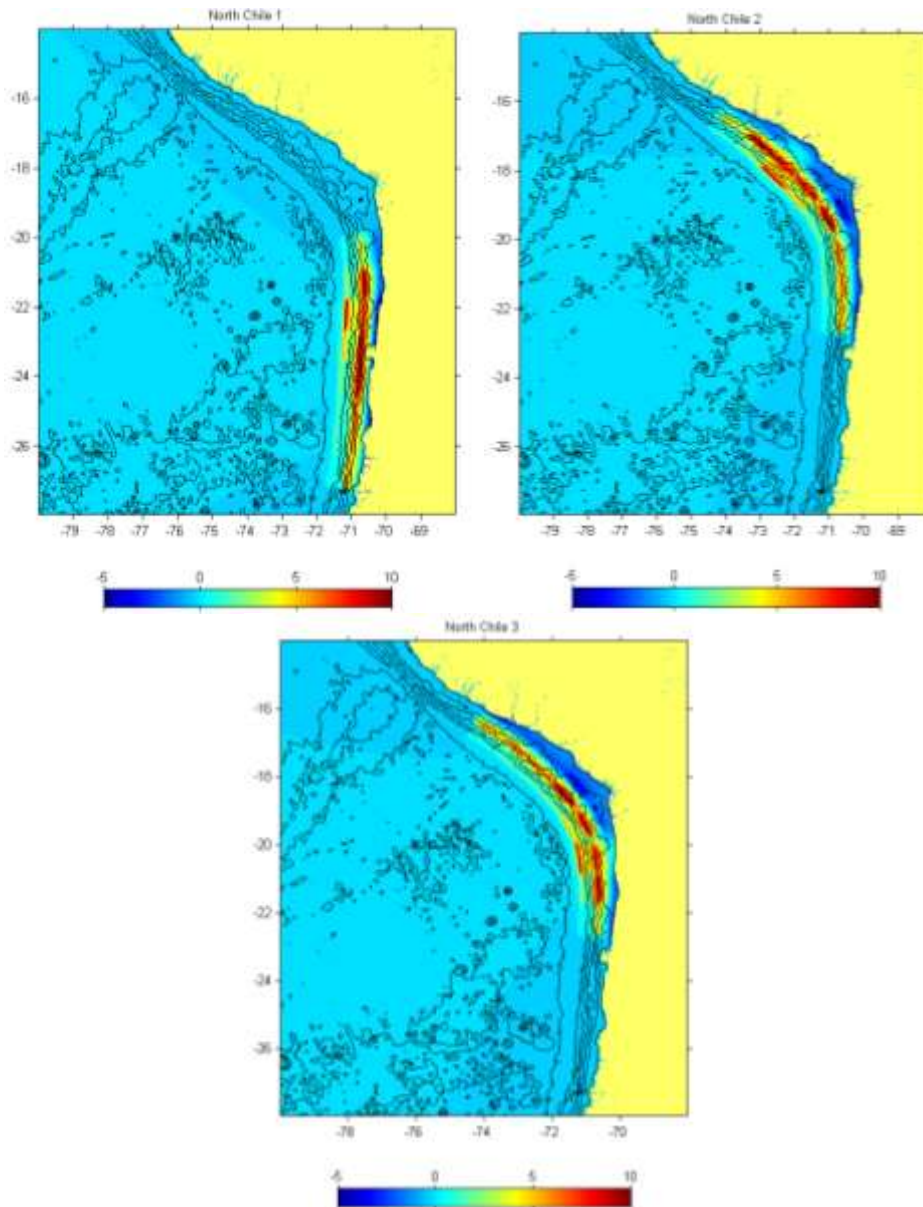


Figure 2.7 Three additional South American sources. Variant of the 1960 Chile earthquake are positioned along the coast of Northern Chile and Southern Peru.

3 MODEL CALIBRATION AND SENSITIVITY ANALYSIS

We used a range of model runs to calibrate and assess the sensitivity of the model to different input parameters. This includes direct comparison to measured tide gauge data from the 2010 Chile and 2011 Japan tsunamis as recorded in Whitianga and a qualitative comparison to the effects from the 1960 tsunami in Whitianga. In terms of model sensitivity, we assess the results as they relate to the grid configuration, source slip distribution, friction parameters and source location.

3.1 Model Grid Configurations

Two grid configurations were used in this study, Grid Configuration 1 and 2 (GC 1, GC 2). The first configuration (GC 1) followed the grid extents used by Prasetya et al. (2008) in their modelling of tsunami inundation at Whitianga, This gridding system features an outermost grid (A grid) that is much smaller in spatial extent than the outermost grid used in GC 2, Both grid configurations use the same B and C level grids, Since this study is aimed at developing an overall modelling system for the Waikato region, we decided to test the performance of a larger outer grid, one that would cover all potential areas of interest for the Waikato Regional Council. By incorporating a larger 'A' grid, we could minimize future gridding needs and simplify forthcoming model runs for other regions of the Waikato Coast. The grid extents are shown in Figure 3.1 and Figure 3.2 and detailed grid parameters are listed in Table 1.1 and Table 1.2.

A third gridding arrangement is presented that was used for the assessment of the 2011 Japan tsunami in Whitianga. These grids, shown in Figure 3.3, were derived by re-sampling and/or linearly interpolating the GEBCO 0.5 min global bathymetry dataset to resolutions of 1 min, 0.25 min and 0.0625 min for the A, B and C grids respectively (Figure 3.3). Grids of this nature were used for the real time assessment of the Japan tsunami in New Zealand as discussed in Borrero et al. (2012). This comparison was done to show the relative accuracy of the model when using highly optimised grids designed to be used in an emergency response capacity and provide accurate results in the shortest time possible.

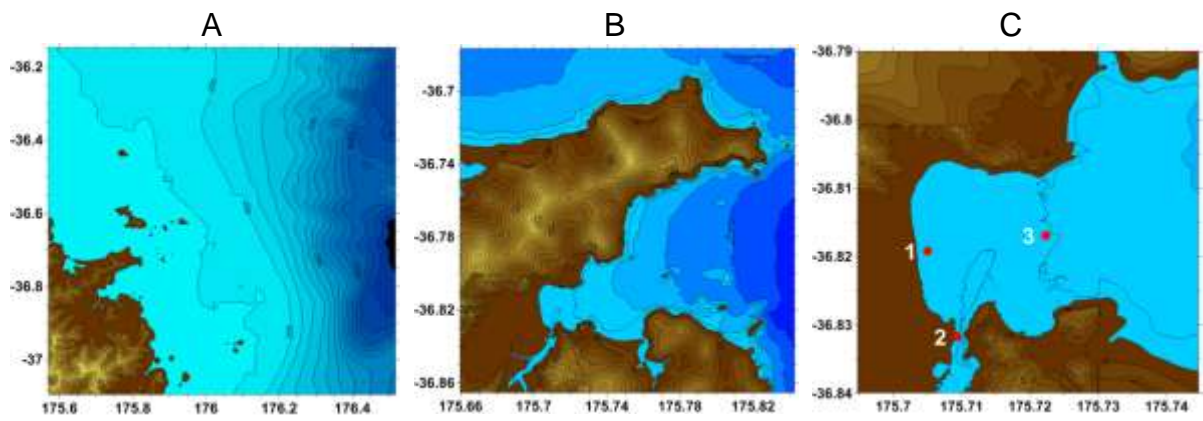


Figure 3.1 Grid configuration 1. Red dots indicate locations where time series data is analysed, Location 2 corresponds to the Whitianga tide gauge.

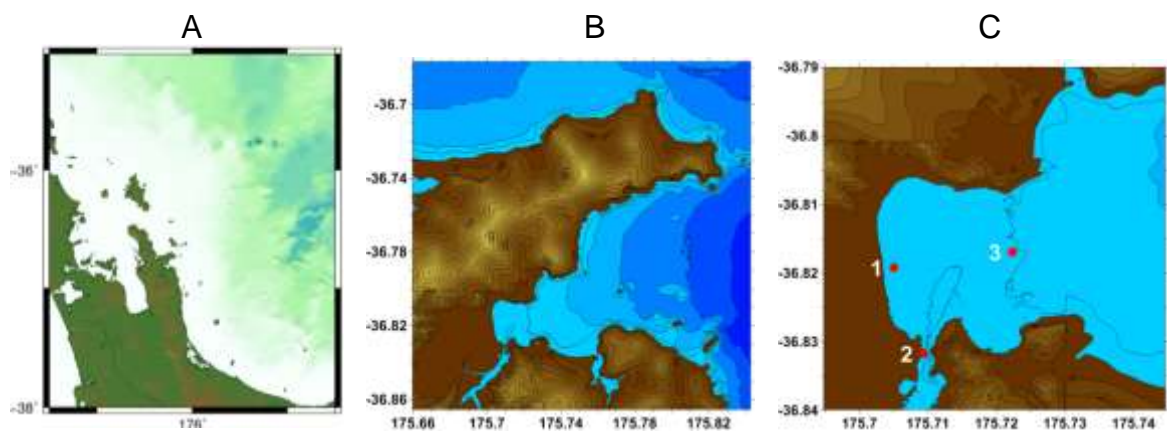


Figure 3.2 Grid configuration 2. Red dots indicate locations where time series data is analysed, Location 2 corresponds to the Whitianga tide gauge.

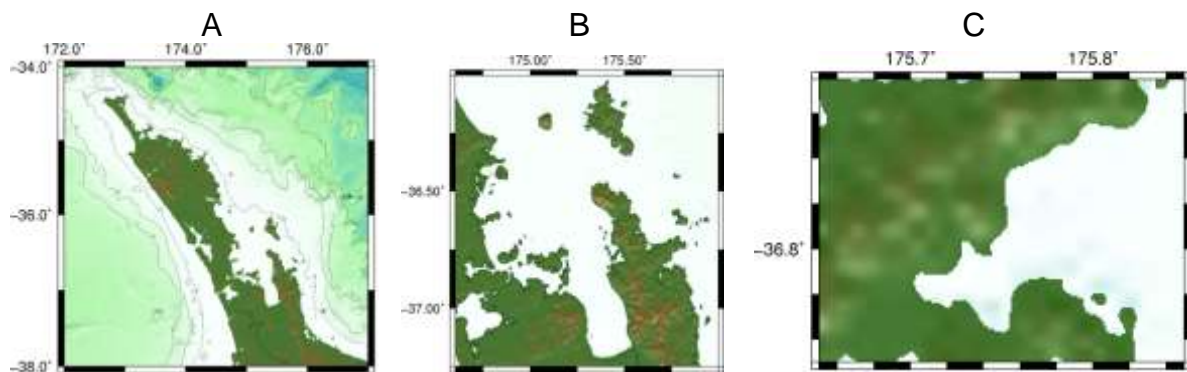


Figure 3.3 Coarse grid configuration.

3.2 Calibration with Japan 2011 tsunami data

Three model runs were compared against tide gauge data recorded in Whitianga during the March 2011 tsunami generated by the Great Tohoku-oki earthquake. While several source models exist for the Tohoku earthquake, for this study we adopted the source determined through the direct inversion of measured tsunami wave forms on DART tsunameter stations located near the earthquake source region (Figure 3.4). This source mechanism was first made available to the global tsunami modelling community just hours after the March 11th, 2011 earthquake and has been used extensively for model assessments in both the near and far-field (Borrero et al., 2012, Wei et al., 2012). This study however is the first to compare model results to measured data on accurate topography as earlier studies (i.e. Borrero et al. 2012) used highly idealised bathymetry derived by linearly interpolating coarse resolution global bathymetry data sets.

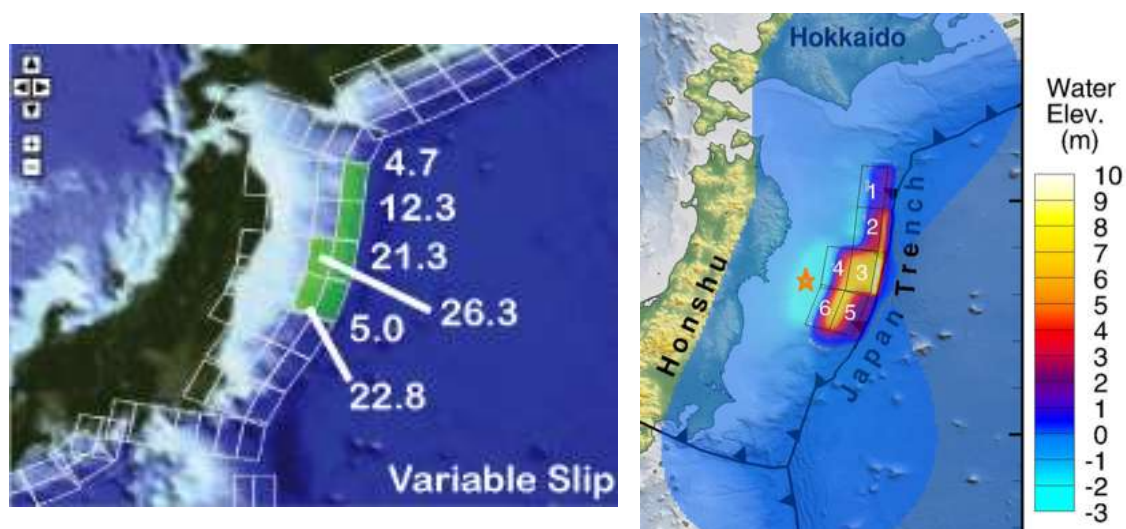


Figure 3.4 Source model used for the 2011 Tohoku tsunami, The amount of slip on each segment is indicated in the left panel, while the vertical deformation of the sea floor is shown on the right (image reproduced from Wei et al., 2012).

Figure 3.5 compares the model results to measured data at three locations in Mercury Bay (the locations are indicated in Figure 3.1 and Figure 3.2 with red dots). Of the three cases, GC 2 provides the best fit to the measured data. It captures the initial oscillations in the first hour after arrival, there is a very good fit in the time interval between 15 and 20 hours and the late arriving surges from 20 to 22 hours are also well represented.

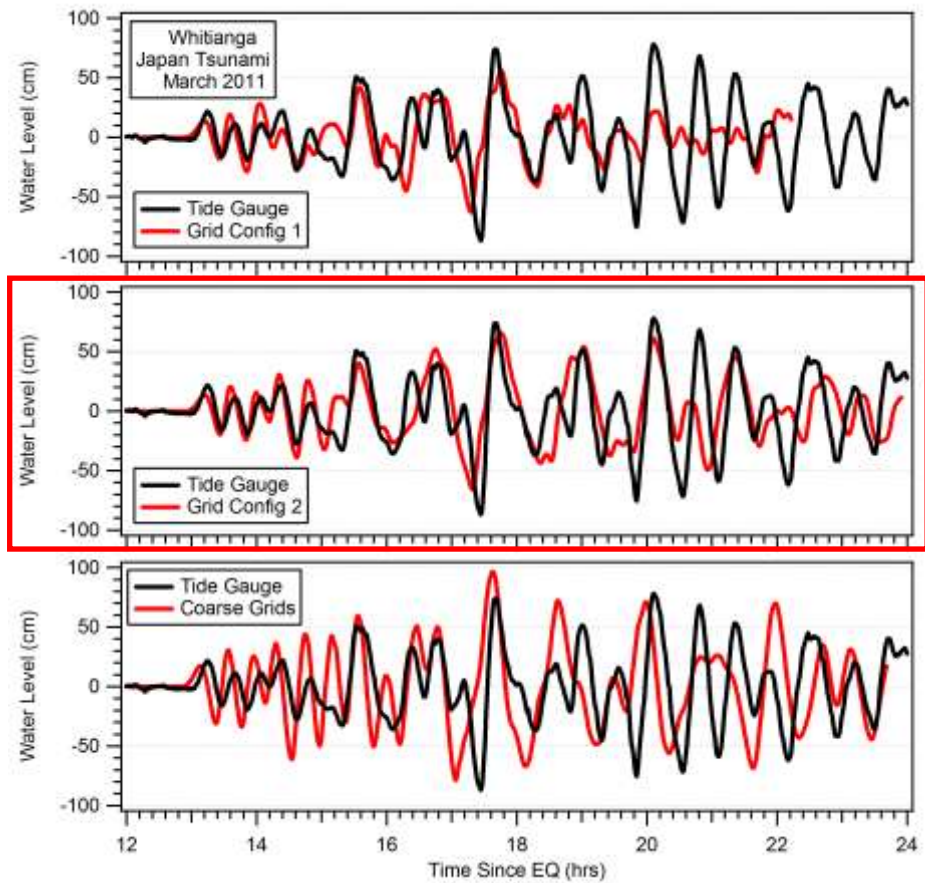


Figure 3.5 Comparison between modelled and measured water levels in Whitianga during the March 2011 Japan tsunami. The results from Grid Configuration 2 (highlighted in the red box) provide a better comparison to the tide gauge data.

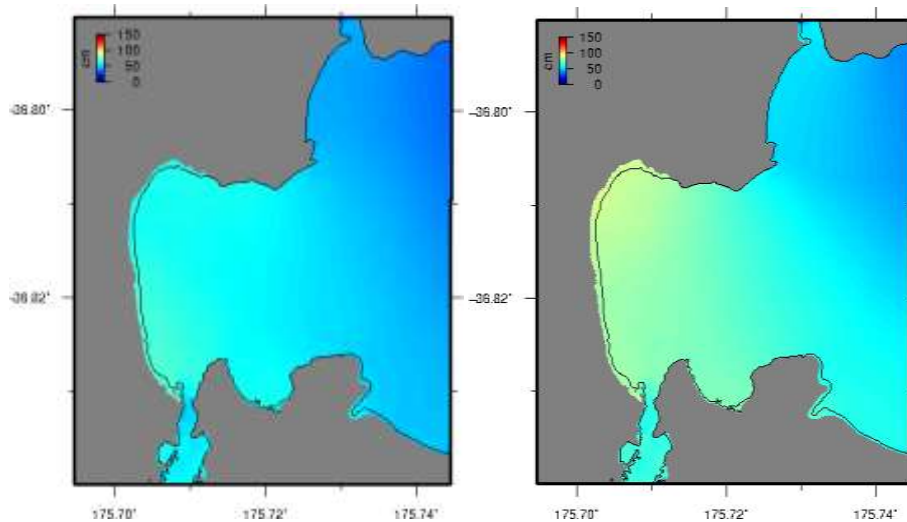


Figure 3.6 Maximum computed water levels for the Japan 2011 tsunami in Mercury Bay using Grid Configuration 1 (left) and Configuration 2 (right).

3.3 The February 2010 Chile Tsunami

On February 27, an earthquake with a magnitude of 8.8 (M_w , United States Geological Survey) occurred in the coastal area of southern Chile. The earthquake caused a destructive tsunami in Chile and a moderate tsunami that was observed throughout the Pacific Ocean. The tsunami was clearly evident in Whitianga and resulted in the closure of the Whitianga Marina for 2 days. Witnesses state that the effects from the 2010 event were stronger than the 2011 Japan tsunami (Borrero et al., 2012). The source mechanism used for this simulation was determined through the inversion of DART tsunameter data (NOAA/PMEL, *pers. comm.*). However, their result was based on only 1 tsunameter record that was located significantly off-axis from the primary lobe of tsunami energy propagation and may not be totally accurate. In contrast the DART constrained tsunami source for the 2011 Japan tsunami was based on three tsunameters, each favourably located for the source inversion (Wei et al., 2012). Nevertheless, the fit between the model and measured data is quite good in terms of timing and amplitude, but the signals fall out of phase approximately 2 hours after tsunami arrival.

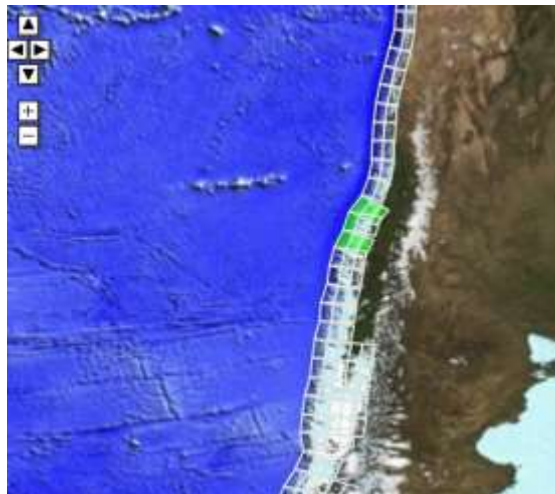


Figure 3.7 Source segments used for the 2010 Chile tsunami.

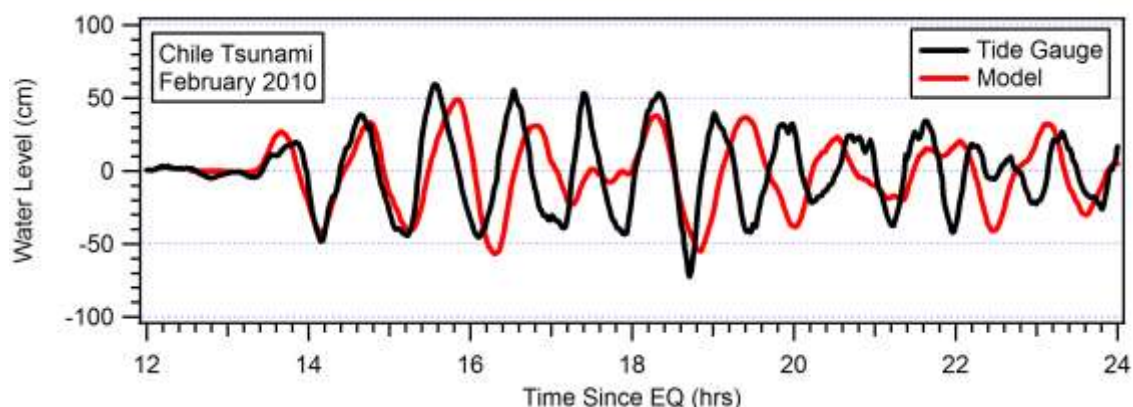


Figure 3.8 Comparison between measured and modelled water levels at the Whitianga tide gauge for the February 2010 Chile earthquake and tsunami. Simulation run on Grid Configuration 2.

3.4 1960 Chile tsunami

The 1960 Chile earthquake caused the strongest tsunami to have affected New Zealand in the modern era. At Whitianga, a number of eyewitness accounts describe the effects of the tsunami as well as the inundation in Whitianga and along the beaches of Mercury Bay.

3.4.1 Effect of Grid Configuration

We first compared model results at Whitianga between GC 1 and GC 2. For this comparison, we are using the 1960 Case 6 scenario. Figure 3.9 shows that the model results do not display a significant difference for the first two wave cycles (approx 2 hrs after arrival). After this, the solutions diverge, with GC 2 producing larger predicted wave heights between 2 and 5 hours after arrival. Both grids then respond with a larger series of surges that occurs approximately 5 to 7 hours after arrival. The occurrence of these surges is somewhat similar to the late arriving surges seen on the tide gauge recording for Whitianga from the 2011 Japan tsunami. This highlights the well known and documented resonant nature of Mercury Bay.

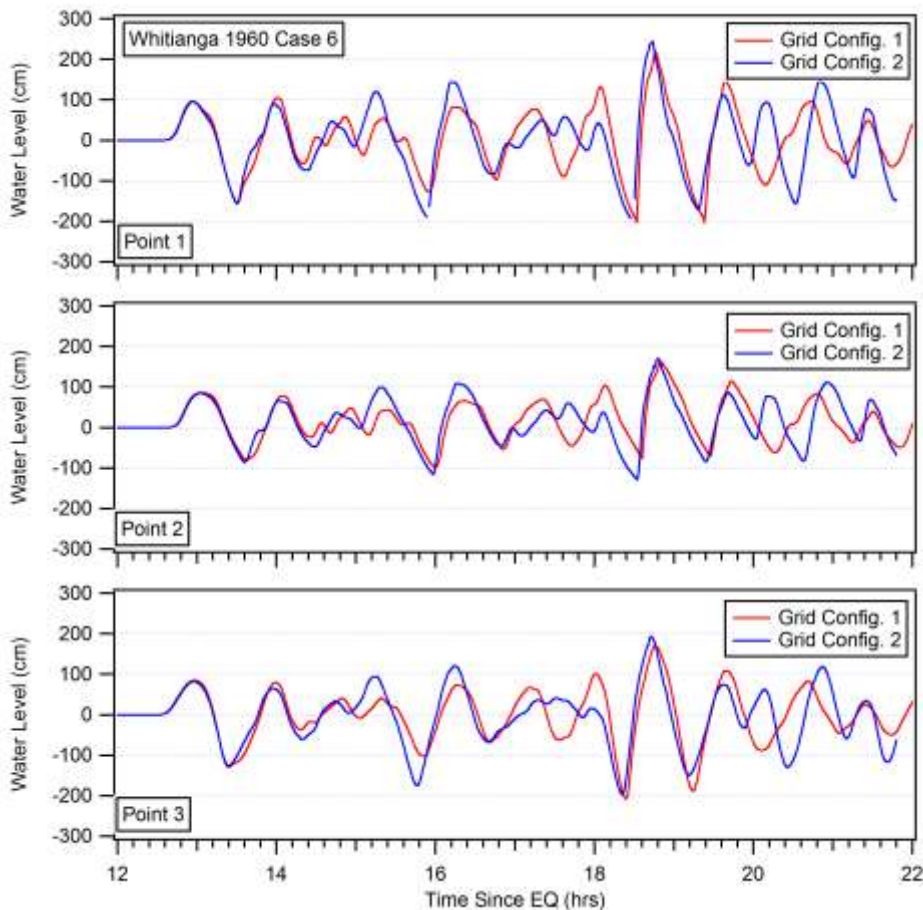


Figure 3.9 Comparison between model results for the two grid configurations at three locations in Whitianga using a Chile 1960 source.

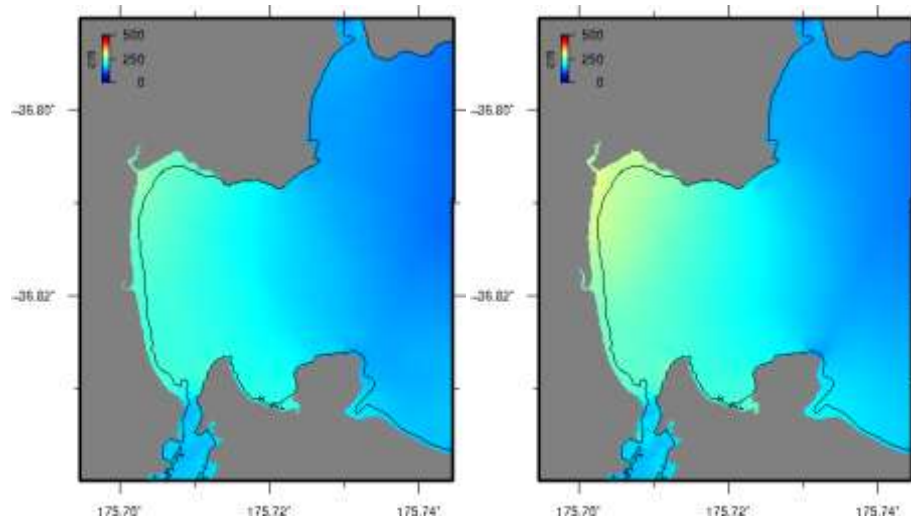


Figure 3.10 Maximum computed water levels in Mercury Bay for Case 6 of the 1960 Chilean earthquake scenarios. GC 1 (left) and GC 2 (right).

3.4.2 Effect of slip distribution

Figure 3.11 plots the modelled water level at the Whitianga tide gauge for each of the 6 different source models of the 1960 Chilean Tsunami (see Section 2.1 above) for both Grid Configurations. It is evident from the figure that the details of the slip distribution have only a secondary effect on the overall modelled water levels. Recall that Cases 1 and 3 are the smallest in terms of magnitude (i.e. slip amount), Cases 4, 5 and 6 are identical in terms of the overall slip amount. The variability in the predictions is approximately 30 cm over a maximum water level variation of 230 cm. Furthermore, the phase of the waves becomes remarkably constant approximately 3 hours after tsunami arrival. The plots show that while Mercury Bay does have this overall effect on the time series, the slip distribution does have some effect on the finer details of the water level signal, this will be discussed in greater detail below when we assess the model results as they relate to eyewitness accounts of the 1960 Chilean tsunami.

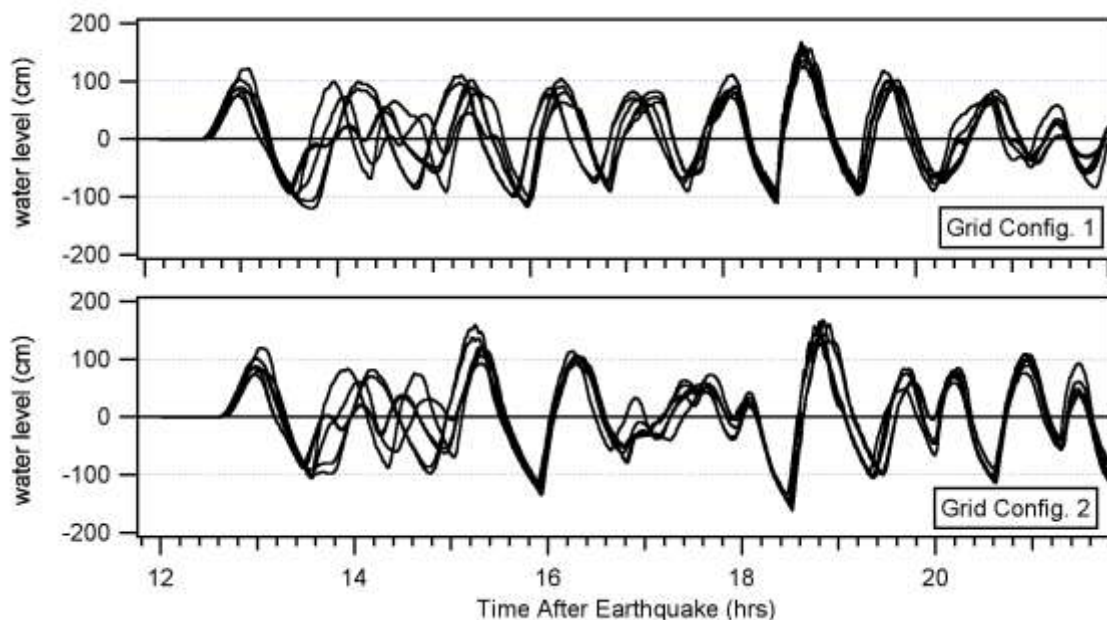


Figure 3.11 Modelled water levels at the Whitianga tide gauge resulting from 6 different versions of the 1960 Chile earthquake source model.

3.4.3 Effect of Friction Coefficient

The MOST hydrodynamic model used in the ComMIT modelling package uses a constant bed friction based on Manning's n friction coefficient. A value of 0.03 is the default used in the model. We also set up a simulation using a lower friction setting of 0.021 (noted as 'f2' in the plots below). The results are compared in Figure 3.13 for the 1960 Chilean tsunami showing that the lower friction leads to elevated wave heights and slightly increased inundation. We also note however that the lower friction setting leads to slight instabilities which appear at the crests and troughs of the largest surges. These are evident in Figure 3.12, particularly in the Case 6 run at the wave trough and crest occurring in hour 18-19 of the simulation.

The effect of the friction coefficient is illustrated over the entire bay in Figure 3.13 through Figure 3.16 where we compare modelled maximum water levels and current speeds throughout Mercury Bay. The lower friction does result in higher water levels, but also results in somewhat unrealistic current speed results as seen in Figure 3.15 and Figure 3.16.

To assess the effect of the friction coefficient on a scenario for which we have instrumental data available, we modelled the 2011 Japan tsunami using the GC 2 bathymetry and the Manning friction coefficients noted above. The results shown in Figure 3.17 and Figure 3.18 again show that the friction coefficient does not have a strong impact on the time series extracted from the tide gauge location. There is however a strong effect on the modelled current speeds with the lower friction setting giving what we suggest are unrealistic speeds jetting out of the harbour and into Mercury Bay.

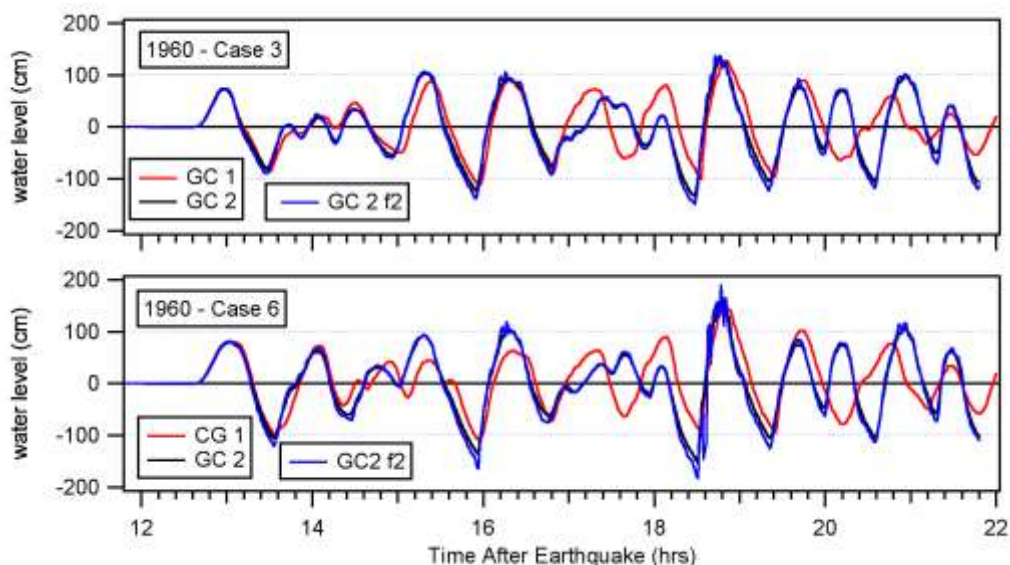


Figure 3.12 The effect of the friction coefficient on water levels at the Whitianga tide gauge location for Case 3 and Case 6 of the 1960 Chilean tsunami sources. The GC2 and GC2f2 results are nearly indistinguishable from one another and appear as one trace on the plot.

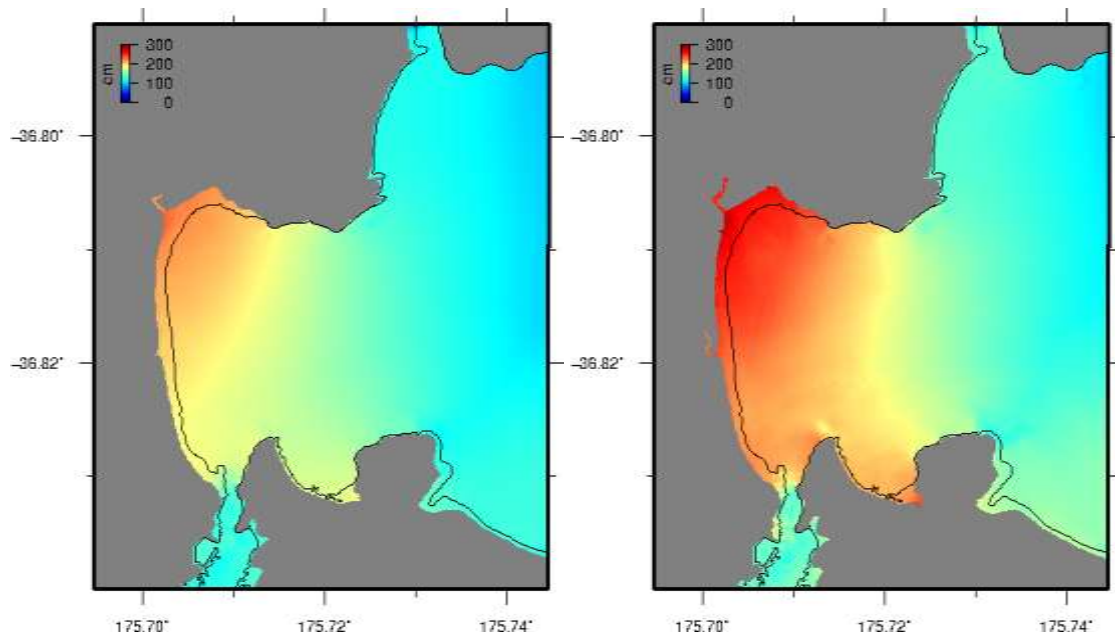


Figure 3.13 Maximum computed water levels in Mercury Bay for Case 3 of 1960 Chilean earthquake scenarios on Grid Configuration 2. A friction factor of 0.03 is used on the left and 0.021 on the right.

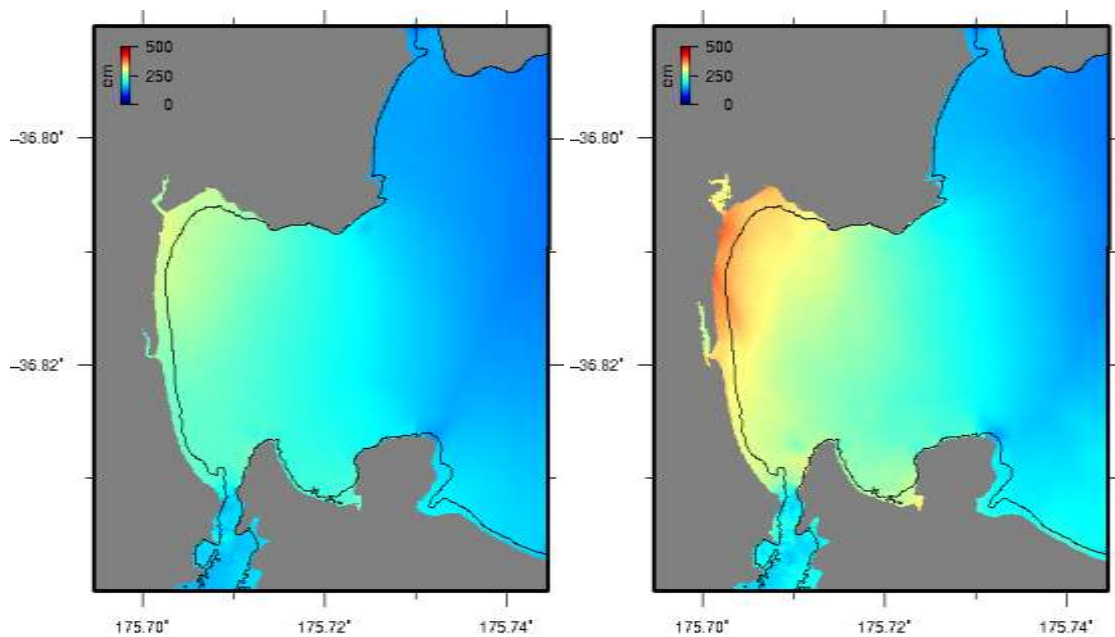


Figure 3.14 Maximum computed water levels in Mercury Bay for Case 6 of 1960 Chilean earthquake scenarios on Grid Configuration 2. A friction factor of 0.03 is used on the left and 0.021 on the right. Note: the colour scale has changed from the previous figure.

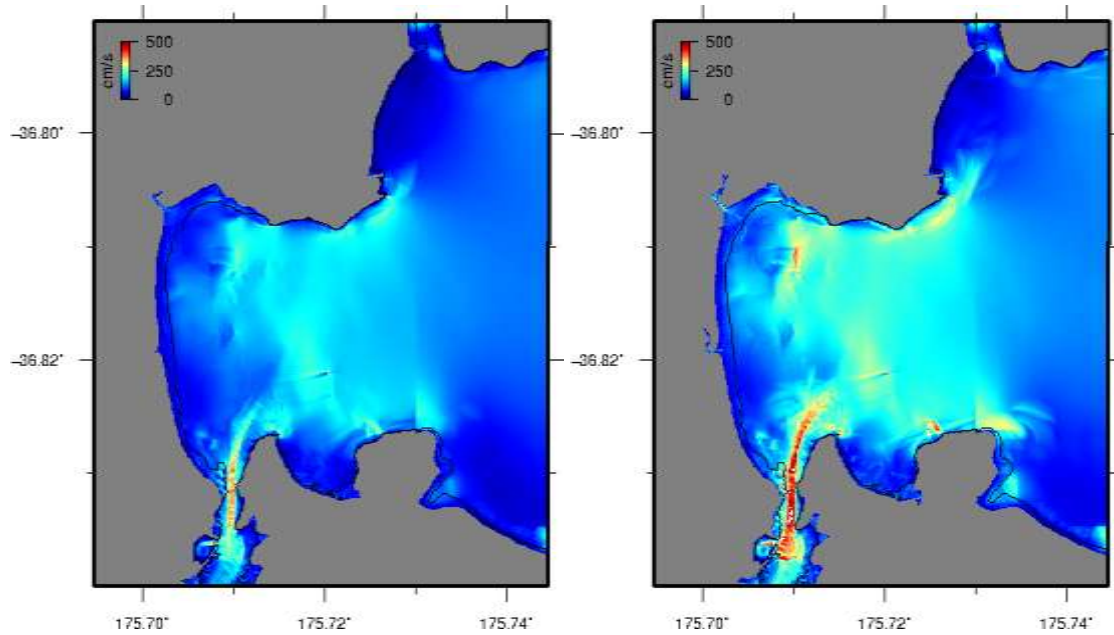


Figure 3.15 Maximum computed current speed in Mercury Bay for Case 3 of 1960 Chilean earthquake scenarios on Grid Configuration 2. A friction factor of 0.03 is used on the left and 0.021 on the right.

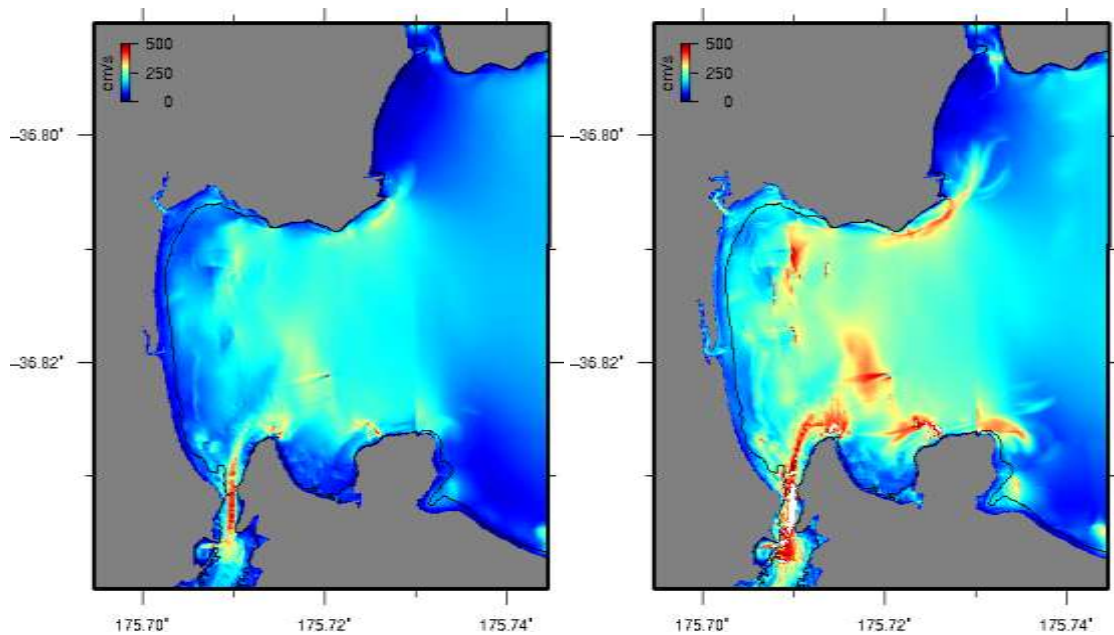


Figure 3.16 Maximum computed current speed in Mercury Bay for Case 6 of 1960 Chilean earthquake scenarios on Grid Configuration 2. A friction factor of 0.03 is used on the left and 0.021 on the right.

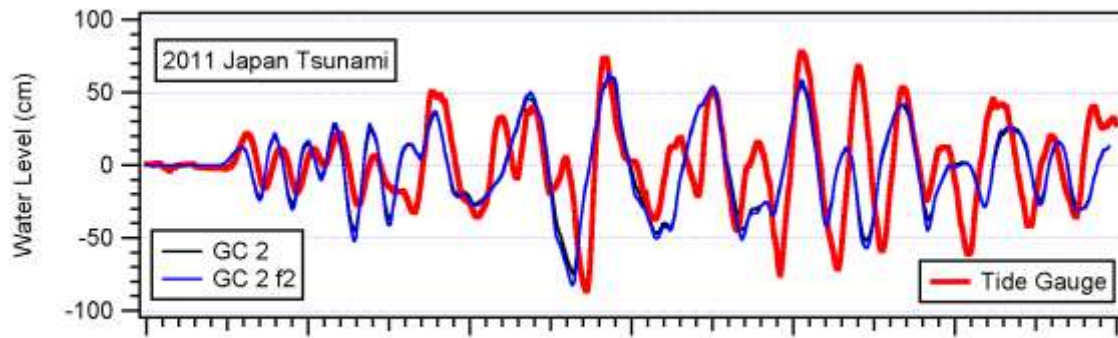


Figure 3.17 The effect of friction setting on modelled water levels at the Whitianga tide gauge for the 2011 Japan tsunami. The two time series from the model are virtually indistinguishable from one another and appear as one blue trace on the plot.

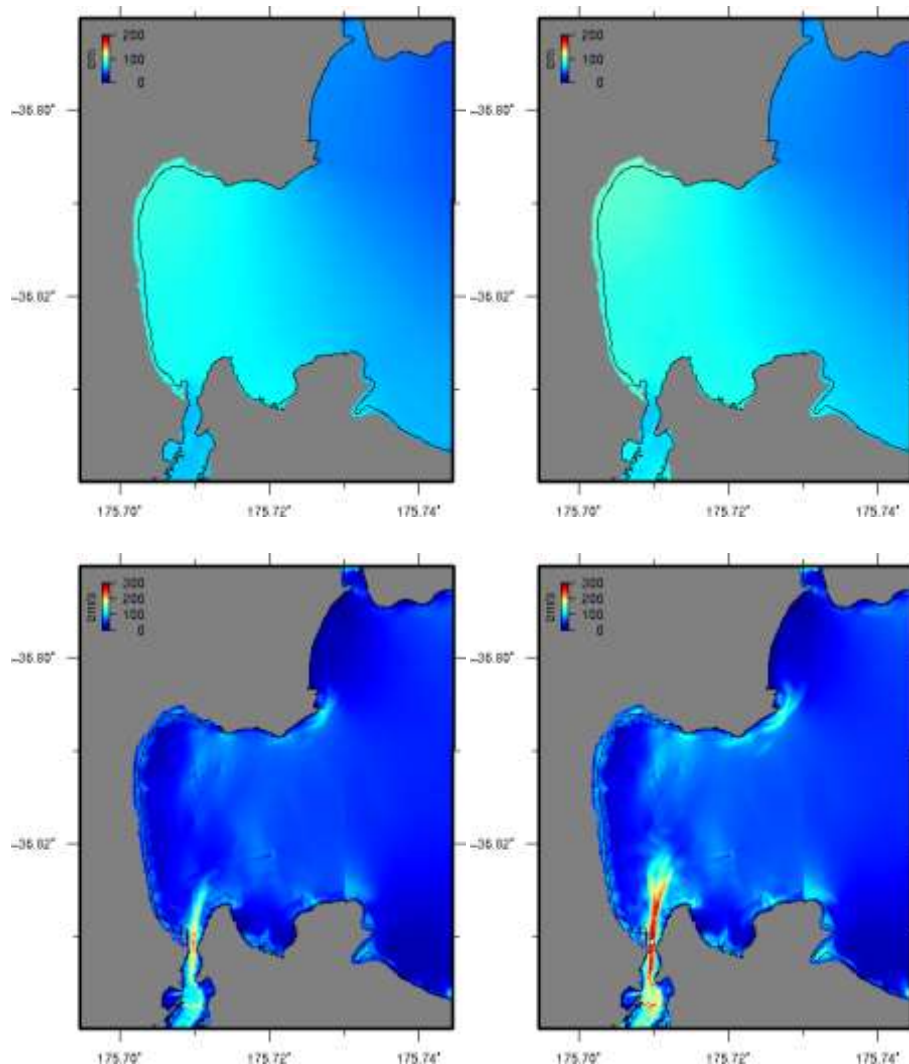


Figure 3.18 The effect of friction setting on modelled water levels and current speeds in Buffalo Bay for the 2011 Japan tsunami.

3.4.4 Qualitative Comparison to Historical Accounts

Eyewitness accounts of the effects of the 1960 Chile tsunami in Whitianga were reproduced by Bell et al. (2004) who sourced a testimonial by H.W. Pasco and others from the New Zealand Nautical Almanac. An additional eyewitness account (Mr. Bruce Smith) was also provided for this study by staff at the Waikato Regional Council (Vernon Pickett, pers. comm.). These testimonies provide some insight in to the character of the tsunami inundation overnight from May 23 to May 24, 1960. We present these reports in conjunction with modelling results and tide data for that time period. Historical tidal sea level data were extracted from a world tidal model (Egbert et al., 1994). The world tide model consists of a $\frac{1}{4}$ degree worldwide grid of the 8 most influential tidal constituents derived from 14 years of satellite altimeter data.

In his account of the event, Mr. Smith states that he first observed the tsunami effects around 9:30 pm on May 23. At that time he stated that ***'the tide came in and out at a fast rate'***. After this initial observation, another vessel took Mr Smith out to his boat which was moored in the harbour. He noted multiple surges over the next hour as he worked to pump water out of the boat which was leaking due to damage sustained during the first hours of the tsunami. Around midnight he made the decision to beach the vessel if it broke free from its mooring. At 2:30 am, a strong incoming surge did just that, as it pushed the nose of his vessel underwater until the mooring line gave way. He momentarily lost control of his boat and was nearly thrown overboard, however he regained control and managed to beach the vessel on a town street ***'approximately 50 m from the Whitianga Pub's front door'***. This location was described in the Pascoe account as being ***'on to the road on the wharf side of Karena Creek'***.

The best description of the inundation comes from the Pascoe account which states that ***'the sea came up Monk Street to where the Power Station was and up to the Dairy Company front office steps'***, he also noted that there was inundation ***'into the old aerodrome hangar along the northern end of Buffalo Beach, where it wet crates of corrugated iron stored on the floor damaging them'***. Pascoe's account also gives some indication of the current speed when he states that a vessel he was handling was ***'doing 12 knots and going backwards'*** due to an incoming surge. He adds that they continued to move backwards for ***'20 minutes until the tide turned and swept us out through the entrance to safety'***. He also notes that ***'about 2 am on Tuesday morning [...] seemed to be the worst time'***. The Pascoe account also describes the weather as ***'very fine'*** with ***'practically no wind or swell outside in the Bay'***.

Mr. Smith's account of multiple surges around 9:30 pm matches with the model results for Case 3 and Case 4 (Figure 3.20). We note that Cases 3 and 4 were based on a slip distribution that had been rigorously constrained by far field tide gauge data and near field geodetic data (Fujii and Satake, 2012) with Case 4 being the same as Case 3, just with slip increased by 20%. The uniform slip source models (Case 1 and 2) produce results which appear to have more regular oscillations and less apparent higher frequency component. Cases 5 and 6, which concentrated the slip either to the south or the north of the fault plane, do contain some higher frequency signals, however, neither one has this high frequency feature around 9 pm as noted by Mr. Smith.

We also note that the model results are consistent with the observation by the two witnesses that the largest and strongest surges happened around 2 am on May 24. This effect can be seen in the results from all of the source models (Figure 3.19 and Figure 3.20) and on both Grid Configurations (Figure 3.11).

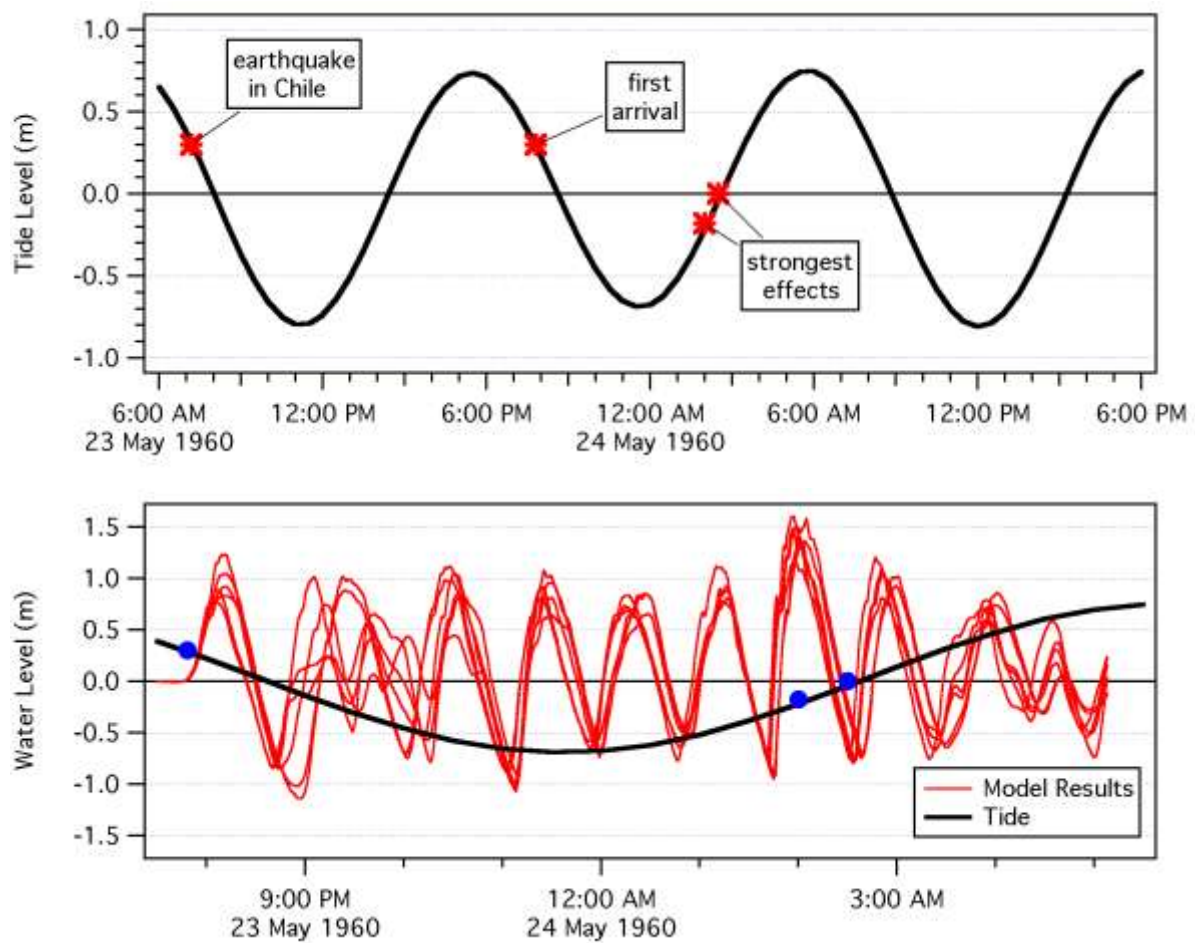


Figure 3.19 (top) The predicted tide on the day the 1960 Chile tsunami affected Whitianga. Important times are marked and noted. **(bottom)** Model results (red) for the six source models compared to the predicted tide level. (black) Blue dots indicate the modelled arrival time and the time when the worst effects were observed by the witnesses.

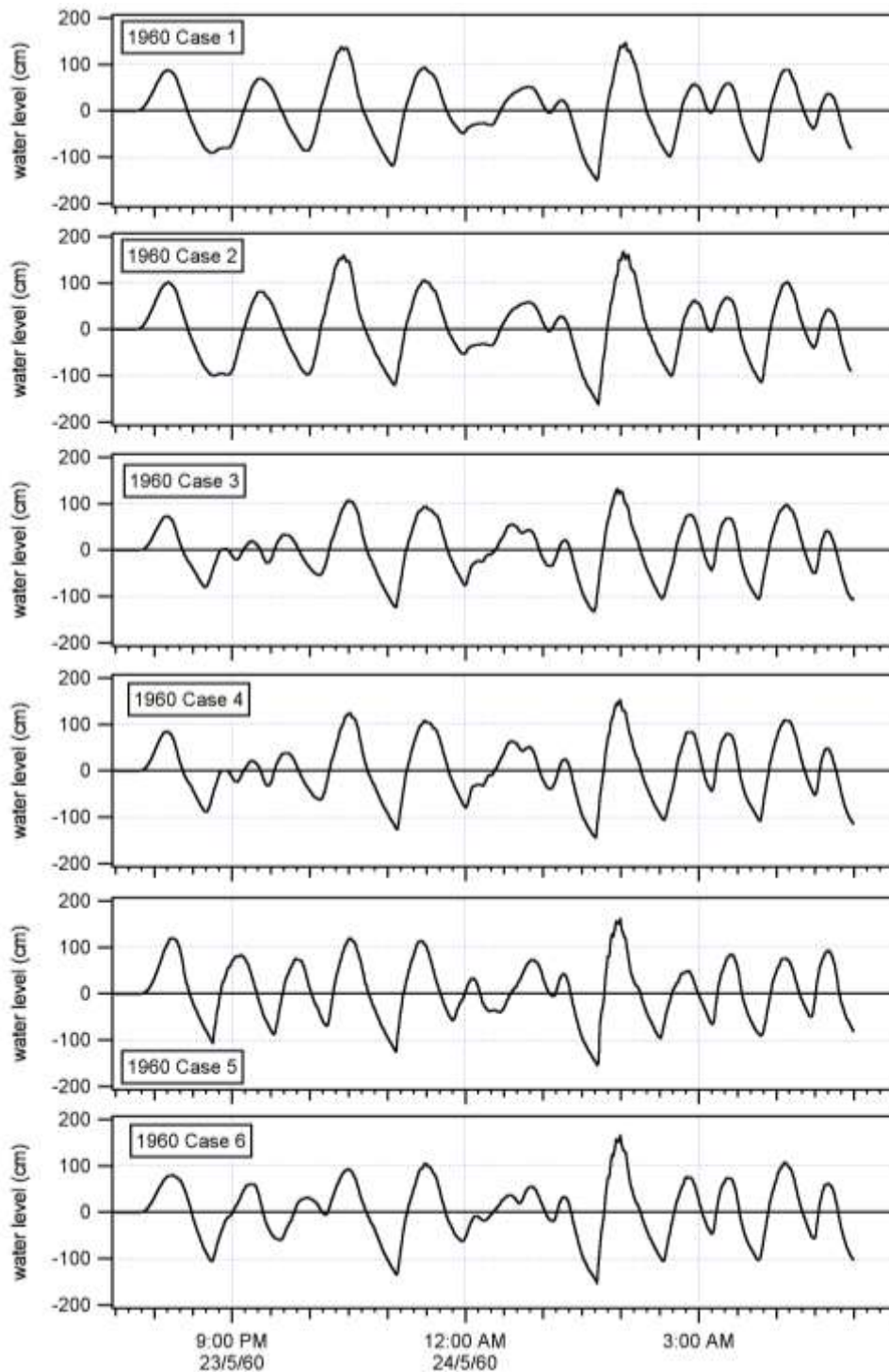


Figure 3.20 Time series of computed water levels at the present location of the Whitianga tide gauge for the six different 1960 Chilean tsunami source models. Model results are from GC 2.

The description of the final location of Mr. Smith's boat and the inundation up Monk Street are consistent with each other. While our model qualitatively matches these descriptions, it does not perform as well in modelling the inundation along the Whitianga water front (Figure 3.21). At the shoreline at the foot of Monk Street, the model predicts a maximum wave amplitude of approximately 2 m, which is of the order necessary to achieve that level of inundation in reality. However, inspection of

the topographic model used by Prasetya et al., (2008) and referenced to Chart Datum (-1.32 m below MSL) shows that the elevations of the land data are in excess of 2 m here, which is not accurate as indicated by the site photograph also shown in Figure 3.22.

It is because of the inaccuracy of the topographic data that our inundation results fall short of reality. We further suggest that the inundation modelling of Prasetya et al. (2008) is over predicting the inundation from the 1960 event. Their results show large scale inundation across the front of Buffalo Beach and reaching an elevation of ~3 m, the occurrence of which is not supported by historical accounts.



Figure 3.21 Modelled inundation overlaid on an aerial image of the Whitianga waterfront. The red line indicates the approximate observed extent of inundation in 1960.



Figure 3.22 The model bathymetry along the Whitianga water front (left) and a photo of the area (right). The photo was taken from a location approximated by the blue oval. The red is the 0 m contour, black contours are in 1 m intervals. Photo was taken between 1 and 2 pm on May 16, 2012 when the tide stage would have been at approximately +1.5 m relative to MLLW (<http://www.tides4fishing.com/nz/coromandel/whitianga>).

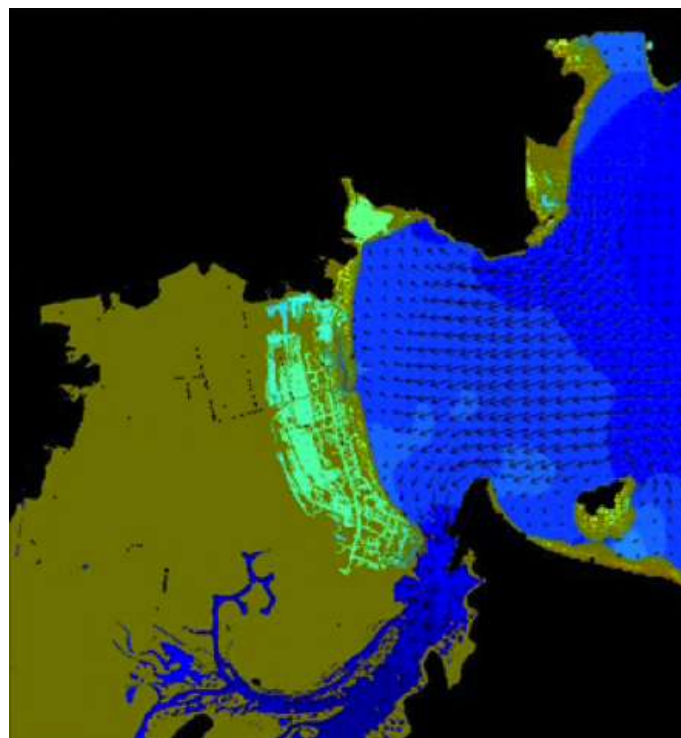


Figure 3.23 Inundation results from Prasetya et al., 2009 for the 1960 Chilean tsunami in Whitianga which significantly overstate the level of inundation along Buffalo beach.

3.5 Model Results for 1960 on the Revised Whitianga Bathymetry

Based on the model results discussed above, the bathymetry and topography used in the simulation was compared to a series of survey control points and a -1.6 m uniform correction was applied prior to re-running the simulations. The adjusted bathymetry grids are shown in Figure 3.24.

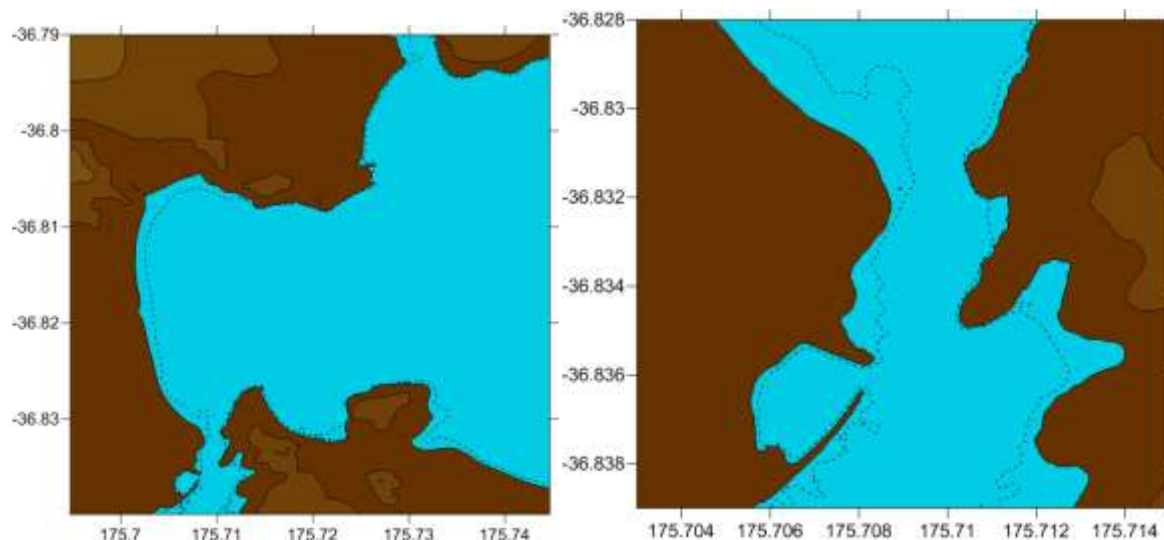


Figure 3.24 Modelling grids adjusted by 1.6 m. The dashed black line is the shoreline (0 m) contour in the original grid.

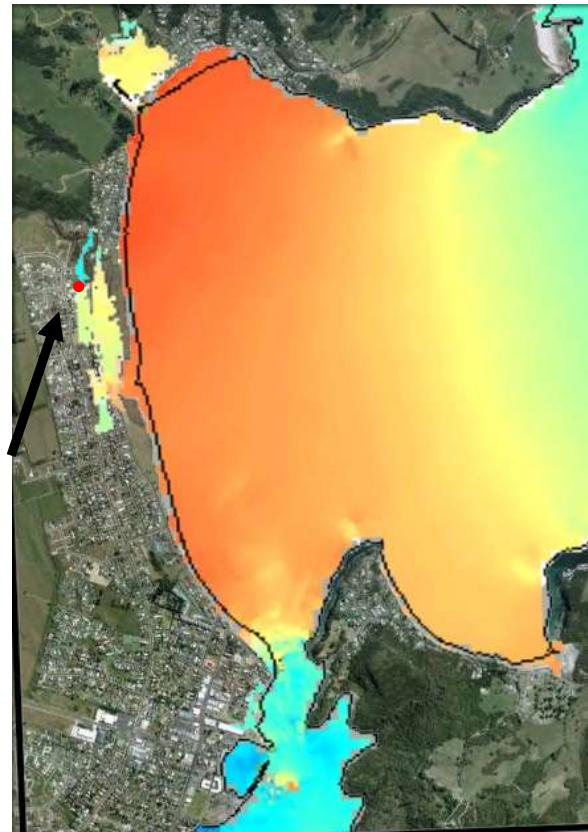
The model was re-run for the 1960 scenarios and selected results are shown in Figure 3.25. These results present a much better fit to the observed inundation effects from the 1960 tsunami. While both cases 3 and 4 replicated the observed inundation along Buffalo Beach, the cases with the higher friction ($n = 0.03$) did not yield sufficient inundation along the town waterfront. Reducing the friction factor on Case 3 to $n = 0.021$, increased the inundation in this area but may still slightly underestimate of the total inundation distance at the waterfront. Case 6 on the other produces more inundation along the waterfront, however it may be overstating the inundation along Buffalo Beach and the beach area just west of the river entrance.

An effort has been made to interview additional eyewitnesses to the 1960 tsunami in Whitianga in an effort to better constrain the extent of inundation caused by that tsunami. Preliminary results of this effort are in general agreement with the model results presented here, however a detailed account of this data is being prepared as a separate report. Based on these results, we contend that the distributed slip source of Fujii and Satake (2012) (used in Cases 3 and 4) yields the best fit to the observed effects during the 1960 Chilean tsunami. This is based on:

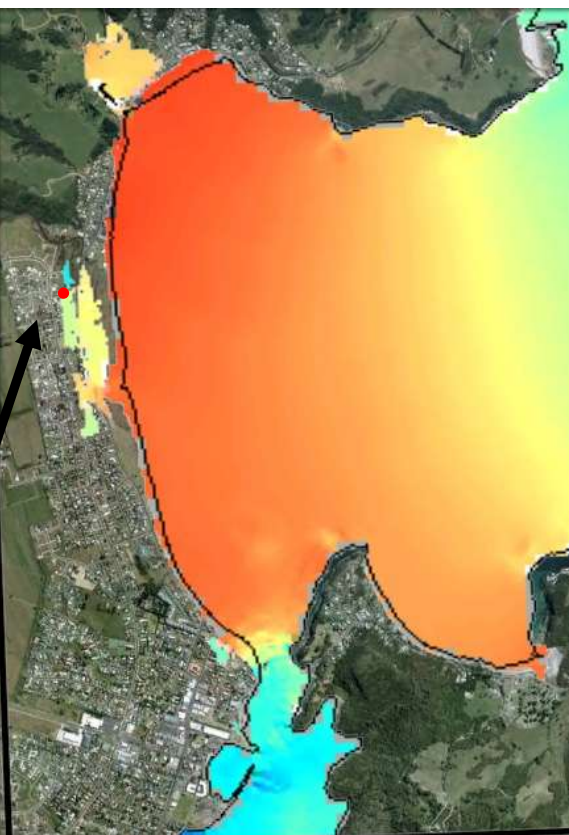
- The high frequency oscillations which occurred around 9:30 pm and are reproduced in the model
- The largest and strongest tsunami surges occurring around 2:30 am which are reproduced in the model, and
- The extent of inundation predicted along Buffalo beach.



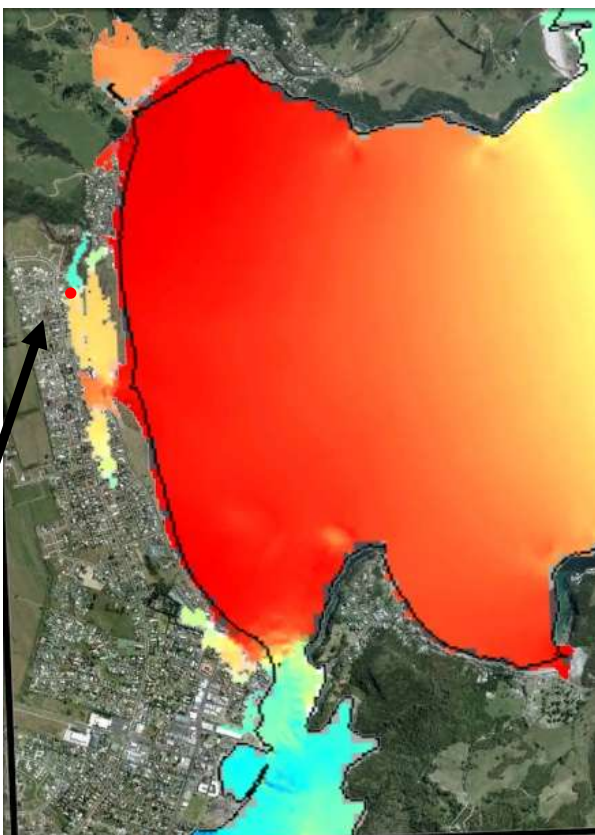
Case 3 (n = 0.03)



Case 3 (n = 0.021)



Case 4 (n = 0.03)



Case 6 (n = 0.03)

Figure 3.25 Modelled inundation in Whitianga from four different models of the 1960 Chilean tsunami. The location of the old Aerodrome hangar is indicated with a red dot.

3.6 Kermadec Trench Source: Effect of Grid Configuration

A sensitivity test for the two grid configurations was also tested with a Kermadec Trench scenario. The model results in Figure 3.26 show the two grids predict nearly identical water motions for the first two wave cycles (up to ~2.5 hours after arrival). A slightly higher positive amplitude is seen for GC 2, while GC 1 produces a slightly larger negative wave on the first significant withdrawal. A slight amount of amplification in later wave cycles is seen in the results (approximately 7 hours after the tsunami arrival). The primary difference between the two signals is the appearance of an additional peak in the GC 2 results occurring after the third overall wave crest. This is followed by one more significant positive surge in both cases, which is then followed by a relatively rapid decay in the wave height. These results suggest that for Kermadec trench type sources, located much closer to New Zealand, a larger hazard exists from the first waves relative to surges later in the wave train. This is in contrast to the far-field cases of Chile 1960 and Japan 2011 where the largest surges occurred many hours after the tsunami arrival.

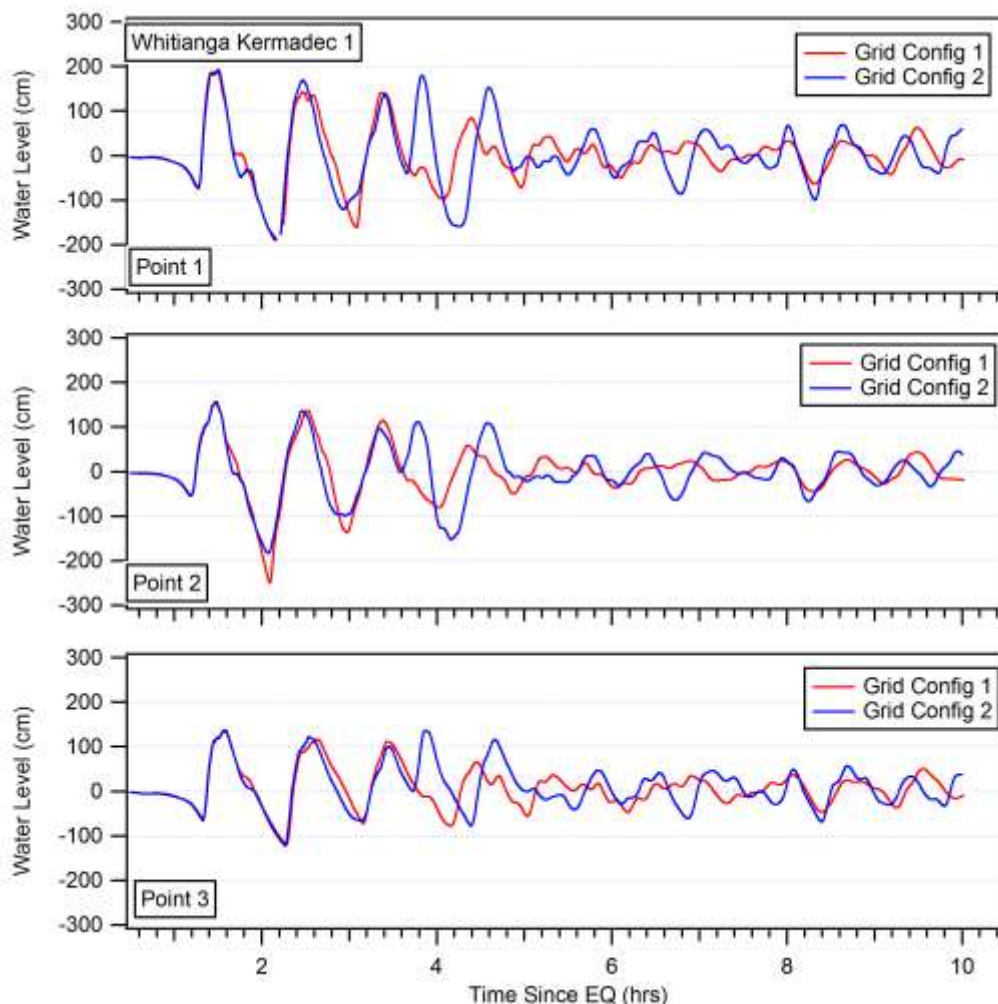


Figure 3.26 Comparison between model results for the two grid configurations at three locations in Whitianga using a Kermadec Trench tsunami source.

3.7 Kermadec Trench Source: Sensitivity to Segment Location:

To assess the sensitivity of the model to the location of the source along the Kermadec Trench, we set up a series of 8 model runs each comprised of two fault segments (as indicated in Figure 3.27). The models were initialised with 10 m of slip on both segments. The maximum and minimum amplitudes of the leading wave height was extracted from a point offshore of Pauanui beach near the entrance to Tairua Harbour (red dot, Figure 3.27).

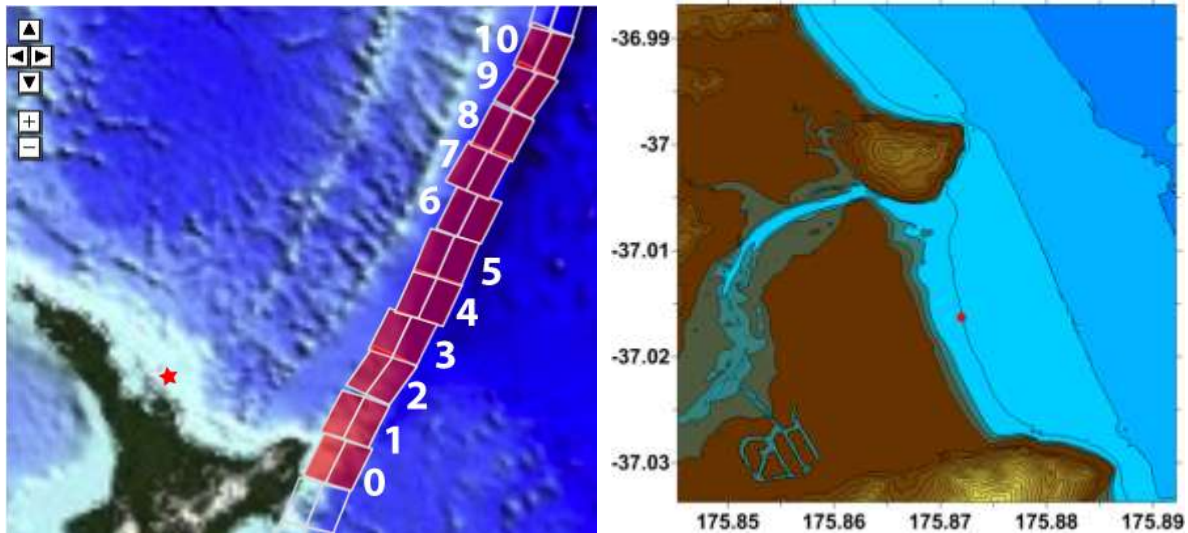


Figure 3.27 (left) The fault segments used in the sensitivity analysis, Each number corresponds to two segments used in each model run. (right) The bathymetry at Pauanui, the red dot corresponds to the location where wave height information is extracted and analysed.

We then plotted the maximum and minimum wave heights as a function of the source segment number (Figure 3.28). This plot shows the sensitivity of the modelled wave height to the source location. We see that the wave height falls away as the source regions moves further north. A significant amount of wave height is also lost when the fault segment is located south of the East Cape. Based on this result we see that segments 1, 2 and 3 contribute the most to the observed wave heights in this area. Computed wave heights are approximately 20% of the slip amount applied to each segment of the fault. Figure 3.29 then shows the computed wave form at the point offshore of Pauanui for each of the segments. The relative arrival times are evident with waves from Segment 1 arriving first. The waves from Segment 0 arrive somewhat later and are not as steep as segments 1 – 5 owing to the blocking effect of the East Cape.

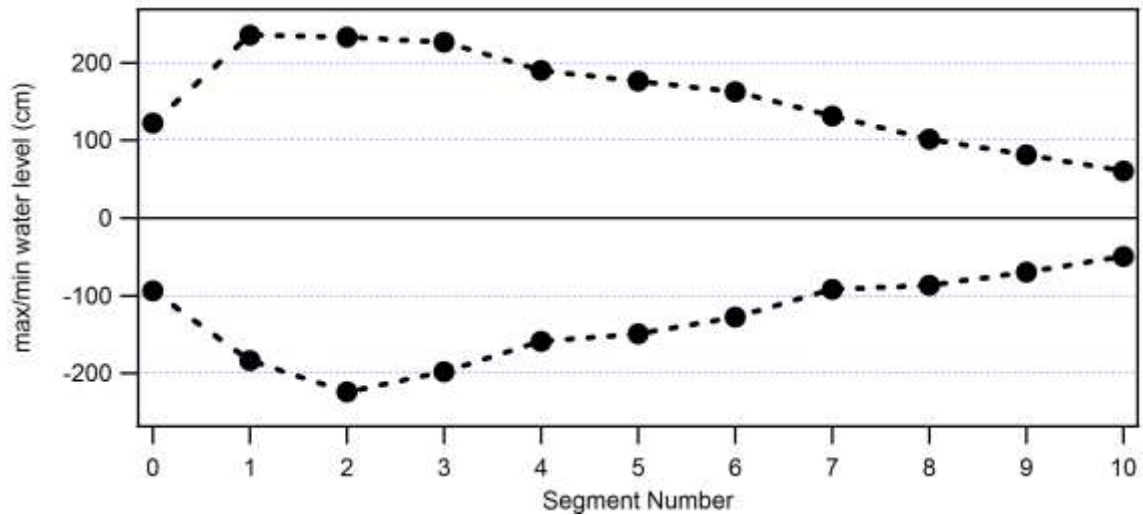


Figure 3.28 Maximum and minimum wave amplitudes recorded offshore of Pauanui Beach as a function of the fault segment.

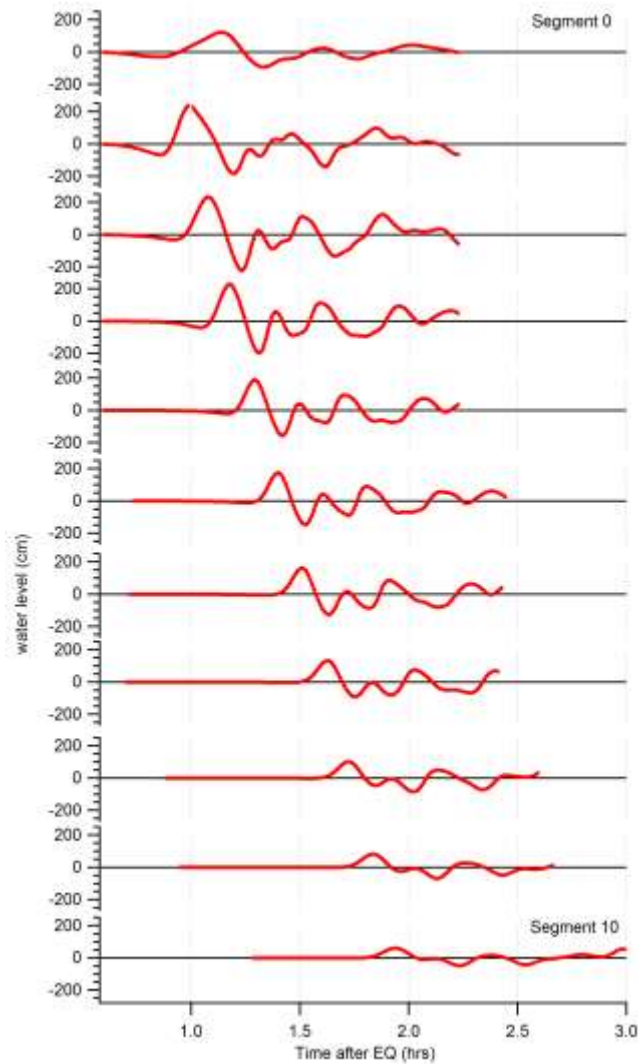


Figure 3.29 Computed wave forms recorded offshore of Pauanui Beach for each of the 11 fault segments.

3.8 Summary of the model Calibration and Sensitivity Analysis

The sensitivity analysis shown above leads to some important observations relative to the grid configurations, the effect of the source model and locations and the effect of the friction parameter. First, we contend that Grid Configuration 2 provides a better fit to the observed water levels at Whitianga caused by the 2011 Japan tsunami. In this example, Grid Configuration 1 does not result in a wave signal that replicates the initial waves well, nor does it capture the larger, late arriving waves. For the Chile 1960 and Kermadec trench scenarios, the results from Grid Configuration 2 result in generally larger wave heights throughout the simulation. Therefore for conservatism and accuracy, we use Grid Configuration 2 as our preferred model.

Looking at the effect of the detailed slip distribution, it was shown that the modelled tsunami water levels are sensitive to the details of this slip distribution. However, for sources of similar magnitude, the slip distribution has only a secondary effect on the overall range in amplitude of the signal. It is nevertheless evident that larger slip amounts in the source region result in larger modelled tsunami heights. Thus it is still important to properly characterise the source model in terms of the slip amount and distribution.

The friction coefficient also has an effect on inundation and wave heights, with lower friction coefficients leading to slightly greater inundation and elevated water levels. Comparison of the water level record at the tide gauge location however shows virtually no difference between the two cases, as we show for the Japan 2011 event. Based on these results we recommend the use of 0.03 as the preferred Manning friction coefficient. The lower friction setting yields some high frequency noise at the peaks and troughs of the waves and seems to produce unrealistically large current speeds. Furthermore, 0.03 is the value used with the MOST model to successfully reproduce the near field inundation characteristics of the 2011 Japan tsunami (Wei et al., 2012) and this value has been adopted as the default for MOST.

In terms of the overall inundation in Whitianga, the model results presented here match with qualitative descriptions of the tsunami effects, timing and water levels. The model however does not match the inundation patterns precisely. We attribute this primarily to discrepancies in the topographic data provided for the study. It is recommended that this topography be revised and the models re-run to confirm this assertion.

Indeed, adjusting the bathymetry to the proper datum results in a much improved model result and shows that the distributed slip scenario of Fujii and Satake (2012) provides the best overall fit to the available observations of the 1960 Chile tsunami in Whitianga.

For the TK Trench scenarios, located much closer to New Zealand, a larger hazard exists from the first waves relative to surges later in the wave train. This is in contrast to both models and observations from large scale far-field tsunamis affecting New Zealand which feature some of the larger wave heights many hours after arrival. In the TK Trench scenarios, the initial period of high wave heights persists for 4-5 hours after tsunami arrival, followed by reduction wave heights over the next few hours.

Following on from this analysis, we illustrated the relative impact of waves from different sources along the TK Trench, The greatest effect on sites in the

Coromandel Peninsula is shown to result from ruptures on the southern segments of the fault that are situated to the north of the East Cape. The induced wave heights fall off as the source region is moved to the north.

3.9 Arrival Times at Whitianga and Tairua-Pauanui from TK Scenarios

Arrival times for tsunami waves generated from the different segments of the Tonga-Kermadec Trench are indicated in Figure 3.29. The plots show that drawdown at Tairua begins less than 1 hour after tsunami generation and the maximum withdrawal occurs between 50 and 90 minutes after tsunami generation. The peak positive surge then arrives 7 to 22 minutes later (see Table 3.1).

Table 3.1 Timing of the maximum withdrawal and maximum positive surge for the 10 unit-source segments shown in Figure 3.27

Segment number	max Drawdown (m)	Time (mins)	max Positive (m)	Time (mins)	Lag (mins)
0	-0.31	51.5	1.23	68.4	17
1	-0.67	51.5	2.36	59.9	8
2	-0.33	55.3	2.33	64.8	10
3	-0.40	62.7	2.27	70.2	7
4	-0.21	70.2	1.9	77.4	7
5	-0.12	75.7	1.76	84.0	8
6	-0.06	80.3	1.63	90.6	10
7	-0.03	86.8	1.32	97.8	11
8	-0.02	92.2	1.01	103.2	11
9	-0.02	99.0	0.81	110.4	11
10	-0.01	94.7	0.61	116.4	22

Table 3.2 Comparison of arrival times in Whitianga and Tairua.

	Whitianga		Tairua		Time Difference (mins)
	Max Drawdown (m)	Time (mins)	Max Drawdown (m)	Time (mins)	
Case 3	-0.89	74.5	-0.80	62.6	12.1
Case 8	-2.18	66.1	-1.95	52.3	13.8

We then look at the arrival times of the eight TK scenario events (Figure 3.30) and compare the arrival time at Whitianga and Tairua for the two end member cases: Case 3 which is the larger of the two northern scenarios and Case 8, which has the slip concentrated on the southern segments (see Figure 2.3 through Figure 2.5). The model results (Table 3. and Figure 3.31) show that the tsunami waves reach Tairua prior to reaching Whitianga by approximately 13 minutes.

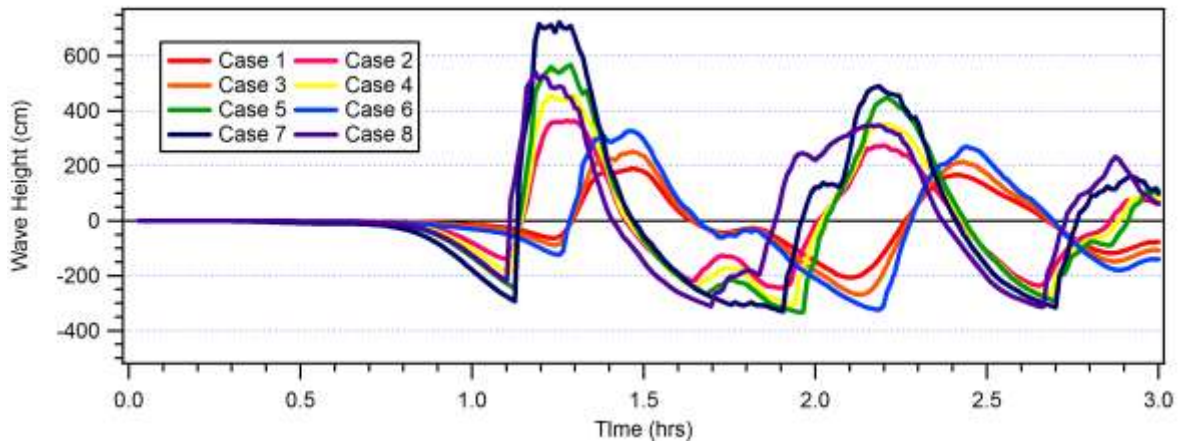


Figure 3.30 The leading wave at Whitianga for the eight TK Scenario events.

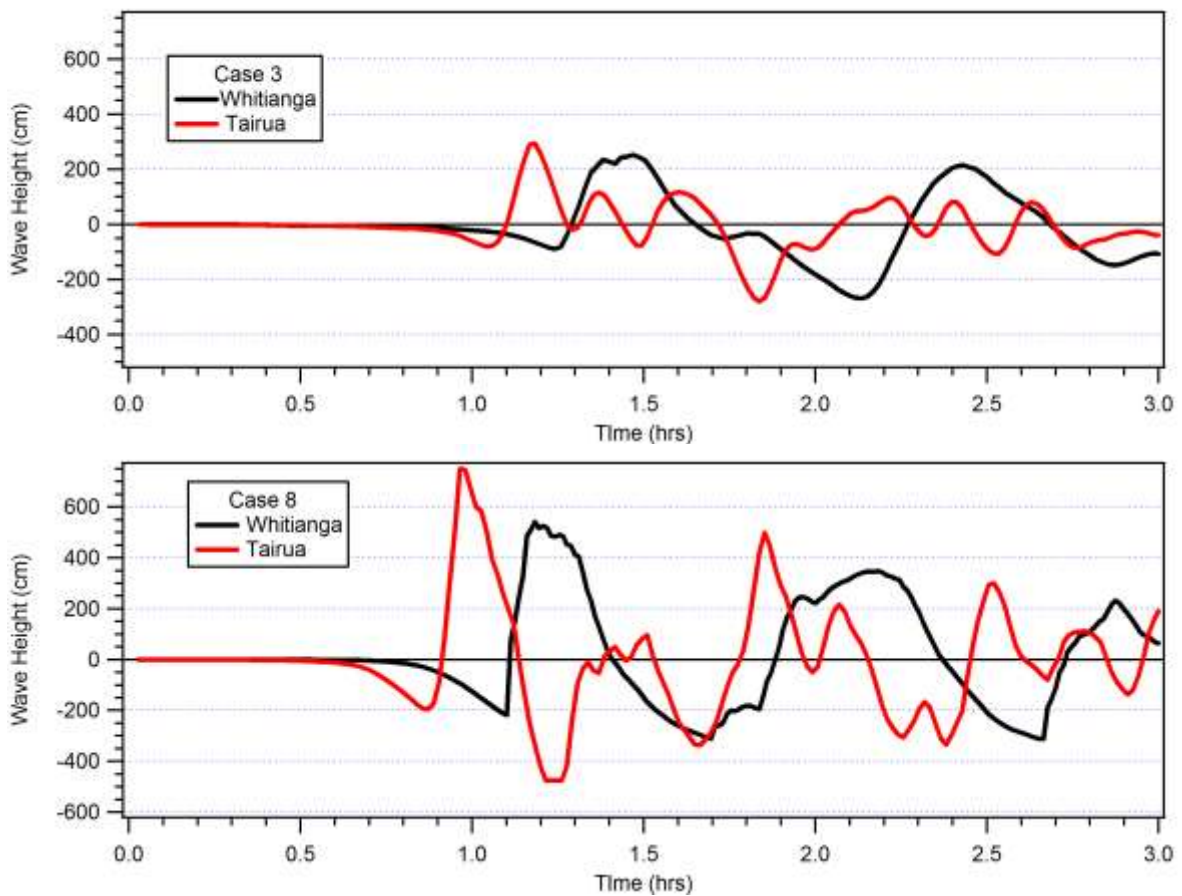


Figure 3.31 Time series of the leading waves at Whitianga and Tairua for Case 3 and Case 8.

4 MODEL RESULTS: TAIRUA PAUANUI

For each of the earthquake scenarios described above, a model simulations were run for the Tairua-Pauanui region, which includes the harbour entrance and the intertidal areas upstream. The model results are depicted on a case by case basis in the figures below.

An important feature of the Pauanui bathymetry is the relatively high topographic relief compared to Whitianga, as shown in Figure 4.1 and Figure 4.2. Additionally, the Tairua data set appears to match reality much more closely than does the Whitianga grid. On the Pauanui side, the populated area are generally at elevations greater than 5 m above MSL. In the area around the Pauanui Waterways development, land levels are lower, but this area lies inside the harbour and is sheltered from direct tsunami impact.

On the Tairua side of the harbour, the main beach area also has higher relief with a dune ridge of more than 5 m elevation present along the beach. Lower topographic elevations exist towards the southern end of the beach. Inside Tairua Harbour, the harbour front of the Tairua township sits at a relatively low elevation, however this area is set back some 500 m across shallow intertidal mudflats which would work to dissipate tsunami energy that enters the harbour.

Tide level at the time of a tsunami is a concern. The grids used for the modelling have all been set to Mean Sea Level (MSL). However, given the low relief of the residential areas fronting Tairua Harbour, we set up a series of simulations for the three southern Kermadec Trench scenarios at a high (+1 m) tide, which is slightly above Mean High Water Spring (MHWS) for Tairua (New Zealand Nautical Almanac, 2010 – 2011).

For the far-field source (presented in Section 4.1), we see that the 1960-type sources do not produce destructive inundation with water levels staying below 1.5 m above the ambient tide level. This water level however would result in small scale inundation properties along the harbour front. For example, along Manaia Road, the berm crest is at approximately +2 m above MSL, and therefore a +1.5 m surge at high tide would overtop and potentially inundate water front properties. Velocities generated by this event are on the order of 2.5 m/s (~5 knots) in the narrow harbour entrance relative to still water. Actual current speeds would be in addition to the tidal currents occurring at that time.

The simulation of the 2011 Japan tsunami produces water elevations on the order of 50 cm along Pauanui Beach near the entrance to the Harbour and some elevated water levels in the canals. Eyewitness accounts from that event report that surges and strong currents were observed in the canals through the day.

A large magnitude earthquake, similar to the 1960 Chile event, along the Peruvian coast is shown to have much stronger effects in Tairua relative to the other two source regions (Japan and southern Chile). This scenario produces water levels in excess of 2 m just outside the harbour entrance and approximately 1 m of water level rise along the beach in front of the Tairua town. Predicted current speeds from this event are somewhat stronger than those predicted for the 1960 Chile cases.

The situation changes for the Kermadec trench scenarios however. These simulations suggest that the Kermadec trench sources would produce much higher water levels and stronger currents than any of the far field sources. This would be expected given the proximity of these sources to the east coast of New Zealand. The tide stage also has a strong effect on the resulting inundation, particularly inside of Tairua Harbour with higher tide elevations resulting in greater inundation. Furthermore, a tsunami of this nature occurring at high tide could possibly inundate areas at the south end of Tairua Beach and at the south end of Pauanui Beach. Both location feature a small stream in this area that would serve to funnel the incoming surge on to the dry land.

The most severe effects are seen from the Kermadec Trench Case 5. This scenario represents an extreme, relatively near field event and the biggest potential hazard for the study site. The model results show this event causing significant inundation at the southern end of both Tairua and Pauanui Beaches with the tsunami surge breaching the dune ridge and flowing in to the harbour on the other side. This effect is more pronounced on the high tide case.



Figure 4.1 The Tairua topography DEM over aerial imagery. The photo shown in below was taken from the location indicated by the blue dot with a view to the southeast. The thicker black line is the 0 m contour while the red line is the +1 m elevation. Thinner black contours are at 5 m intervals.

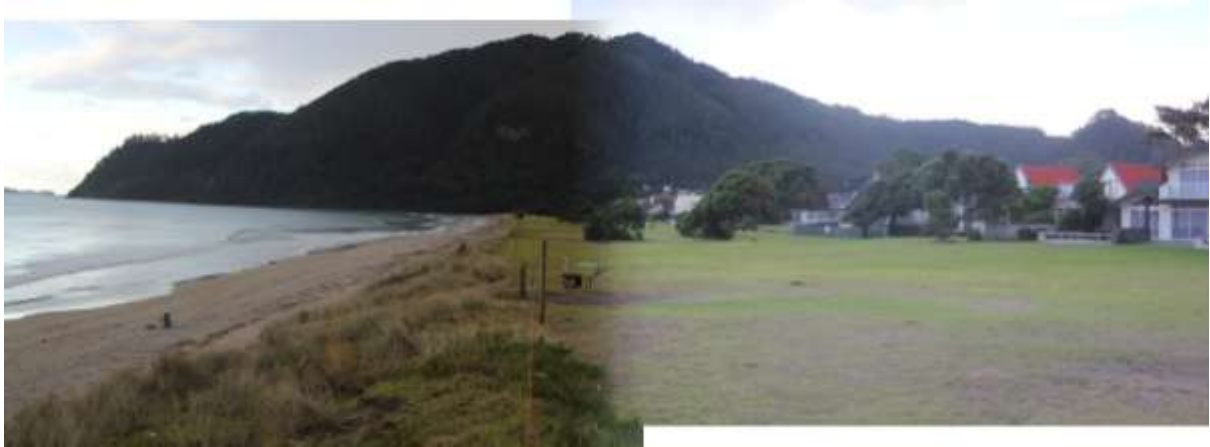


Figure 4.2 View along Pauanui Beach, the dune crest is on the order of 5 meters above sea level and there is an ample set back to the first house.



Figure 4.3 The beach at Tairua showing the relatively high dune ridge and large set back along the northern end of the beach. On the southern end (in the foreground) the topographic relief is lower and the buildings are located closer to the sea.

4.1 Far Field Sources

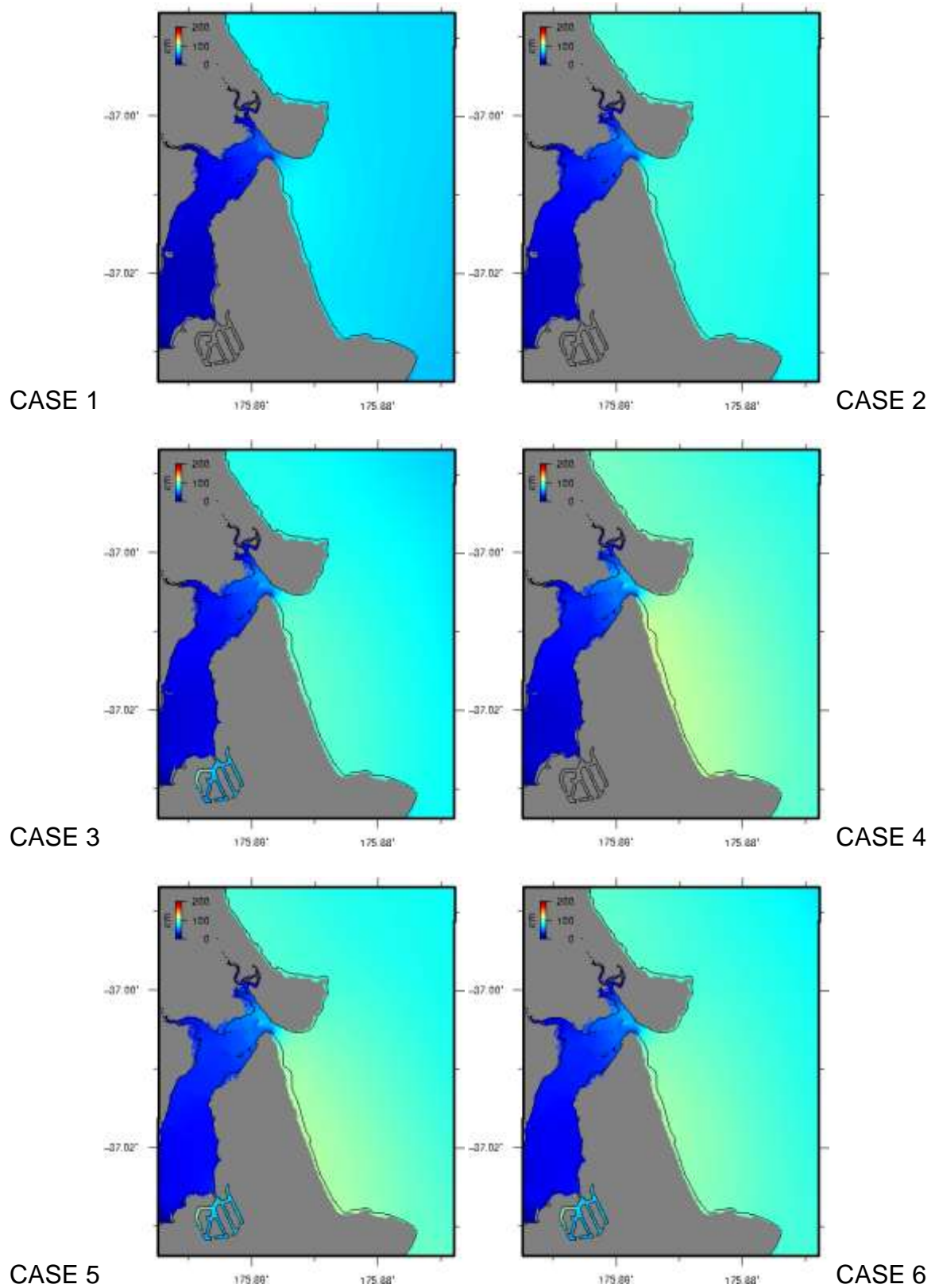


Figure 4.4 Maximum computed water level in Tairua at mid-tide for Cases 1 – 6 of the 1960 Chile tsunami.

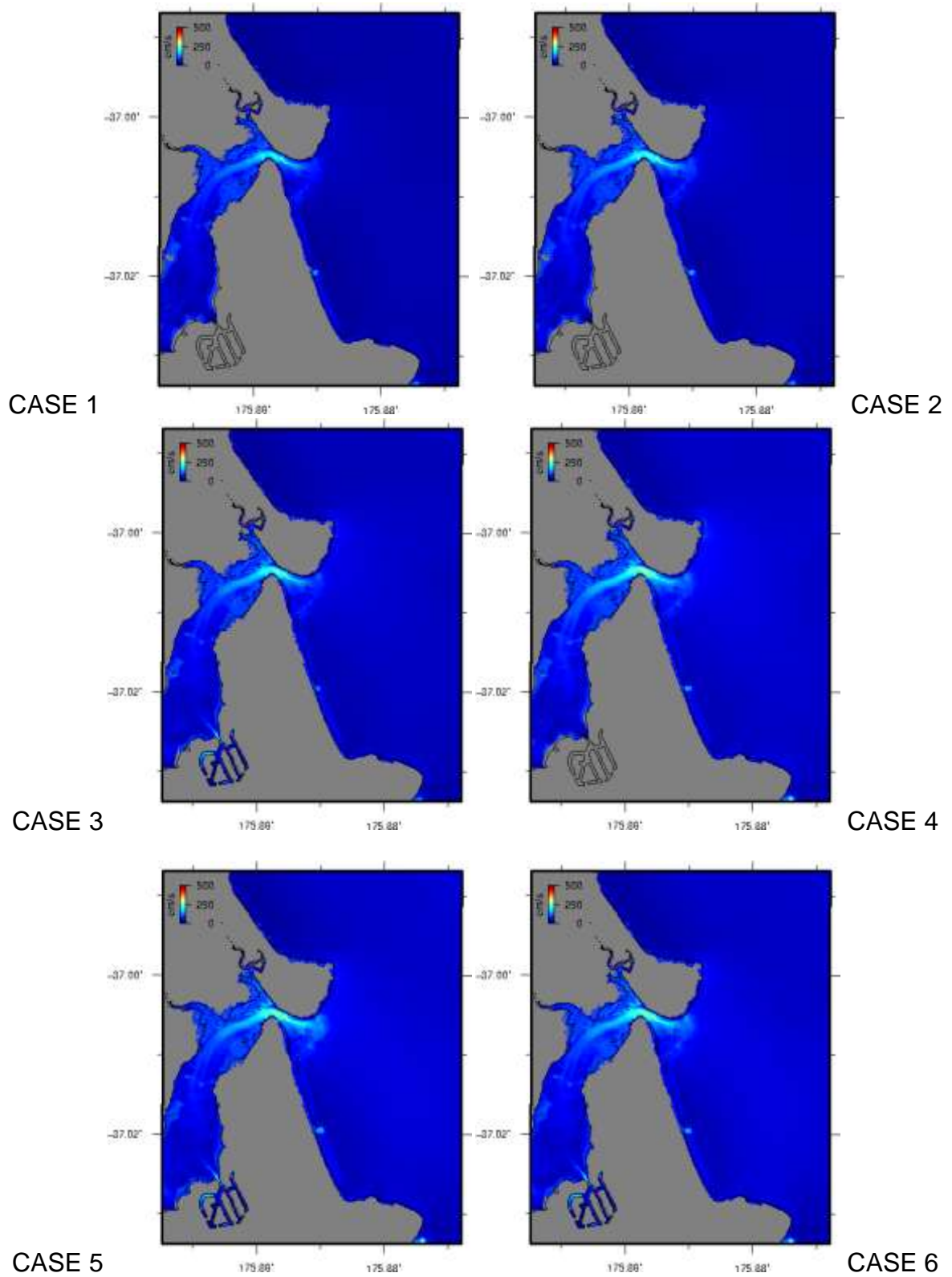


Figure 4.5 Maximum computed current speed in Tairua at mid-tide for Cases 1 – 6 of the 1960 Chile tsunami.

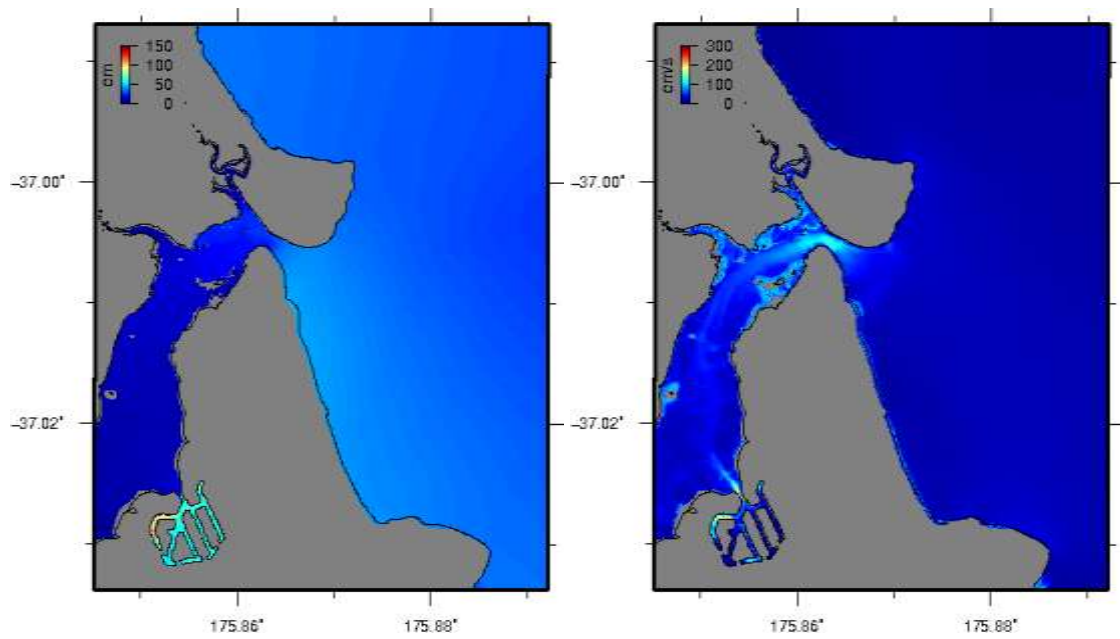


Figure 4.6 Simulation of the 2011 Japan tsunami in Tairua. Water level (left) and current speed (right).

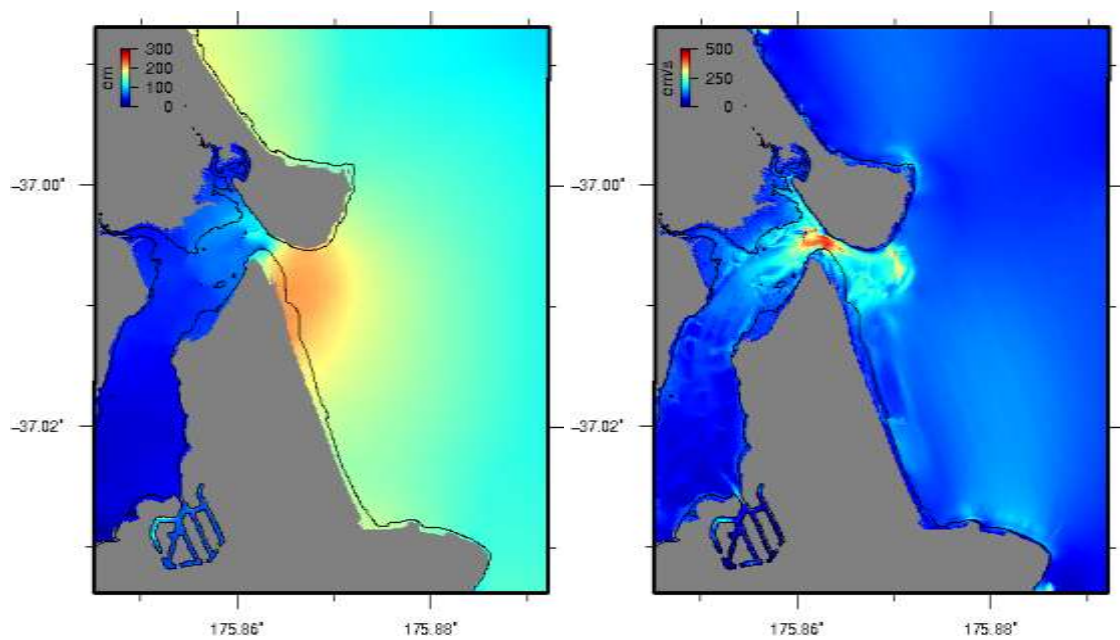


Figure 4.7 Simulation of a 1960 Chile-type source in Peru affecting Tairua at mid-tide. Water level (left) and current speed (right).

4.2 Kermadec Trench Sources

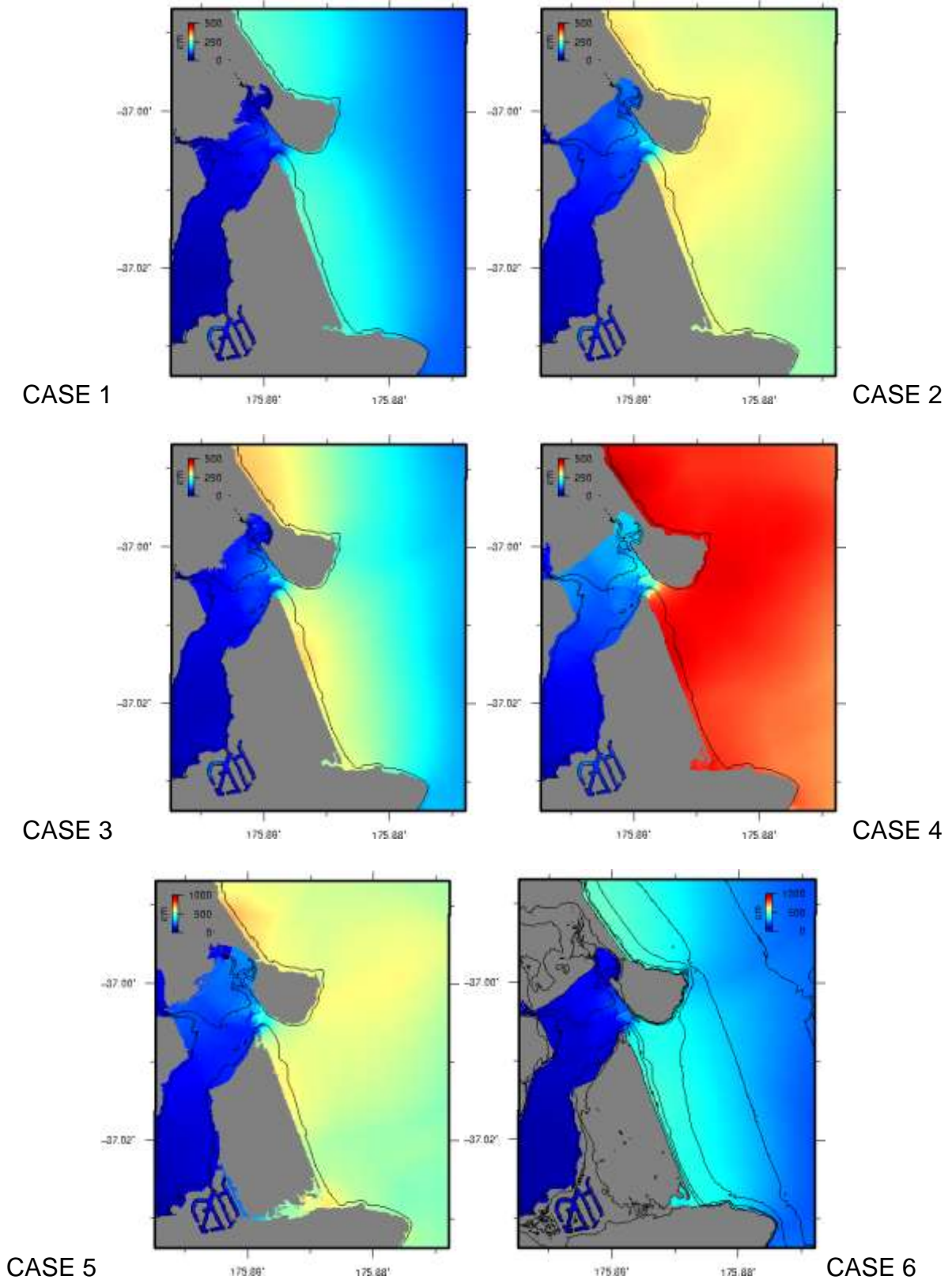


Figure 4.8 Maximum computed water level for the Kermadec Trench Cases 1-5 in Tairua at MSL. Note change in colour scale on Case 5 and Case 6.

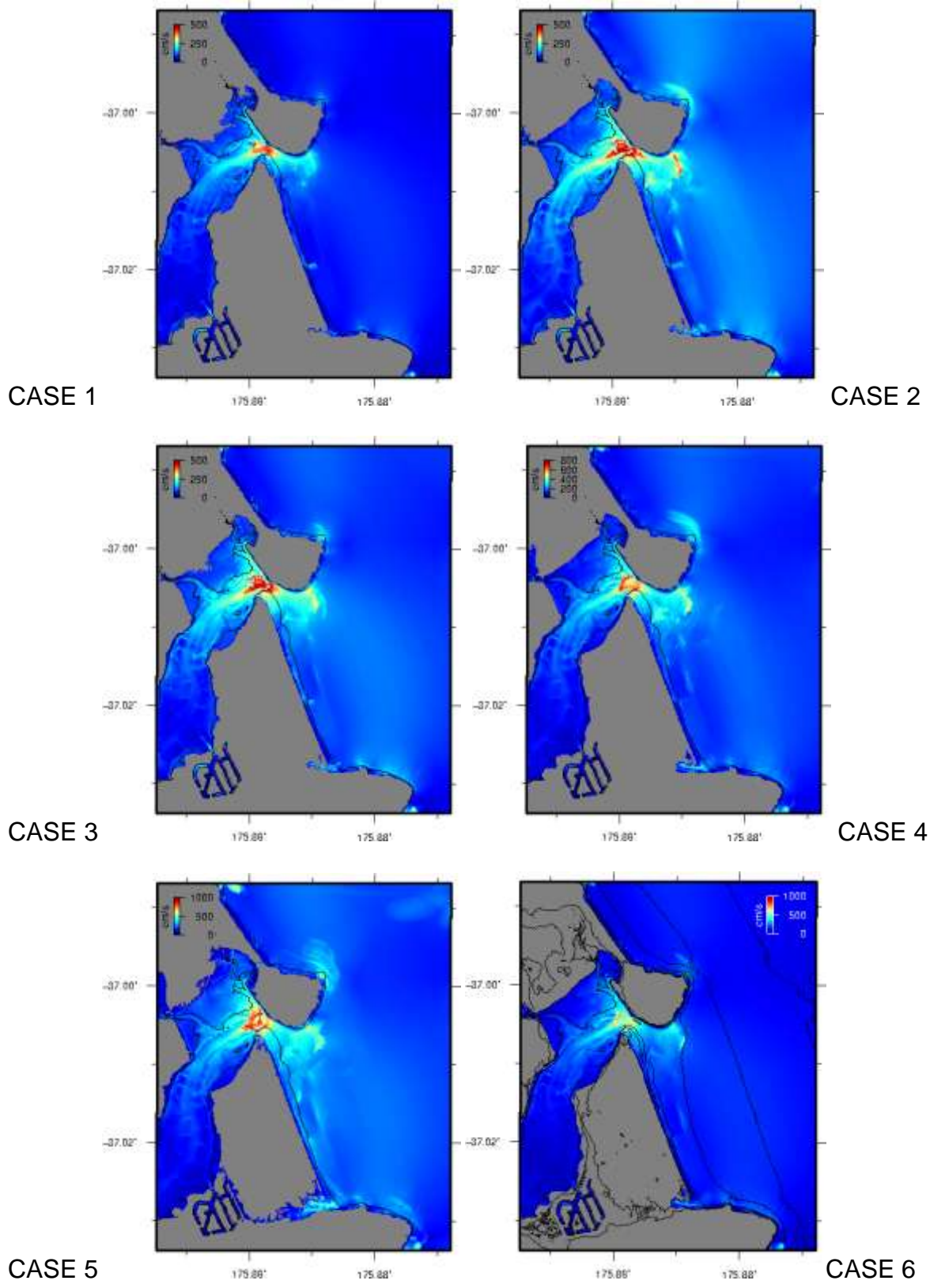


Figure 4.9 Maximum computed current speeds for the Kermadec Trench Cases 1-6 in Tairua at MSL. Note change in colour scale on Case 5 and Case 6.

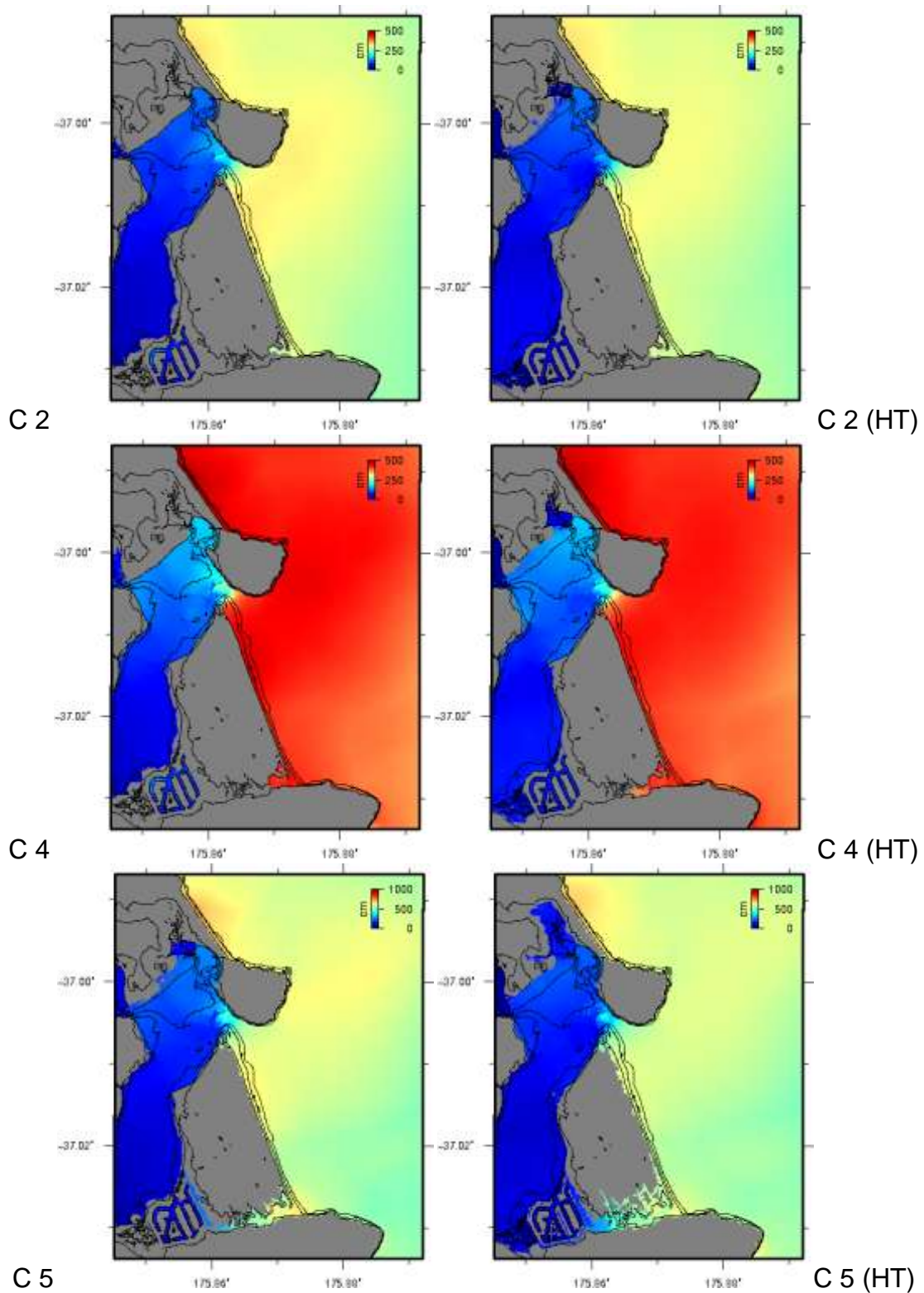


Figure 4.10 Comparison between mid tide (left) and high tide (+1 m, right) modelled inundation at Tairua – Pauanui for the three southern Kermadec Trench scenarios. Contours are the 0,1 and 5 m contours relative to MSL.

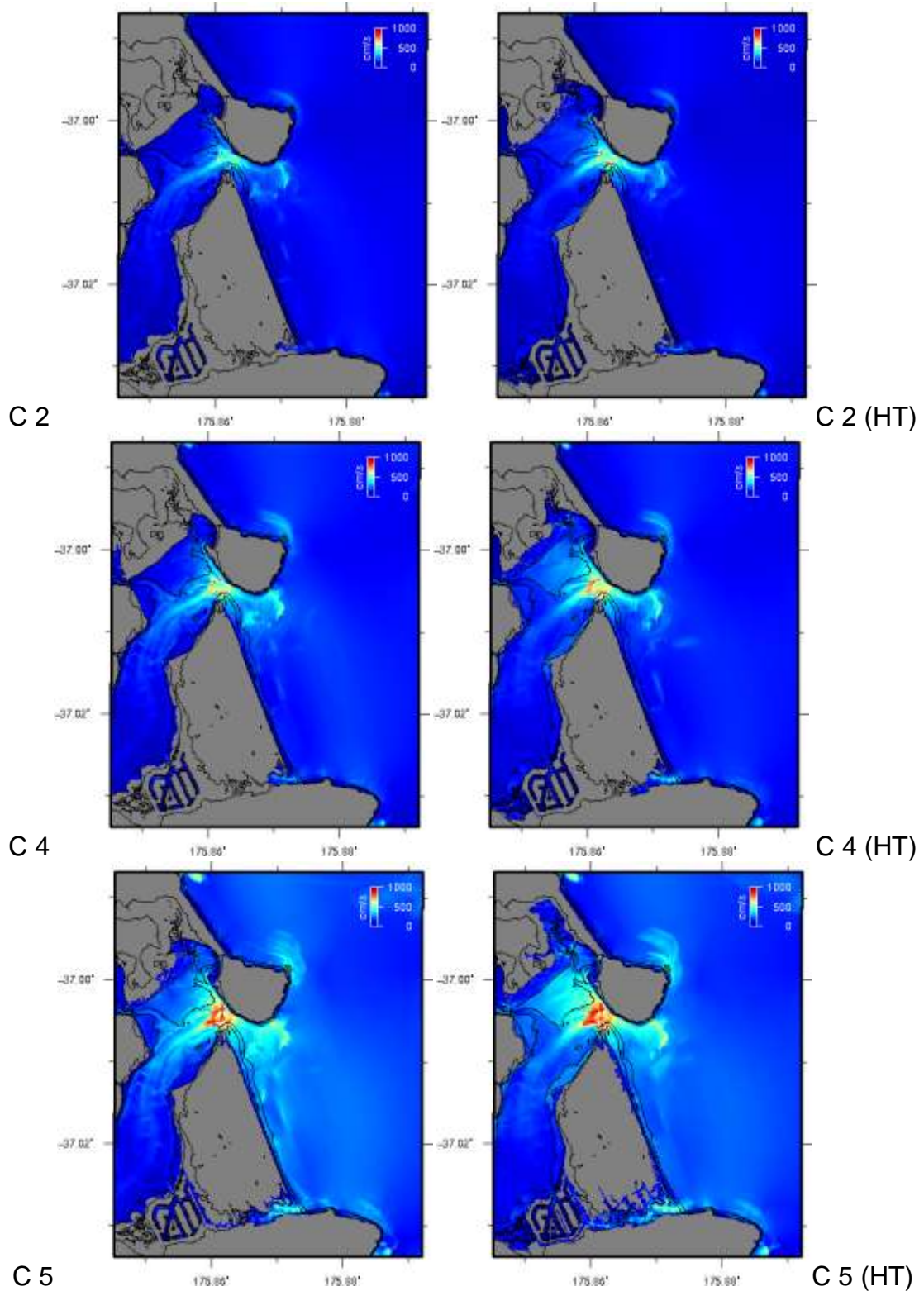


Figure 4.11 Comparison between mid tide (left) and high tide (+1 m, right) modelled current speeds at Tairua – Pauanui for the three southern Kermadec Trench scenarios. Contours are the 0,1 and 5 m contours relative to MSL.

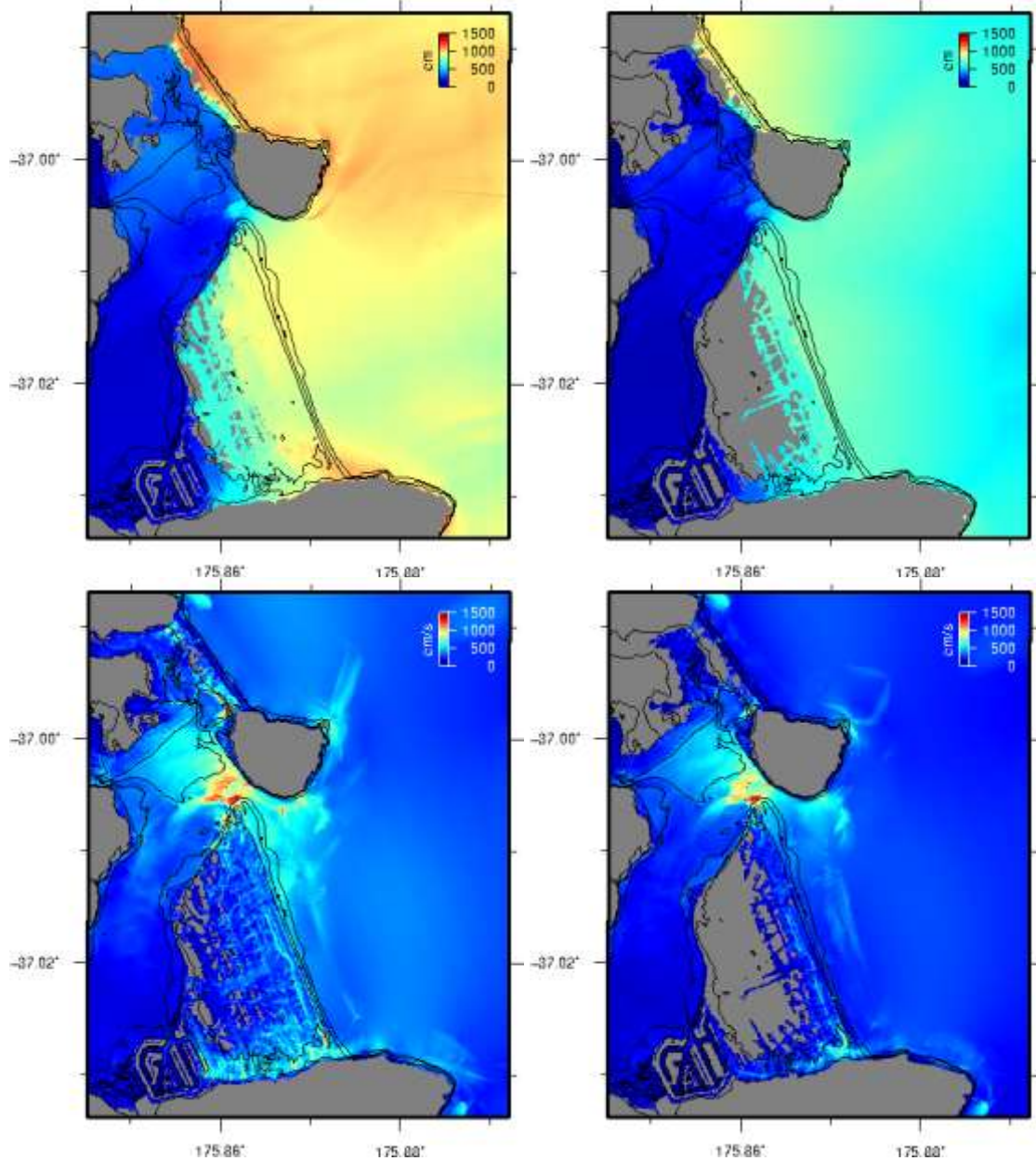


Figure 4.12 Maximum computed water levels and current speeds in Tairua from Case 7 (left) and case 8 (right) at high tide.

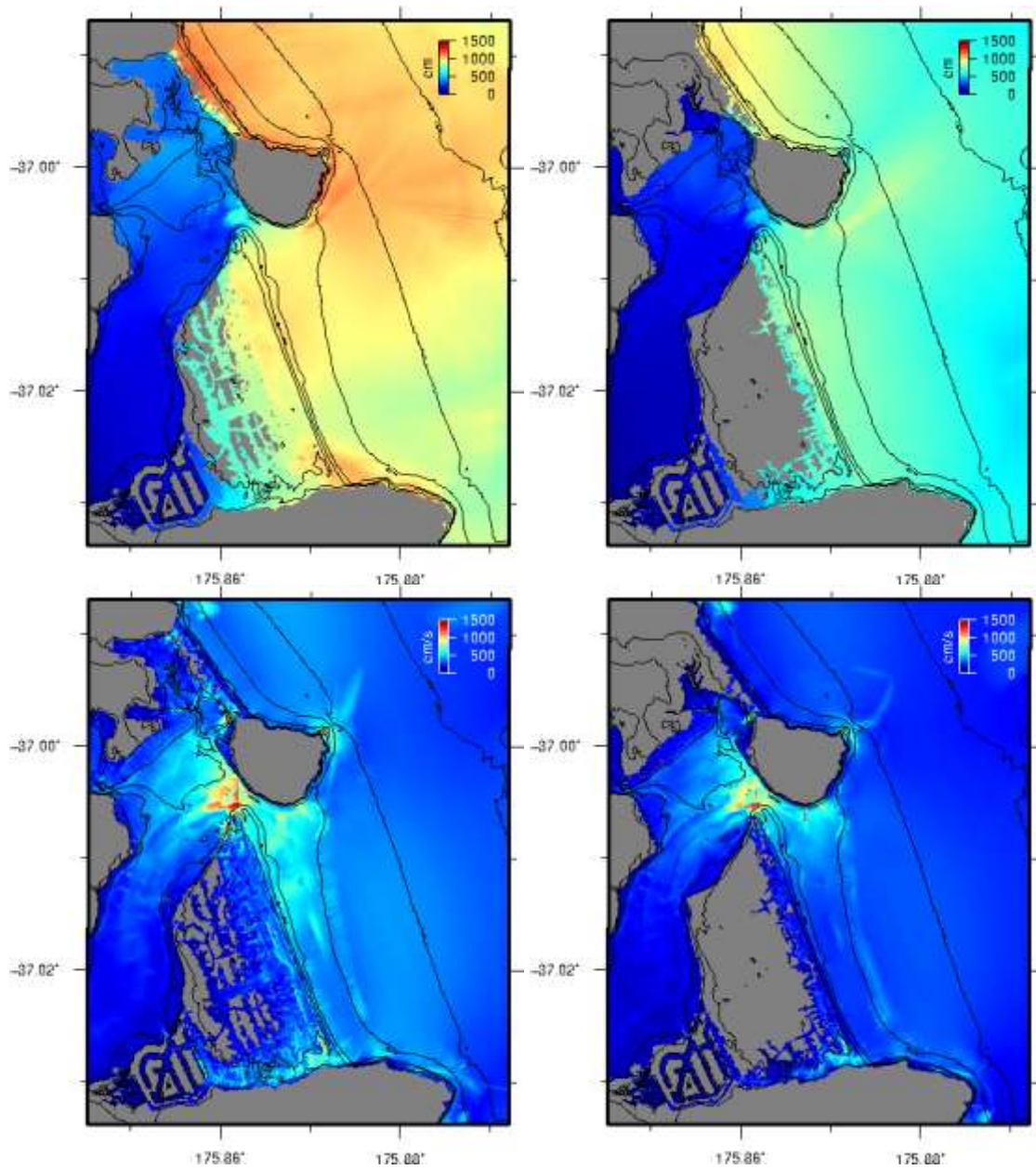


Figure 4.13 Maximum computed water levels and current speeds in Tairua from Case 7 (left) and case 8 (right) at MSL.

5 MODEL RESULTS: WHITIANGA

5.1 Far Field Sources

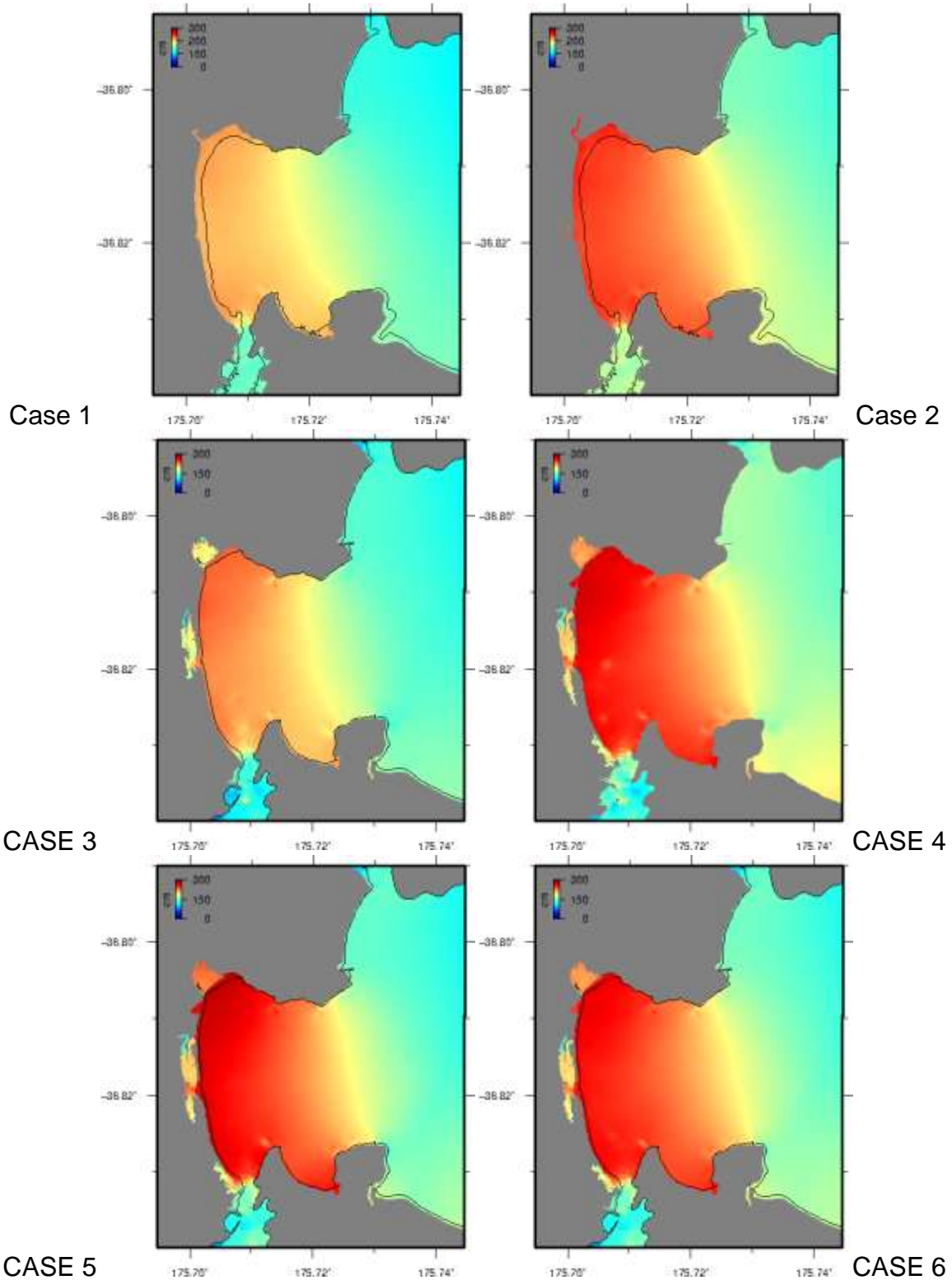


Figure 5.1 Maximum water level (cm), Whitianga, 1960 cases. Note these results are for Grid Configuration 2. Cases 3-6 are computed on the

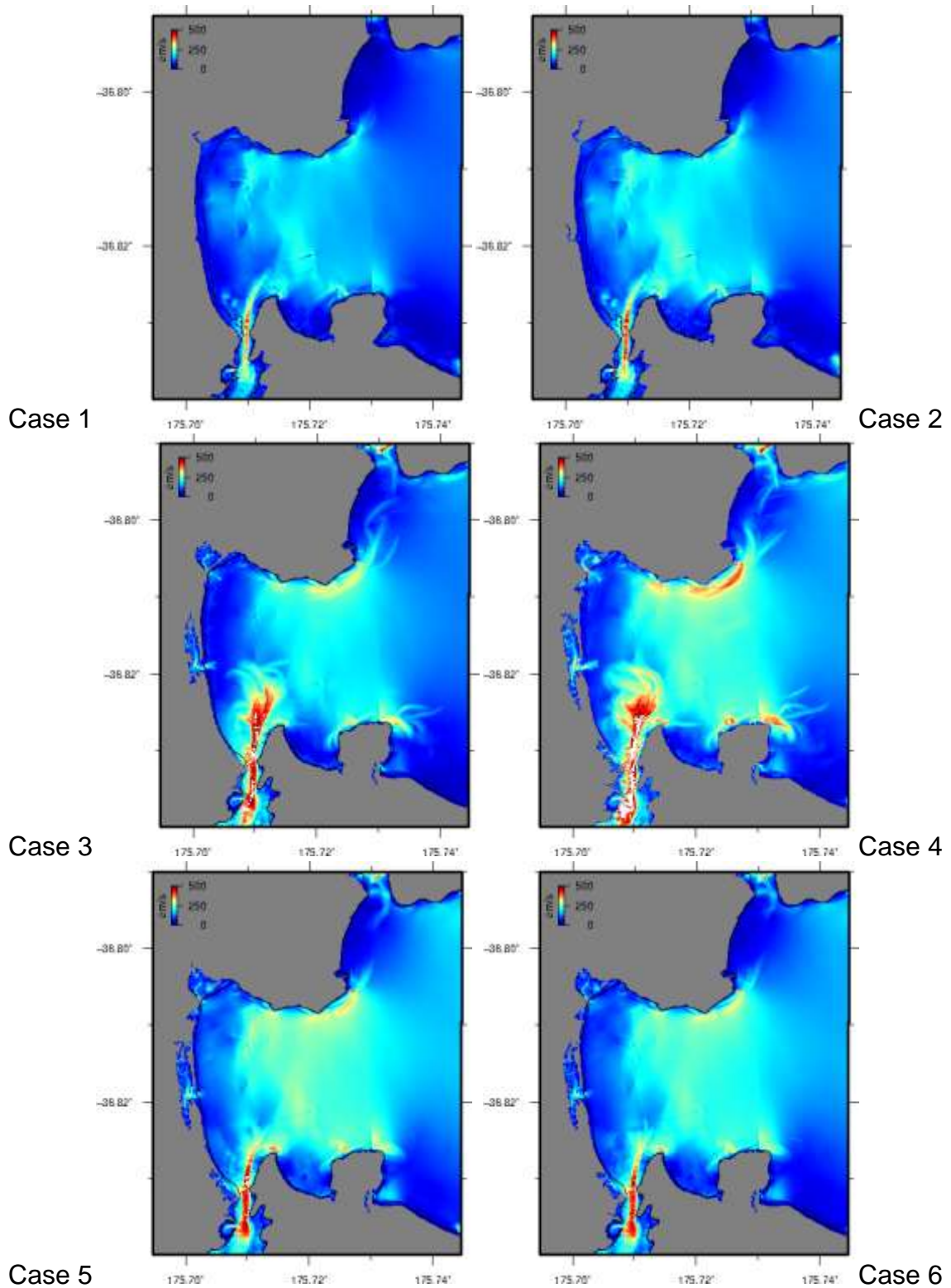


Figure 5.2 Maximum current speed, (cm/sec) Whitianga, 1960 cases. Note these results are for Grid Configuration 2.

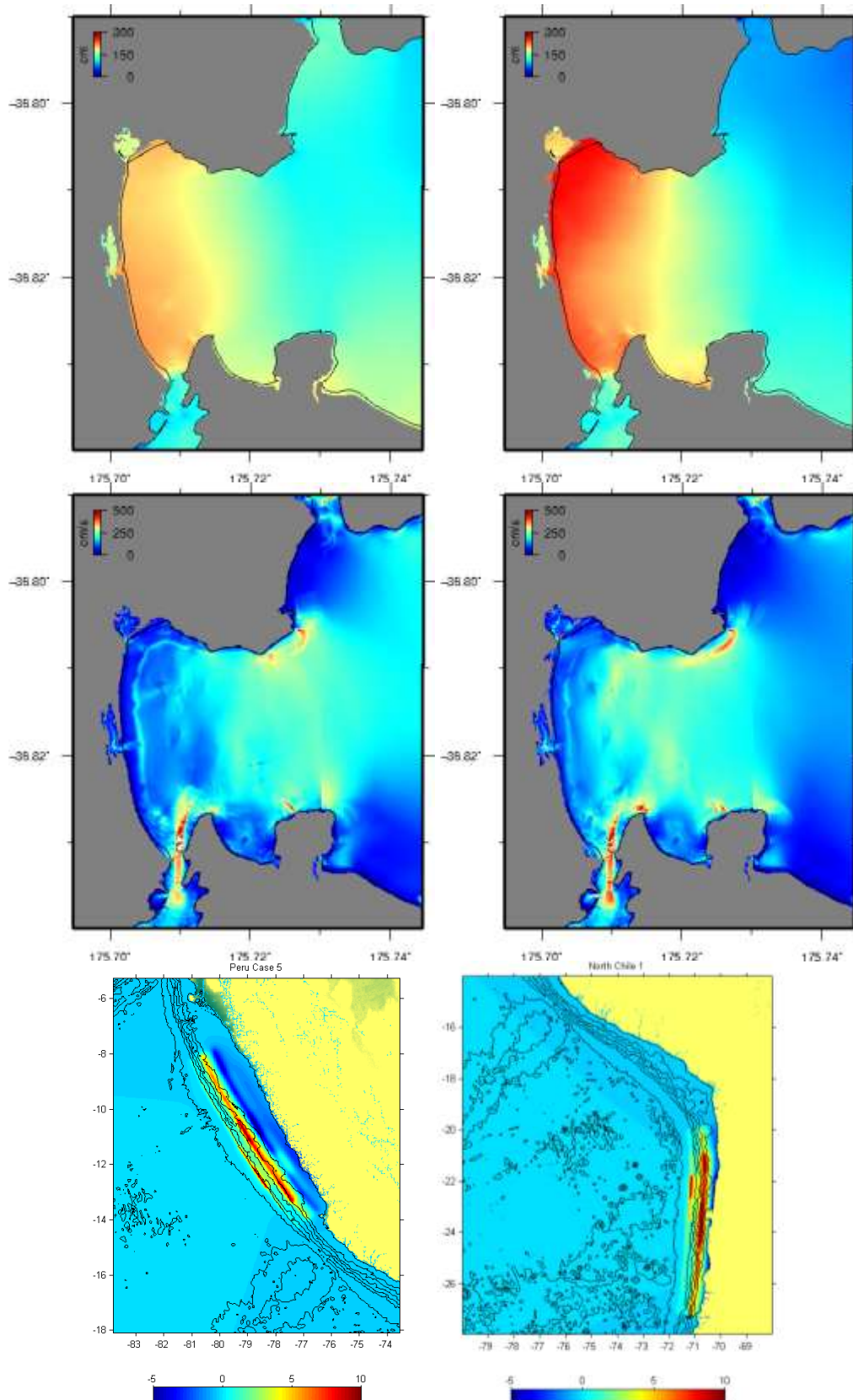


Figure 5.3 Maximum water level and current speeds in Mercury Bay predicted by the model for a hypothetical 1960-type source located in Peru (left) and northern Chile (right).

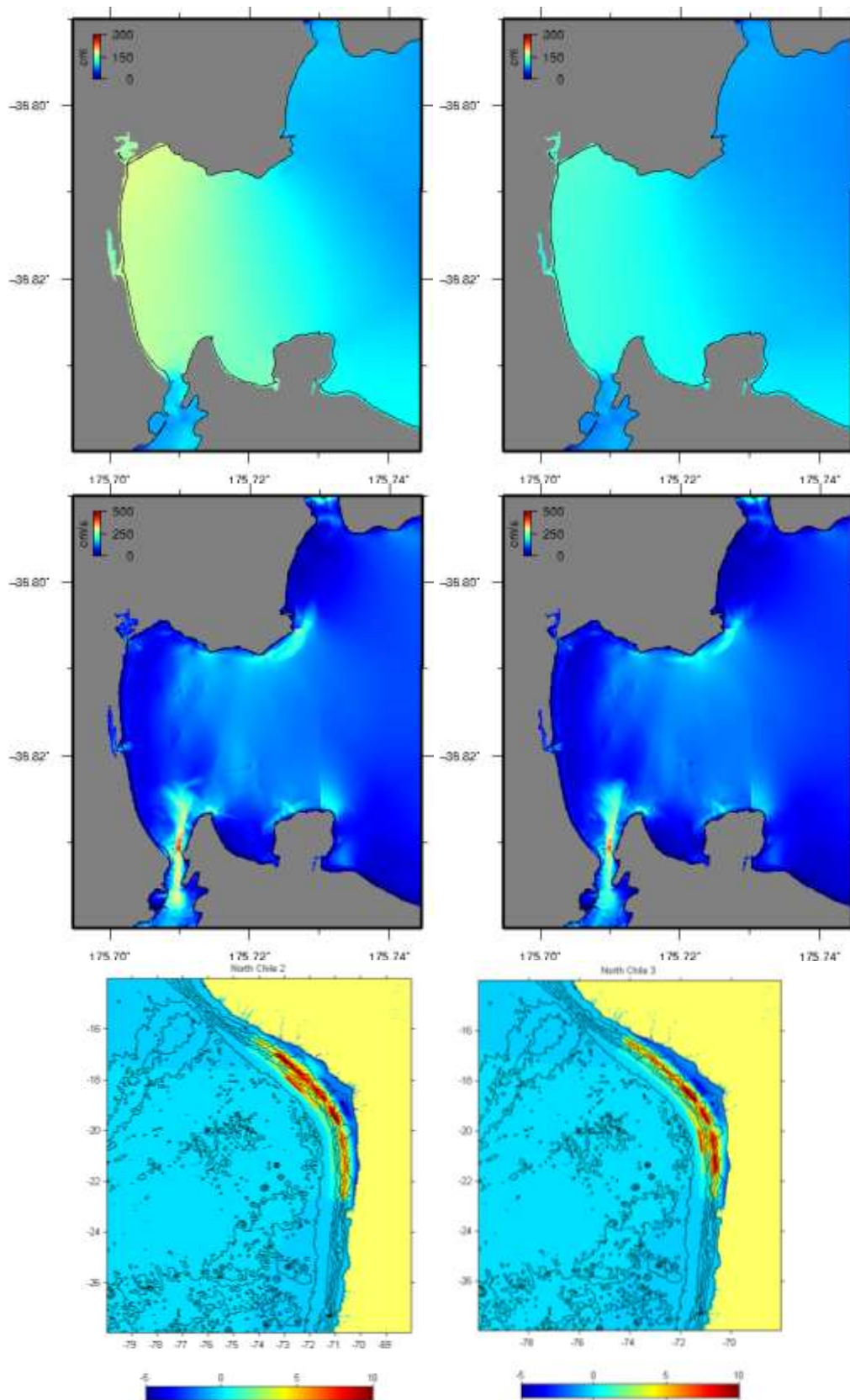


Figure 5.4 Maximum water level and current speeds in Mercury Bay predicted by the model for a hypothetical 1960-type source located in the Peru/Chile border region.

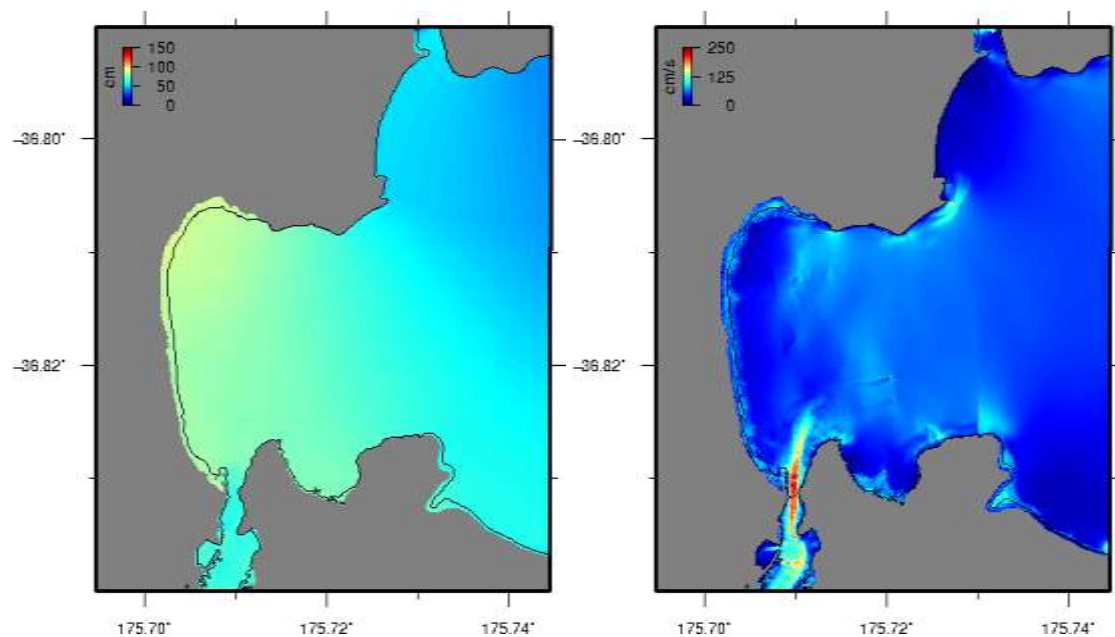


Figure 5.5 Maximum water level and current speed in Whitianga predicted by the model for the 2011 Japan (Tohoku-oki) tsunami.

5.2 Kermadec Trench Scenarios

The following figures show the maximum computed water levels and current speeds in Whitianga resulting from the hypothetical earthquake scenarios along the Tonga-Kermadec subduction zone (see Section 2.2). For each pair of scenarios (1,2), (3,4), and (5,6), the only difference between the initial condition is the position of the southern extent of the rupture zone. These results further illustrate the findings depicted in Section 3.7, that the tsunami effects along the Coromandel Peninsula are highly dependant on the source location, The further south the rupture zone, the stronger the tsunami effects. In Case 1 for example, the inundation extents from a near field M 8.9 earthquake are less than what was experienced during the 1960 Chilean tsunami, however, moving that same source just 200 km to the south results in significant inundation across Whitianga. This pattern is repeated for Cases 3 and 4 and Case 5 and 6, however with ore significant inundation due to the larger earthquake magnitude used in each set.

Case 7 and 8 are presented to show the effect of very large earthquakes occurring on the Kermadec trench. While each of these events is extreme, these scenarios are based on actual subduction zone events. Case 7 is analogous to the 1960 Chilean earthquake occurring along the TK trench and Case 8 is identical to the source responsible for the 2011 Japan tsunami. The projected inundation in Whitianga caused by either of these sources would result in nothing short of complete devastation of the Whitianga township.

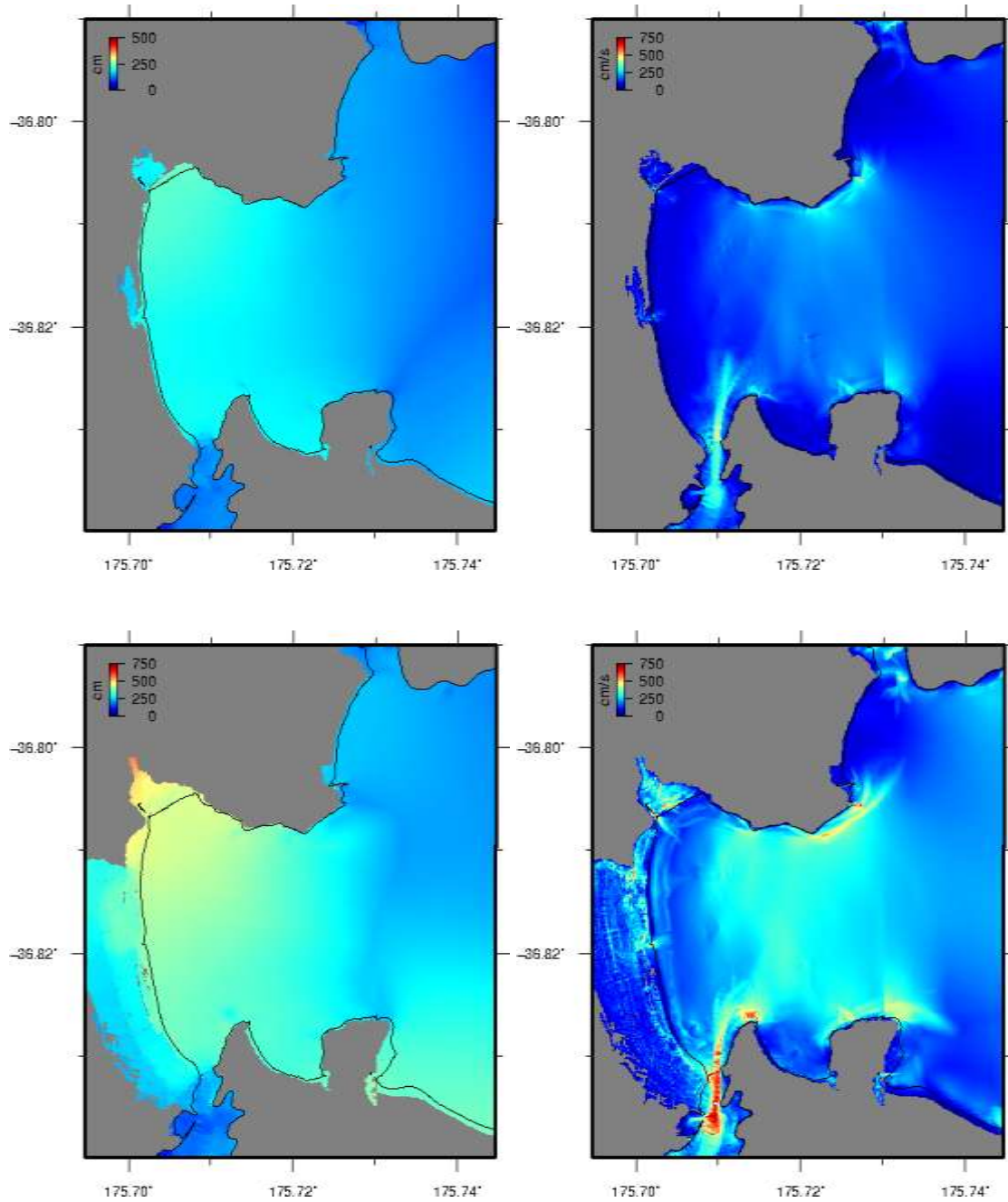


Figure 5.6 Kermadec Trench scenarios in Whitianga. Case 1 (top) and Case 2 (bottom). For each case water level is on the left and current speed is on the right.

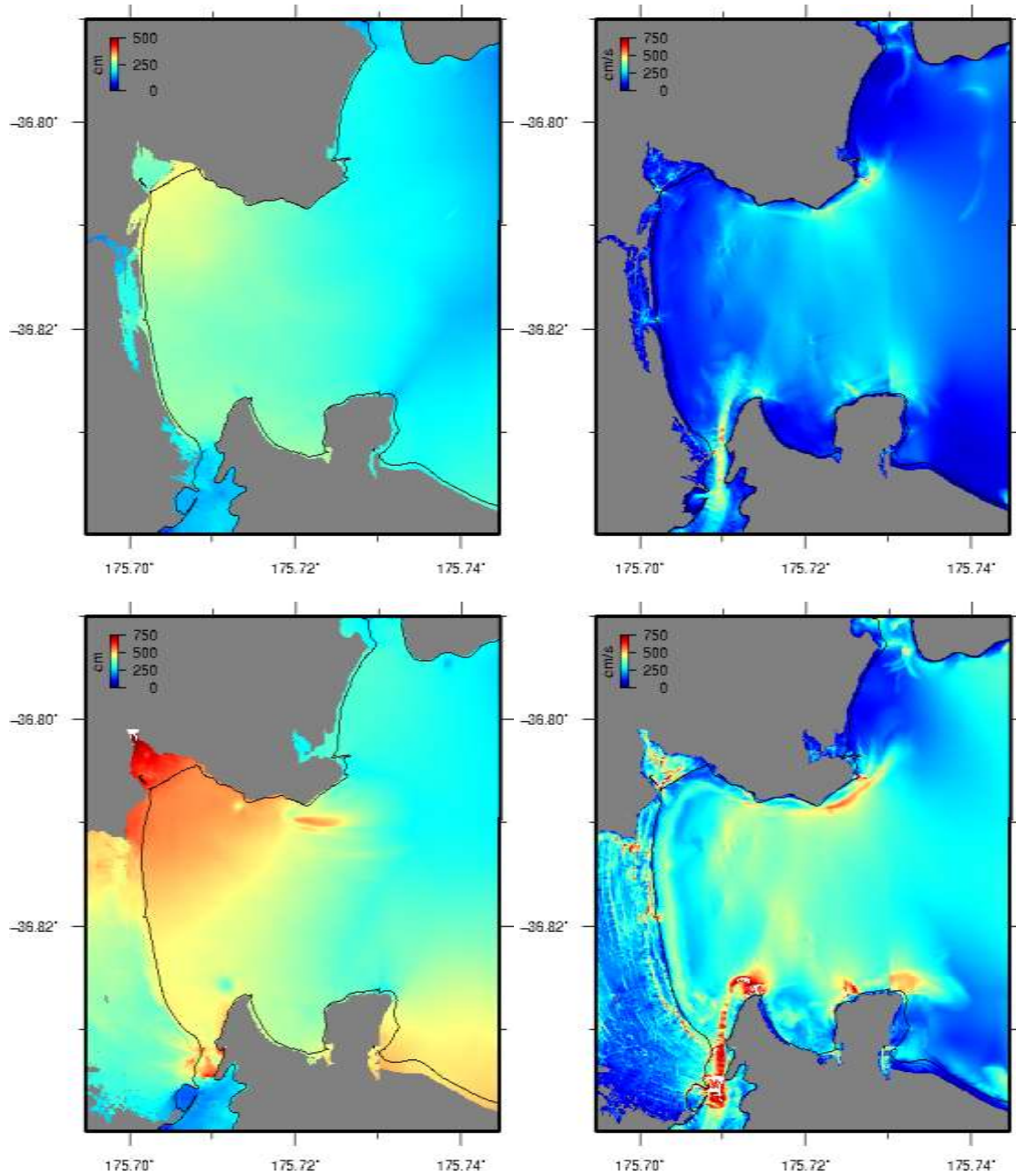


Figure 5.7 Kermadec Trench scenarios in Whitianga. Case 3 (top) and Case 4 (bottom). For each case water level is on the left and current speed is on the right.

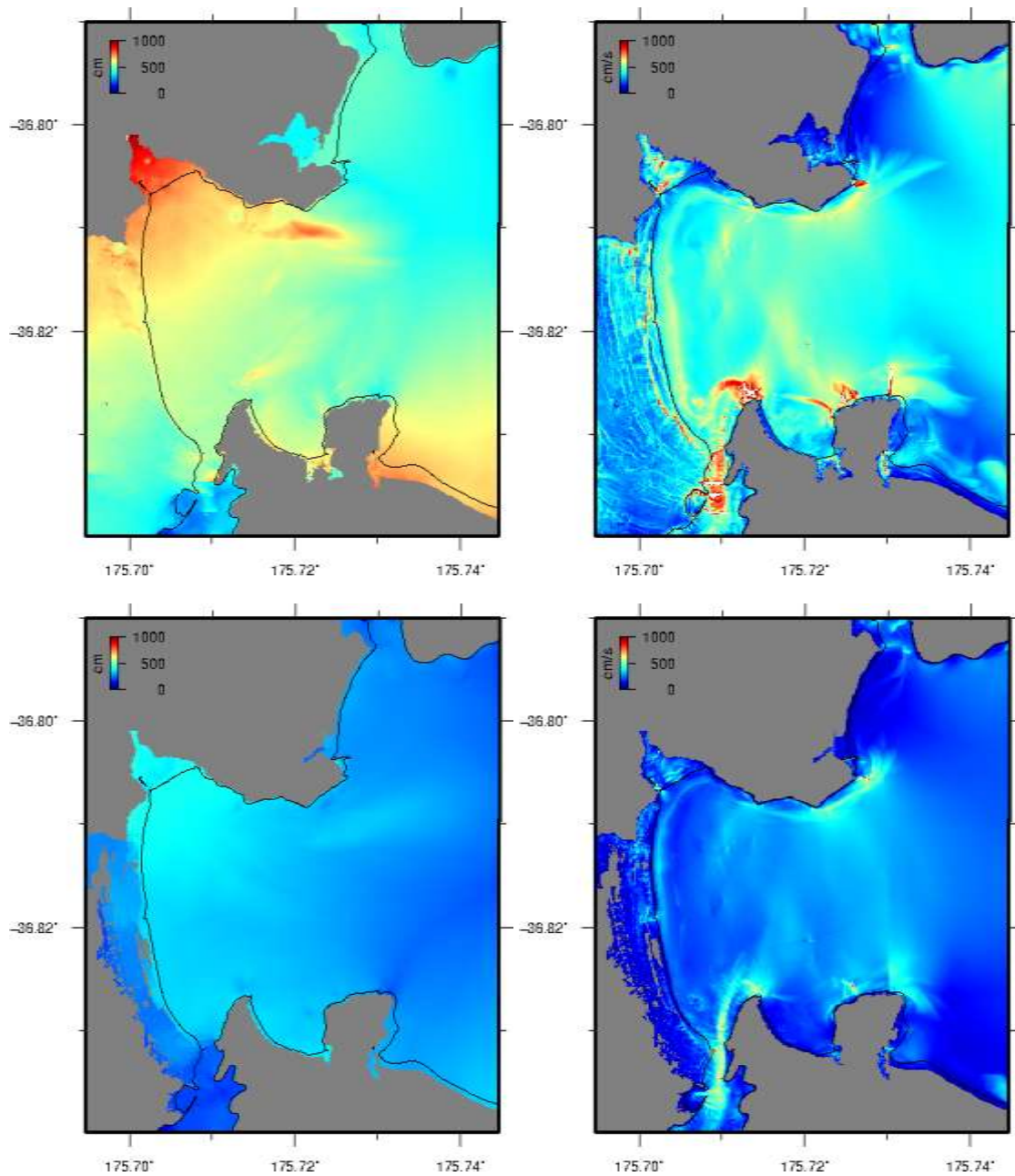


Figure 5.8 Kermadec Trench scenarios in Whitianga. Case 5 (top) and Case 6 (bottom). For each case water level is on the left and current speed is on the right.

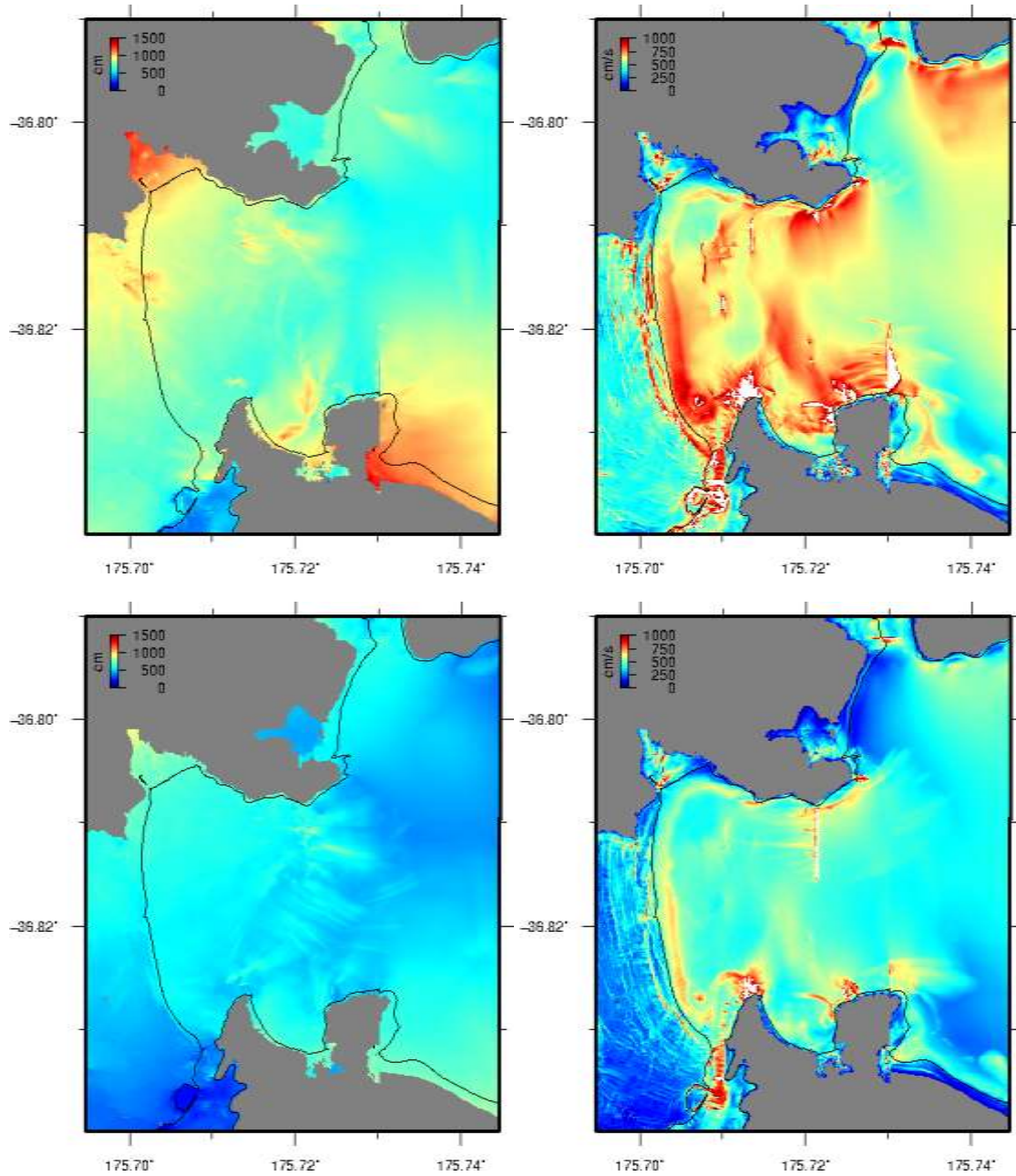


Figure 5.9 Kermadec Trench scenarios in Whitianga. Case 7 (top) and Case 8 (bottom). For each case water level is on the left and current speed is on the right.

6 SITE VISIT

A field trip was made to the study sites of Tairua, Whitianga and Pauanui in May 2012. The purpose of this trip was to see the site conditions first hand and to provide a first order reality check on the bathymetry and topography grids used in the study. The following photos depict important sites as they relate to tsunami inundation.

6.1 Tairua



Figure 6.1 The Tairua wharf.



Figure 6.2 Looking inland from near cnr. Manaia and Hapenui Roads.



Figure 6.3 (top) looking out of the harbour entrance from Manaia Rd. (bottom) view from the top of Paku Hill.



Figure 6.4 (top) View of harbour from Paku Hill. (bottom) Tairua Beach from Paku Hill.

6.2 Pauanui



Figure 6.5 Views of Pauanui from Paku Hill.



Figure 6.6 (top) Pauanui from Paku Hill (bottom) Pauanui Beach, view to south showing the width of the setback and the relatively high beach berm.

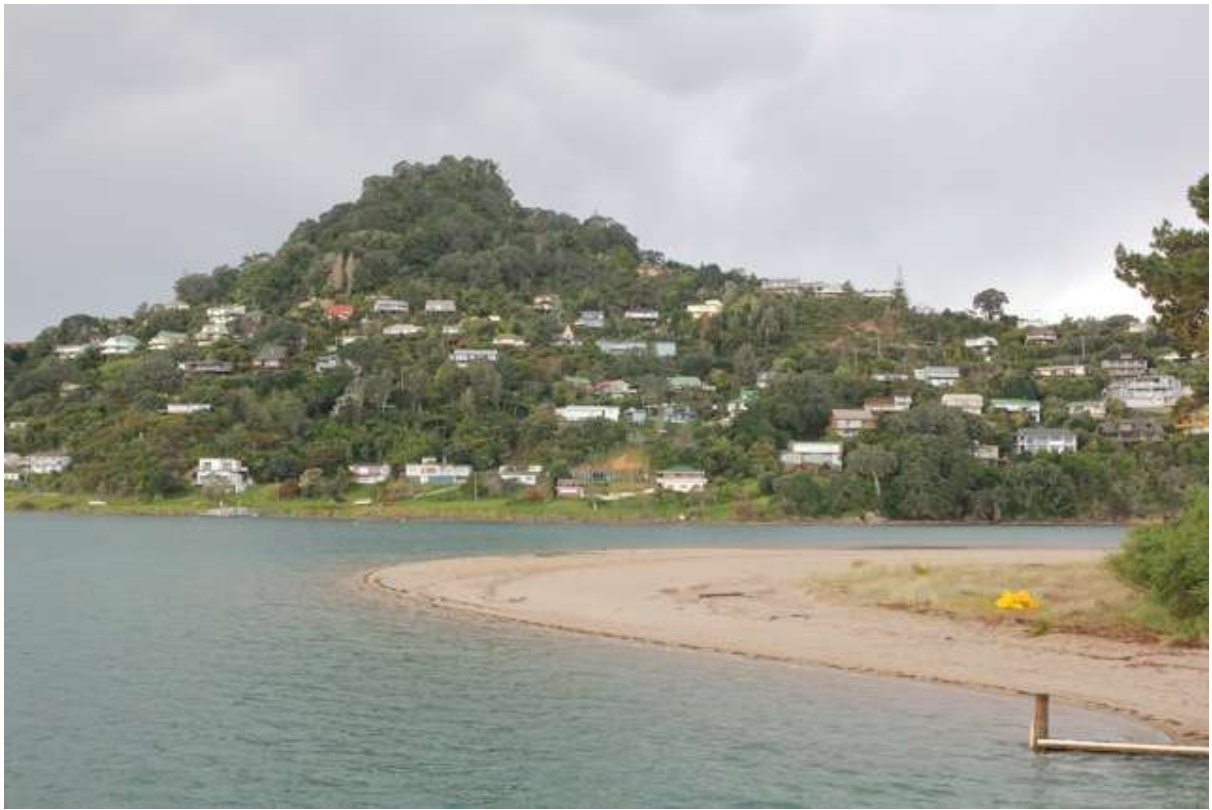


Figure 6.7 (top) View from Pauanui across the harbour entrance to Paku Hill. (bottom) inside the Pauanui canals.



Figure 6.8 Views of the Pauanui canals.

6.3 Whitianga



Figure 6.9 Views of the Whitianga water front near the marina entrance.



Figure 6.10 (top) Boats parked near the entrance to the Whitianga Marina. (bottom) Land for sale near the beachfront at Buffalo Beach.



Figure 6.11 Panoramic view of the Buffalo Beach beachfront.



Figure 7.2 Inundation at Tairua/Pauanui from Case 7 source scenario.



Figure 7.3 Inundation at Tairua/Pauanui from Case 8 source scenario.



Figure 7.5 Maximum current speed at Tairua/Pauanui from Case 7 source scenario.



Figure 7.6 Maximum current speed at Tairua/Pauanui from Case 8 source scenario.

8 REFERENCES

- Bell, R., Goff, J., Downes, G., Berryman, K., Walters, R., Chague-Goff, C., Barnes, P., and Wright, I., Tsunami Hazard for the Bay of Plenty and Eastern Coromandel Peninsula : Stage 2, NIWA Client Report: HAM2004-084 June 2004.
- Borrero, J., Bell, R., Csato, C., DeLange, W., Greer, D., Goring, D., Pickett, V. and Power, W. (2012) Observations, Effects and Real Time Assessment of the March 11, 2011 Tohoku-oki Tsunami in New Zealand, *Pure and Applied Geophysics*, DOI 10.1007/s00024-012-0492-6.
- Heath, R.A. (1976). The response of several New Zealand harbours to the 1960 Chilean Tsunami. *In*: Heath, R.A.; Cresswell, M.M. (Eds.): Tsunami Research Symposium 1974. *Bulletin of Royal Society of New Zealand* 15: 71–82.
- Egbert, G.D., Bennett, A.F., and M.G.G. Foreman, (1994). TOPEX/POSEIDON tides estimated using a global inverse model, *J. Geophys. Res.*, 99, 24821-24852.
- Fujii, Y. and Satake, K. (2012) Slip distribution and seismic moment of the 2010 and 1960 Chilean earthquakes inferred from tsunami waveforms and coastal geodetic data, *Pure and Applied Geophysics*, *in press*.
- New Zealand Nautical Almanac, 2010 – 2011, Land Information New Zealand (LINZ) <http://www.linz.govt.nz>.
- Prasetya, G., Healy, T. and de Lange, W. (2008) Hydrodynamic Modelling of Tsunami Overwash of Whitianga Township and Harbour, Technical report prepared for Waikato Regional Council
- Prasetya, G. and Wang, X. (2010) Tsunami frequency analysis for Eastern Coromandel and Waikato Region from Kermadec Trench and local sources within the Bay of Plenty, GNS Science Consultancy Report 2011/135 June 2011.
- Power, W. and Gale, N. (2010) Tsunami Forecasting and Monitoring in New Zealand, *Pure and Applied Geophysics*, 168:1125-1136.
- Titov, V.V. and Synolakis, C.E. (1995), Modelling of breaking and non-breaking long-wave evolution and run-up using VTCS-2, *J. Waterw. Port Ocean Coast. Eng.* 121(6), 308–316.
- Titov, V.V. and Synolakis, C.E.. (1998), Numerical modeling of tidal wave run-up, *J. Waterw. Port Ocean Coast. Eng.* 124(4), 157–171.
- Titov, V., Moore, C, Greenslade, D., Pattiaratchi, C., Badal, R., Synolakis, C., and KANOGLU, U. (2011). A new tool for inundation modeling: community modeling interface for tsunamis (ComMIT). *Pure Appl. Geophys.*, 168, 2121–2131.